National Library
of Canada

Bibliothèque nationale
du Canada

Canadian Theses Service

Service des thèses canadiennes

Ottawa, Canada
K1A 0N4

NOTICE

The quality of this microform is heavily dependent upon the quality of the original thesis submitted for microfilming. Every effort has been made to ensure the highest quality of reproduction possible.

If pages are missing, contact the university which granted the degree.

Some pages may have indistinct print especially if the original pages were typed with a poor typewriter ribbon or if the university sent us an inferior photocopy.

Reproduction in full or in part of this microform is governed by the Canadian Copyright Act, R.S.C. 1970, c. C-30, and subsequent amendments.

AVIS

La qualité de cette microforme dépend grandement de la qualité de la thèse soumise au microfilmage. Nous avons tout fait pour assurer une qualité supérieure de reproduction.

S'il manque des pages, veuillez communiquer avec l'université qui a conféré le grade.

La qualité d'impression de certaines pages peut laisser à désirer, surtout si les pages originales ont été dactylographiées à l'aide d'un ruban usé ou si l'université nous a fait parvenir une photocopie de qualité inférieure.

La reproduction, même partielle, de cette microforme est soumise à la Loi canadienne sur le droit d'auteur, SRC 1970, c. C-30, et ses amendements subséquents.

NL-339 (r. 88/04) c

Canadä

National Library of Canada
Canadian Theses Service

Ottawa, Canada
K1A 0N4

Bibliothèque nationale du Canada
Service des thèses canadiennes

The author has granted an irrevocable non-exclusive licence allowing the National Library of Canada to reproduce, loan, distribute or sell copies of his/her thesis by any means and in any form or format, making this thesis available to interested persons.

The author retains ownership of the copyright in his/her thesis. Neither the thesis nor substantial extracts from it may be printed or otherwise reproduced without his/her permission.

L'auteur a accordé une licence irrévocable et non exclusive permettant à la Bibliothèque nationale du Canada de reproduire, prêter, distribuer ou vendre des copies de sa thèse de quelque manière et sous quelque forme que ce soit pour mettre des exemplaires de cette thèse à la disposition des personnes intéressées.

L'auteur conserve la propriété du droit d'auteur qui protège sa thèse. Ni la thèse ni des extraits substantiels de celle-ci ne doivent être imprimés ou autrement reproduits sans son autorisation.

ISBN 0-315-55545-9

Canada

THE UNIVERSITY OF ALBERTA

A LARGE ACCEPTANCE DETECTOR FOR PHOTONUCLEAR REACTIONS

BY

© PHILIP PATRICK LANGILL

A THESIS

SUBMITTED TO THE FACULTY OF GRADUATE STUDIES AND RESEARCH
IN PARTIAL FULFILMENT OF THE REQUIREMENTS FOR THE DEGREE
OF MASTER OF SCIENCE

IN

NUCLEAR PHYSICS

DEPARTMENT OF PHYSICS

EDMONTON, ALBERTA
FALL 1989

THE UNIVERSITY OF ALBERTA

RELEASE FORM

NAME OF AUTHOR:	PHILIP PATRICK LANGILL
TITLE OF THESIS:	A LARGE ACCEPTANCE DETECTOR FOR PHOTONUCLEAR REACTIONS
DEGREE:	MASTER OF SCIENCE
YEAR THIS DEGREE GRANTED:	1989

Permission is hereby granted to THE UNIVERSITY OF ALBERTA LIBRARY to reproduce single copies of this thesis and to lend or sell such copies for private, scholarly or scientific research purposes only.

The author reserves other publication rights, and neither the thesis nor extensive abstracts from it may be printed or otherwise reproduced without the author's written permission.

Philip P. Langill

Permanent address:
825 - 20th Ave. N.W.,
Calgary, Alberta,
Canada, T2M 1E4.

Date: September 7, 1989

THE UNIVERSITY OF ALBERTA

FACULTY OF GRADUATE STUDIES AND RESEARCH

The undersigned certify that they have read, and recommend to the Faculty of Graduate Studies and Research for acceptance, a thesis entitled *A Large Acceptance Detector for Photonuclear Reactions* submitted by Philip Patrick Langill in partial fulfilment of the requirements for the degree of Master of Science in Nuclear Physics.

Nathan Rodning

Supervisor Dr. W.J. McDonald
Dr. N. Rodning

Dr. D. Budney

Dr. D. Skopik

Dr. F.C. Khanna

Date: Sept 7/1989

DEDICATION

For their unswerving love and support I dedicate this work to my family. I thank my parents Bernadette and Frederick Langill for their guidance and example. I thank Judith, David, Peter and Deborah for their friendship and I especially thank my late brother Martin who kindled my interest in science when I was very young. It is an honor to be part of such an outstanding group of people.

ABSTRACT

A large acceptance detector has been built at the University of Alberta for the study of photonuclear reactions at the Saskatoon Accelerator Laboratory (SAL). The Saskatoon Alberta Large Acceptance Detector (SALAD) utilizes a high pressure cylindrical gas target cell surrounded by four cylindrical wire chambers operated in Self Quenching Streamer (SQS) mode and a 24 element E - dE calorimeter. The energy resolution and attenuation lengths of the E and dE scintillators were measured at TRIUMF on the M13 pion channel. A preliminary test of SALAD was performed by studying p(p,p)p elastic scattering at TRIUMF on beam line 1B. The ability of SALAD to measure the angular distribution of p-p coincidence events and the ability of the Monte Carlo software to calculate the efficiency of SALAD for detecting p-p coincidence events was assessed by measuring the relative p-p elastic scattering cross section at $E_p = 220$ MeV.

ACKNOWLEDGEMENT

I would like to acknowledge those people involved in the development of the Saskatoon Alberta Large Acceptance Detector. For the design and construction of the wire chambers I thank Earl Cairns. For the design and construction of the gas target cell, calorimeter and support stand I thank Jan Soukup. For the design and construction of the electronic hardware employed by SALAD I thank Lars Holm and his staff of electronic experts - Jan Schaapman, Pat Wong and Randy Dorash. For writing the data acquisition software I thank Dr. Harry Fielding.

I appreciate the work of Dr. Peter Green, John Hewlett and Jim M^{ac}Kinnon for maintaining an excellent computing facility. I appreciate the help of the secretaries Greta Tratt and Llanca Letelier who, regardless how busy, were always able to lend a hand or answer a question. I also appreciate the support and words of encouragement from my colleagues Paul M^{c}Neely, Khaled Negm and Evan Hackett. Thank you all!

My sincerest appreciation goes to my supervisors. I thank Dr. W. J. M^{c}Donald for his financial support and guidance. I also thank Dr. Nathan Rodning for his guidance and advice, and for writing the Monte Carlo software as well as the SALAD and Monte Carlo data analysis software.

TABLE OF CONTENTS

A Large Acceptance Detector for Photonuclear Reactions

1. Introduction 1

2. The Saskatoon - Alberta Large Acceptance Detector 5
   - 2-A Introduction 5
   - 2-B Detector Geometry and Coordinate Definitions 6
   - 2-C Gas Target Cell 7
   - 2-D Wire Chambers 10
   - 2-E Calorimeter 17

3. SALAD Scintillator Pion Tests 22
   - 3-A Introduction 22
   - 3-B Procedure 22
   - 3-C Results 27
     - I Beam Profile 27
     - II Time of Flight Spectra 28
     - III Beam Scintillator Spectra 30
     - IV Light Attenuation and Collection 32
     - V SALAD E Scintillator Energy Resolution 41
     - VI SALAD dE Scintillator Energy Resolution 45

4. SALAD Efficiency Test 49
   - 4-A Introduction 49
   - 4-B Procedure 50
   - 4-C Wire Chamber Calibration 52
   - 4-D Track Reconstruction 53
   - 4-E The Reduced Data Set 57
   - 4-F The Final Data Set 69
   - 4-G Scintillator Energy Calibration 80
   - 4-H Efficiency Calculation From Monte Carlo Studies 85
   - 4-I The p(p,p)p Elastic Scattering Differential Cross Section . . 94

5. Conclusion 98

References 102

Appendix A: Characteristics of Wire Chamber Detectors 104

I Effects of Applied Voltage 104

II Effects of Gas Mixture 107

Appendix B: Mathematical Supplement 112

I Z Position Determination From Charge Division Readout 112

II Flight Time Through the M13 π Channel and π Decay Kinematics . . 114

III Linear Regression Formulas 117

IV Order of Peaks in 20.2 MeV Beam Scintillator Spectrum 117

V Energy Loss Distribution in the Beam Scintillator Spectra 119

VI Position Independent ADC Values 121

VII $1/\sqrt{E}$ Dependence of the Scintillator Energy Resolution 122

Appendix C: Monte Carlo Results 124

LIST OF TABLES

Figure	Description	Page
2-1.	Density, Radial Thickness and Areal Thickness of the Materials in each SALAD Component. (All errors in %)	10
2-2.	Physical Constants of the SALAD Scintillators.	19
3-1.	Pion Data for SALAD Scintillator Tests.	24
3-2.	Kinetic Energy Lost by the Pions in the Beam, dE and E Scintillators (Remaining Kinetic Energy in Parenthesis).	24
3-3.	ADC Centroids as a Function of Beam Position.	37
3-4.	Natural Logarithms of ADC Centroids for Each Scintillator End. . .	38
3-5.	Total Light Collected as a Function of Beam Position for the SALAD E Scintillator.	40
3-6.	SALAD E Scintillator Energy Resolution.	42
3-7.	Expected Total dE Scintillator Data.	47
3-8.	SALAD dE Scintillator Energy Resolution.	48
4-1.	p(p,p)p Elastic Scattering Cross Section Data Used by SAID. . . .	95

LIST OF FIGURES

Figure	Description	Page
2-1.	The SALAD Detector (Viewed from Upstream).	7
2-2.	The SALAD Detector (Side View - Section AA).	8
2-3.	Carbon Fiber Wrapping Directions Used in the SALAD Gas Target Cell Construction.	9
2-4.	Support Structure and Dimensions of the SALAD Wire Chambers.	12
2-5.	Configuration of a Single Wire Chamber Cell (not to scale).	13
2-6.	Scintillator and Wire Numbering Convention (Viewed from Upstream).	14
2-7.	Wire Chamber Electronics.	16
2-8.	Cross Sectional Dimensions of the SALAD E and dE Scintillators.	18
2-9.	SALAD Scintillator Circuitry and Trigger Logic.	20
3-1.	Beam Line M13 (Modified from C. Oram et al. NIM **75** (1981) 95).	23
3-2.	Orientation of the Wire Chamber and Scintillators Relative to the Pion Beam.	23
3-3.	Front End Electronics for the SALAD Scintillator Pion Tests.	25

3-4. A Typical Beam Profile. 27

3-5. TRF Spectra for the Various Pion Beam Energies. 29

3-6. Beam Scintillator Spectra for the Four Pion Beam Energies. . . . 31

3-7. 62.3 MeV Pion Beam Positions Relative to the SALAD Scintillators for Light Attenuation Measurements. 33

3-8. Energy Measured by the Left vs. Right Ends of the SALAD E Scintillator Beam Energy = 62.3 MeV). 35

3-9. Energy Measured by E Scintillator vs. the Right End of the SALAD dE Scintillator (Beam Energy = 62.3 MeV). 36

3-10. Log of ADC Centroid as a Function of Beam Position for the SALAD Scintillators. 39

3-11. Total Light Collected in the SALAD E Scintillator as a Function of Position. 41

3-12. E Scintillator Energy Spectra. 43

3-13. E_{Left} vs. Total Energy Measured in the SALAD E Scintillator. . . . 44

3-14. dE Right Scintillator Energy Spectra. 46

4-1. SALAD Efficiency Test on Beam Line 1B. $E_p = 220$ MeV. Collimators and Event Trigger Scintillators Shown. 51

4-2. Typical QSUM Spectra of a Single Wire for the Three Source Positions. 54

4-3. Calculated Source Positions for the Wire of Figure 4-2. 55

4-4. Reconstructed Tracks for a Typical p-p Scattering Event. 58

4-5. Minimum Distance and Interaction Vertex Definitions. 60

4-6. Interaction Vertex in the x-y Plane for (a) the H_2 Gas Target Cell and (b) a CH_2 Target of Uniform Areal Thickness. 62

4-7. Opening Angle of the Reduced p-p Data Set. 63

4-8. Coplanarity of the Reduced p-p Data Set. 64

4-9. Minimum Distance Between Outgoing Protons for the Reduced p-p Data Set. 65

4-10. Radial Vertex Position for the Reduced p-p Data Set. 66

4-11. RMS Error of Reconstructed Tracks for the Reduced p-p Data Set. 67

4-12. Anglular Distribution of Scattered Protons for the Reduced p-p Data Set. 68

4-13. Fraction of p-p Events in the N(θ) Spectrum as a Function of Opening Angle Cut. 70

4-14. Fraction of p-p Events in the N(θ) Spectrum as a Function of Coplanarity Cut. 71

4-15. Fraction of p-p Events in the N(θ) Spectrum as a Function of Minimum Distance Cut. 72

4-16. Opening Angle of the Final p-p Data Set. 73

4-17. Coplanarity of the Final p-p Data Set. 74

4-18. Minimum Distance Between Outgoing Protons
for the Final p-p Data Set. 75

4-19. Radial Vertex Position for the Final p-p Data Set. 76

4-20. Anglular Distribution of Scattered Protons
for the Final p-p Data Set. 77

4-21. Opening Angle and Vertex Position of p-p Events
Failing the Coplanarity Test. 79

4-22. Missing Energy Spectra of the SALAD E and dE Scintillators. . . 82

4-23. Energy Loss of Scattered Protons in SALAD
as a Function of θ_{Lab}. 84

4-24. Opening Angle of the Monte Carlo Data Set. 87

4-25. Comparison of the Radial Position of the p-p Interaction Vertex
for the Monte Carlo and p-p Data Sets (Target wall subtracted
from the p-p data). 88

4-26. θ_{Lab} Distribution Used to Generate the Monte Carlo Data Set. . . . 90

4-27. N(θ) Distribution of the Analyzed Monte Carlo Data Set. 91

4-28. Efficiency of SALAD for Detecting p-p Coincidence Events. . . . 92

4-29. The (a) Single and (b) Total Efficiency of SALAD for Detecting p-p Events. 93

4-30. The p-p Elastic Scattering Cross Section. 96

A-1. Schematic Design of a Typical Gas Filled Wire Chamber Detector. (Modified from W. J. Price, Nuclear Radiation Detection, 1964) . 104

A-2. Log(n) as a Function of Applied Voltage for the Gas Filled Detector of Figure A-1. (Modified from D. H. Wilkinson, Ionization Chambers and Counters, 1950) 105

A-3. A Summary of the Wire Chamber Modes of Operation. (Modified from M. Matoba, Radiation Detectors and Their Uses, 1988) . . 111

B-1. A Particle Stopping in the SALAD E Scintillator at Some Arbitrary Position 122

C-1. Scattering Angle θ_{Lab} Versus Reconstructed Beam Energy for the (a) p-p and (b) Monte Carlo Data Sets. 124

C-2. Stopping Power Versus Energy Deposited in E Scintillator for the (a) p-p and (b) Monte Carlo Data Sets. 125

C-3. Difference Between the (a) Theta and (b) Phi Angles as Generated by the Monte Carlo and Calculated by the Track Reconstruction Software. 126

C-4. Difference Between the (a) Radial Vertex Position and (b) X-Coordinate of the Radial Vertex Position as Generated by the Monte Carlo and Calculated by the Track Reconstruction Code. 127

C-5. $|\phi_1 - \phi_2| - 180^{o}$ for the (a) p-p and (b) Monte Carlo Data Sets. . . 128

C-6. $|\theta_1 + \theta_2| - 87^{o}$ for the (a) p-p and (b) Monte Carlo Data Sets. . . 129

C-7. Minimum Distance Between Outgoing Tracks for the (a) p-p and (b) Monte Carlo Data Sets. 130

C-8. RMS Tracking Error for the (a) p-p and (b) Monte Carlo Data Sets. 131

C-9. Z - Position of the Interaction Vertex for the (a) p-p and (b) Monte Carlo Data Sets. 132

C-10. Total Charge Collected by Wire Chamber 1 (Sum Over All Wires) for the (a) p-p and (b) Monte Carlo Data Sets. 133

C-11. $E_{Calculated} - E_{Measured}$ for the dE scintillators (Sum Over All dE Scintillators) for the (a) p-p and (b) Monte Carlo Data Sets. 134

C-12. $E_{Calculated} - E_{Measured}$ for the E scintillators (Sum Over All E Scintillators) for the (a) p-p and (b) Monte Carlo Data Sets. 135

C-13. Beam Energy as Reconstructed from Energy Deposited in Scintillators for Two Track Events. (a) p-p and (b) Monte Carlo Data Sets. 136

CHAPTER 1

INTRODUCTION

The study of photon induced nuclear reactions dates back to the work of Chadwick and Goldhaber (1934)$^{(1)}$, Fermi (1935)$^{(2)}$ and Seigert (1937)$^{(3)}$. The subject is certainly not new and much has been learned in the past 50 years. Why is it still important to study photonuclear physics?

From a theoretical point of view, the study of the interaction of photons with light nuclei (atomic number ≤ 4) is relatively straight forward. Light nuclei make the best laboratory for studying the nucleon - nucleon interaction since the wave functions are well known. In photonuclear reactions the initial and final states are clearly separated, since the incoming channel can be treated as a first order perturbation. All the physics of interest appears through the final state interactions$^{(4)}$.

Many photonuclear observables have been calculated particularly for the deuteron which is the simplest N–N state. A comparison of the calculated predictions to the measured data should test probable theoretical models. Unfortunately in many cases, the quantity and/or quality of the data makes this approach impossible.

For example, the absolute deuteron photodisintegration cross section has been measured as a function of θ_{cm} many times at low energy ($E_\gamma \leq 130$ MeV) by studying both the reaction $d(\gamma,p)n$ and its inverse $p(n,d)\gamma$ (radiative capture). A comparison of the data from 10 different experiments is given by Meyer$^{(5)}$ for $E_\gamma = 95$ MeV. The large discrepancies between the data are most likely due to differences in overall normalization. Meyer also shows a comparison of several theoretical calculations of the same cross section as a function of θ_{cm} for $E_\gamma = 100$ MeV. Included in the comparison are impulse approximation calculations with different nucleon - nucleon potentials (i.e. varying D state probabilities), calculations which contain explicit contributions from meson exchange currents, a calculation imposing gauge invariance and a calculation involving relativistic contributions to the charge density. The range in values of the absolute cross section as predicted by these calculations is as large as the range in measured absolute cross sections. It is clear that the data must be improved in order to isolate the important final state mechanisms.

Another aspect of photonuclear physics of fundamental importance is the formation of the $\Delta(1236)$ resonance at intermediate energies ($130 < E_\gamma < 350$ MeV). The Δ resonance plays an important role in the description of the intermediate - range part of the nucleon -nucleon interaction.

Theoretically the Δ is created in the nucleus in a very clean way. Unfortunately, the Δ is both unstable and strongly interactive. Generally the Δ decays via $\Delta \rightarrow \pi N$ before escaping the nucleus. The propagation of the Δ in the nucleus is not well understood, and the incorporation of the Δ into the formalism of final state interactions is difficult. Although studies of pion photoproduction ($\gamma N \rightarrow \pi N$) provide constraints, it is not yet clear how to define the interaction of an unstable isobar and stable nucleon$^{(4)}$. Photonuclear reactions provide a means for studying the propagation of the Δ in nuclei as well as for studying the N-Δ and Δ–nucleus interactions.

At intermediate energies the Δ resonance dominates the total $d(\gamma,p)n$ cross section as well as the total cross sections for π - N scattering and pion photoproduction. Cameron$^{(6)}$ gives a comparison of the $d(\gamma,p)n$ total cross section data around $E_\gamma = 300$ MeV. The scatter in the data resembles that of the $d(\gamma,p)n$ absolute cross section data at $E_\gamma = 95$ MeV given by Meyer. Again it is clear that the data must be improved to aid in the understanding of the N-Δ interaction.

It has been found in many cases that the most important part of the interaction of the Δ with the nuclear medium can be approximated by a multiple scattering series of its constituents (π or nucleon) with the other nucleons. At higher energies ($E_\gamma > 350$ MeV) this approximation fails significantly for some reactions (ie. $\gamma d \rightarrow \pi NN$) This indicates that the remaining part of the N-Δ interaction which cannot be reduced to a multiple scattering series must be studied. It is not clear whether this deviation is due to the intermediate part of the nucleon - nucleon interaction or to a short range part involving the quark degrees of freedom in the nucleon$^{(4)}$.

This has been a very brief discussion of a few of the problems which provide motivation for studying photonuclear reactions. An excellent review of the state of affairs regarding radiative processes in few nucleon systems is given in Ref. 7.

It has been emphasized above that in many cases the quality of the photonuclear data must be improved. The photons used to study photonuclear reactions are produced by electron bremsstrahlung. A major difficulty in using a bremsstrahlung beam to study reactions is the fact that the bremsstrahlung beam contains a continuous distribution of photon energies. In order to measure an absolute cross section at a particular photon energy one must (a) determine the total flux of photons in each energy bin and (b) determine the energy bin corresponding to each event observed. These difficulties have led to the development of tagged photon beams where the electron which releases a bremsstrahlung photon is momentum analyzed and the energy of the photon is deduced.

The recently upgraded Saskatoon Accelerator Laboratory (SAL) employs a continuous wave (CW) electron beam which ranges in energy between 100 – 325 MeV. A tagged photon beam of flux $\sim 10^7\ \gamma$ / s and energy range of 90 – 320 MeV(8) is generated using the CW beam. The energy resolution of the photon beam is 3% of the electron energy at the center of the focal plane (a mini-tagger is available that provides a factor of 10 improvement in energy resolution over a portion of the focal plane). The duty cycle (the fraction of the time the beam is on to the total time) of the tagged photon beam is ~ 100%.

A large acceptance detector dedicated to the study of photonuclear physics at SAL has been built at the University of Alberta. The Saskatoon Alberta Large Acceptance Detector (SALAD) is described in detail in chapter 2. The geometry of the detector is outlined and a discussion of the target, wire chambers and calorimeter employed by SALAD is given. Before the construction of SALAD was completed in September 1988 the energy resolution, light attenuation and light collection properties of an E - dE scintillator pair was measured. The results are given in chapter 3.

The actual measurement of a photonuclear cross section using SALAD will rely on two intermediate results. First the angular distribution of the reaction products must be measured by SALAD, and second, a Monte Carlo calculation of the efficiency of SALAD for detecting the reaction in question must be made. The ability of SALAD and the Monte Carlo code to perform these tasks is the topic of chapter 4. A simple p(p,p)p elastic scattering coincidence measurement served to test SALAD. The results of this test will be discussed in detail.

Finally in chapter 5 an assessment as to the performance of SALAD particularly in the proton elastic scattering test of chapter 4 is given. The status of the Monte Carlo code is also assessed and a brief comment as to the future of SALAD is given.

Appendix A is a brief summary of the characteristics and classification of wire chamber detectors. A discussion of the Self - Quenching - Streamer mode of wire chamber operation (the mode employed by SALAD) is also given. Appendix B is a mathematical supplement where statements made throughout the body of the text are backed up by a simple calculation. Important mathematical techniques used in some of the data analysis are also described. Appendix C is a collection of Monte Carlo generated results for the p-p coincidence test. When these results can be compared to the actual p-p coincidence data, the data results are also given.

The scope of this thesis has been broadened to serve as a SALAD users guide. The author has contributed to the assembly and calibration of SALAD, and has had responsibility for the analysis of the pion test and efficiency test data.

CHAPTER 2

THE SASKATOON-ALBERTA LARGE ACCEPTANCE DETECTOR

A) Introduction

When planning an experiment to study a nuclear interaction it is necessary to know the rate $R(\theta)$ at which the reaction products will be detected. For a perfectly efficient detector which subtends a solid angle $d\Omega(\theta)$ this detection rate is given by

$$R(\theta) = F_B(t)\, N_T\, \frac{d\sigma}{d\Omega}(\theta)\ d\Omega(\theta) \quad , \tag{2.1}$$

where $F_B(t)$ is the flux of incident beam particles, $d\sigma/d\Omega$ is the differential reaction cross section and N_T is the number of target particles per unit area. N_T can be calculated using

$$N_T = \tau \frac{N_A}{M} \quad , \tag{2.2}$$

where τ is the areal thickness of the target (in units of g / cm^2), N_A is Avogadro's Number and M is the molar weight of the target material. Photonuclear reaction rates are inherently small since reaction cross sections are small (~ 70 μb for d(γ,p)n at E_γ = 100 MeV)$^{(9)}$. Reaction rates are smaller still when tagged photon beams are used since $F_B(t)$ is relatively low (~ 10^6 γ / sec$^{(6)}$ compared to 10^9 γ / sec for bremsstrahlung, ie. non-tagged, photon beams$^{(4)}$). To maximize the photonuclear counting rate both the number of target particles N_T and the detector acceptance $d\Omega$ must be maximized.

The areal thickness of a target made from a gaseous material is given by $\tau = \rho l$ where l is the length of container traversed by the photon beam and ρ is the density of the gas which is given by

$$\rho = \frac{MP}{RT} \quad , \tag{2.3}$$

where P and T are the pressure and temperature of the gas and R is the ideal gas constant (R = 8.31 N·m / °K·mole). Using the above expressions the equation for N_T can be written

$$N_T = \frac{l\,P\,N_A}{R\,T} \quad . \qquad (2.4)$$

To maximize N_T either the pressure of the gas can be increased or the temperature decreased.

Cryogenic targets provide high N_T. However, large energy losses in the target and container make it difficult for low energy reaction products to escape into the surrounding detector. Also, the equipment used to maintain low temperature tends to limit the acceptance of the surrounding detector. These considerations suggest the use of a high pressure gas target.

The Saskatoon-Alberta Large Acceptance Detector (SALAD) is designed to study photonuclear interactions. SALAD employs a high pressure, room temperature, cylindrical gas target cell. It gives a large target thickness and allows the surrounding detector to have a cylindrical geometry. Thus SALAD attempts to minimize running time by maximizing both the detection acceptance and the gas target thickness while allowing the detection of relatively low energy reaction products. A description of the detector's geometry, and a discussion of the gas target cell, wire chambers and calorimeter that make up the SALAD detector is given below.

B) Detector Geometry and Coordinate Definitions

The cylindrical geometry of the SALAD detector is illustrated in figures 2-1 and 2-2. The length and radius of several components are given in figure 2-2. The dimensions of each component are given in detail below. Figure 2-1 shows the detector as viewed from the upstream end (the right side of figure 2-2). The line AA defines the x-axis of the detector. The x = 0, y = 0 point is chosen to coincide with the axis of the detector. From the perspective of figure 2-1, x increases from right to left and y increases from bottom to top. The angle ϕ is defined as shown in figure 2–1. The axis of the cylindrical wire chambers is chosen to define the z-axis of the detector as illustrated in figure 2-2. The z = 0 point is chosen to coincide with the geometric center of the wire chambers. The angle θ is defined as shown in figure 2-2.

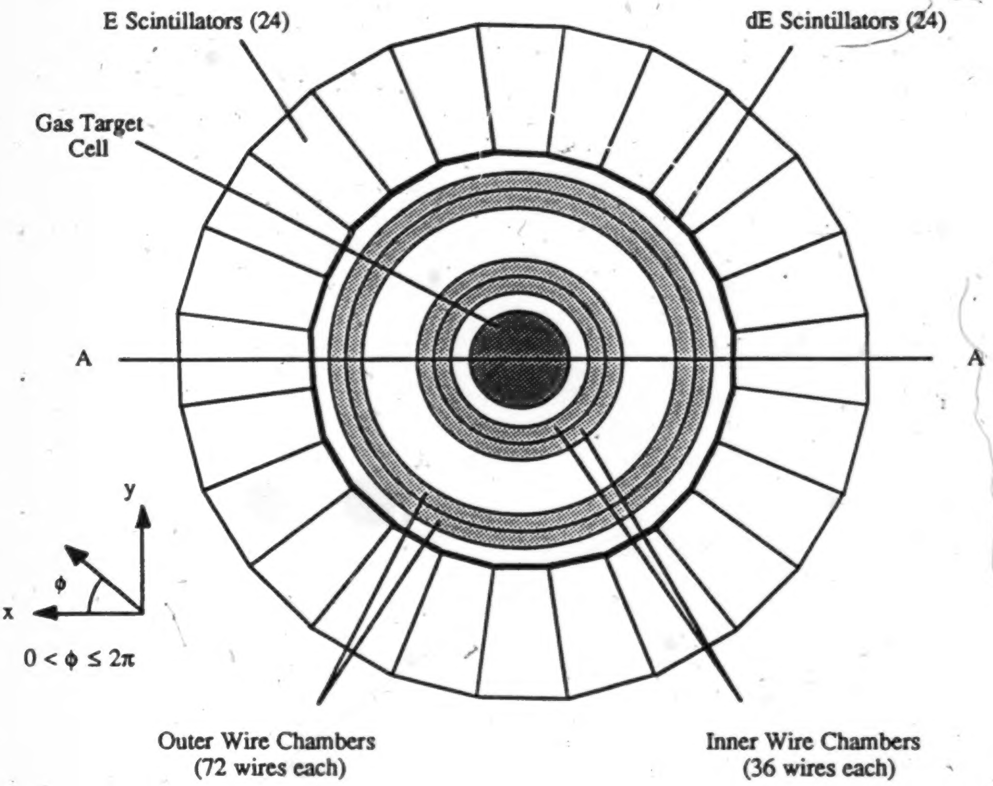

Figure 2-1

The SALAD Detector (Viewed from Upstream).

C) Gas Target Cell

Figure 2-2 shows the gas target cell inserted inside SALAD. It is mounted inside the detector on the wire chamber end supports and can be removed or inserted any time during the experiment. The z position of the gas target window is known to within ± 5 mm. The overall length of the target, from window to dome, is 236.6 cm. The inside radius is 5.048 cm and the volume of the target is 18.95 liters.

The target cell is lined with a thin layer of mylar. Over the mylar are wound two layers of a carbon fiber impregnated epoxy. It is known that the biaxial strength of a filament wound vessel depends on the angle at which the layers are wrapped relative

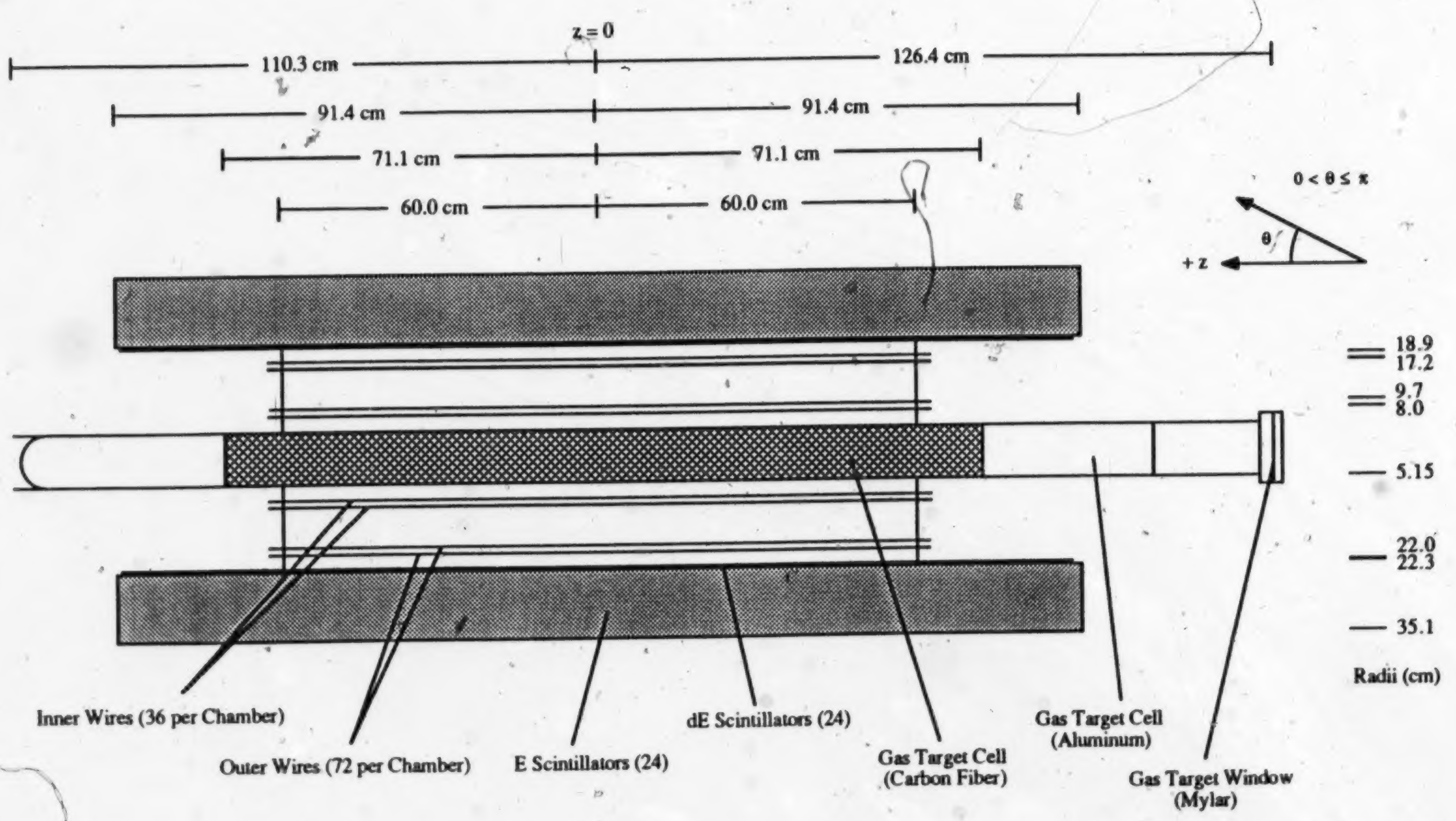

Figure 2-2 The SALAD Detector (Side View - Section AA).

to the axis of the vessel. Studies have shown that the maximum strength is attained with a wrapping angle of 54.75°(10,11). The SALAD target cell was wrapped as shown in figure 2-3.

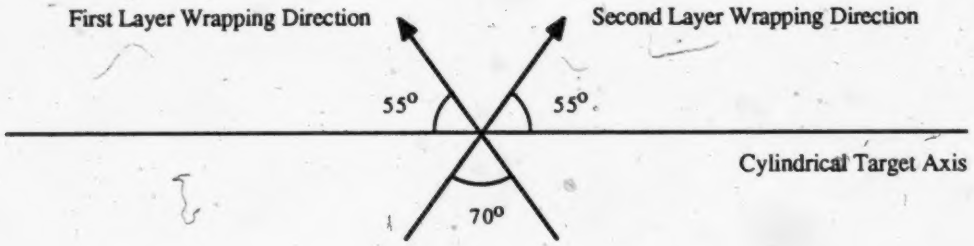
First Layer Wrapping Direction
Second Layer Wrapping Direction
55°
55°
Cylindrical Target Axis
70°

Figure 2-3

Carbon Fiber Wrapping Directions Used in the SALAD Gas Target Cell Construction.

The length of the mylar-carbon fiber tube portion of the target is 208.3 cm. Into each end of this tube are inserted 33.020 cm long x 0.079 cm thick aluminum tubes (the aluminum portions of the target cell are machined to a tolerance of 0.005 cm). There is a clearance of 0.020 cm in diameter in all cylindrical fits for adhesive. The downstream end of this assembly is then inserted 33.020 cm into a 38.259 cm long x 0.102 cm thick aluminum tube. The 5.239 cm length of aluminum tubing extending beyond the end of the carbon tube is threaded so that an aluminum dome can be attached to this end. The dome has an inside radius of curvature of 4.968 cm and a thickness of 0.074 cm. The upstream end of the assembly is inserted 33.020 cm into a 36.513 cm long x 0.102 cm thick aluminum tube. The 3.493 cm length of aluminum tubing extending beyond the end of the carbon tube is threaded so that an aluminum flange can be attached to this end. The flange is used to mount the target window. The material used as a window depends on the desired operating pressure(12). For the studies of chapter 4 (1 atm. operating pressure) a 'type A' mylar of thickness of 0.036 cm was used as a window.

The density, radial and areal thickness of the mylar lining, carbon fiber tubing and aluminum tubing are given in table 2-1. A *LOSSPROG*(13) calculation shows that a ~ 10 MeV proton has enough kinetic energy to pass perpendicularly through the mylar-carbon fiber tubing. LOSSPROG is a program used to calculate dE/dx for particles heavier than electrons based on the Bethe - Bloch equation with appropriate corrections at low energies. The results are reliable to within 5% for protons in the energy range 10 - 1000 MeV.

A 60 cm long section of this mylar lined 2-ply carbon fiber target has been tested without failing to a pressure of 30 atmospheres. It can therefore be operated safely at 15 atmospheres as safety regulations typically require an operating pressure of $\frac{1}{2}$ the failure pressure of a pressurized gas target.

Table 2-1 Density, Radial Thickness and
Areal Thickness of the Materials in each SALAD Component. (All errors in %)

SALAD Component: Material	ρ (g/cm^3)	ι (cm)	τ (mg/cm^2)
Gas Target Cell:			
Mylar Lining	1.40 ± 3	0.013 ± 2	18.2 ± 5
Carbon Fiber Tube (2 ply)	1.65 ± 5	0.051 ± 5	84.2 ± 10
Aluminum Tubes (Inner and Outer)	2.70 ± 1	0.181 ± 2	488.6 ± 3
Wire Chambers:			
Polyurethane Foam	0.05 ± 15	0.500 ± 5	25.0 ± 20
Graphite coated Kapton (1 layer)	1.85 ± 10	0.003 ± 2	5.6 ± 12
Wire Chamber Gas Mixture (1 atm.)	2.08×10^{-3} ± 2	1.200 ± 3	2.5 ± 5
Calorimeter:			
Vinyl Light Seal	1.20 ± 3	0.025 ± 2	30.0 ± 5
Aluminized Mylar (1 layer)	1.35 ± 3	0.003 ± 2	4.1 ± 5
dE Scintillator	1.03 ± 1	0.318 ± 1	237.5 ± 2
E Scintillator	1.03 ± 1	12.753 ± 1	13.1×10^3 ± 2

D) Wire Chambers

The path of a charged reaction product through the detector is tracked by the wire chambers. Figure 2-1 shows that SALAD employs four wire chambers, two near the target and two near the calorimeter. Each wire chamber is 120.0 cm long as shown in figure 2-2. The support structure and radial dimensions of the wire chambers is shown in detail in figure 2-4. The wire chambers are numbered 1 to 4 from smallest to largest radius as shown in figure 2-4. Wire chambers 1 and 2 utilize 36 sense wires each and wire chambers 3 and 4 utilize 72 sense wires each. The wires are made from 50 μm diameter stainless steel with a resistance / unit length of 5.3 Ω / cm. The wires are mounted under a tension of 0.98 Newtons.

The cylindrical walls of the wire chambers are made from a low density polyurethane foam. Each foam cylinder wall is lined on both sides with a thin sheet of kapton. The kapton is coated with a film of graphite to make it conducting. The inner and outer radii of each cylinder as well as the radii of the wire positions in each chamber are shown in figure 2-4.

Each wire chamber pair (i.e. wire chambers 1 and 2 or 3 and 4) is made using three concentric polyurethane foam cylinders as shown in figure 2-4. The inner cylinder of a wire chamber pair supports the inner set of wires and the middle cylinder supports the outer set of wires. The space between the inner cylinder and middle cylinder and between the middle cylinder and outer cylinder is air-tight, confining the wire chamber gas around the wires. The wire chamber gas used in SALAD is a mixture of 70% isobutane (C_4H_{10}) and 30% argon by volume. This gas mixture enables the wire chambers to be operated in Self-Quenching-Streamer mode (this mode of wire chamber operation is discussed in appendix A). The density, radial and areal thickness of the polyurethane foam, graphite coated kapton and wire chamber gas mixture are given in table 2-1.

Each wire is physically separated from its neighbors by a 1.2 cm wide x 0.003 cm thick kapton strip coated with a thin film of graphite to make it conducting. The shape of a single wire chamber cell is shown schematically in figure 2-5. The arc lengths A and B are different for each wire chamber because (a) the wire chambers have differing radii and (b) each cell does not span the same number of degrees in ϕ. Wire chambers 1 and 2 hold 36 cells each spanning 10° in ϕ while wire chambers 3 and 4 hold 72 cells each spanning 5° in ϕ. The resulting arc lengths A and B are 1.29 cm and 1.50 cm respectively for wire chamber 1, 1.59 cm and 1.80 cm for wire chamber 2, 1.45 cm and 1.55 cm for wire chamber 3 and 1.60 cm and 1.70 cm for wire chamber 4. The wires are situated at the geometric center of each cell. The relative positions of the wires in each wire chamber is shown in figure 2-6. Also shown in this figure is the convention chosen for numbering the wires. Wire #1 in chambers 1 and 2 lie at

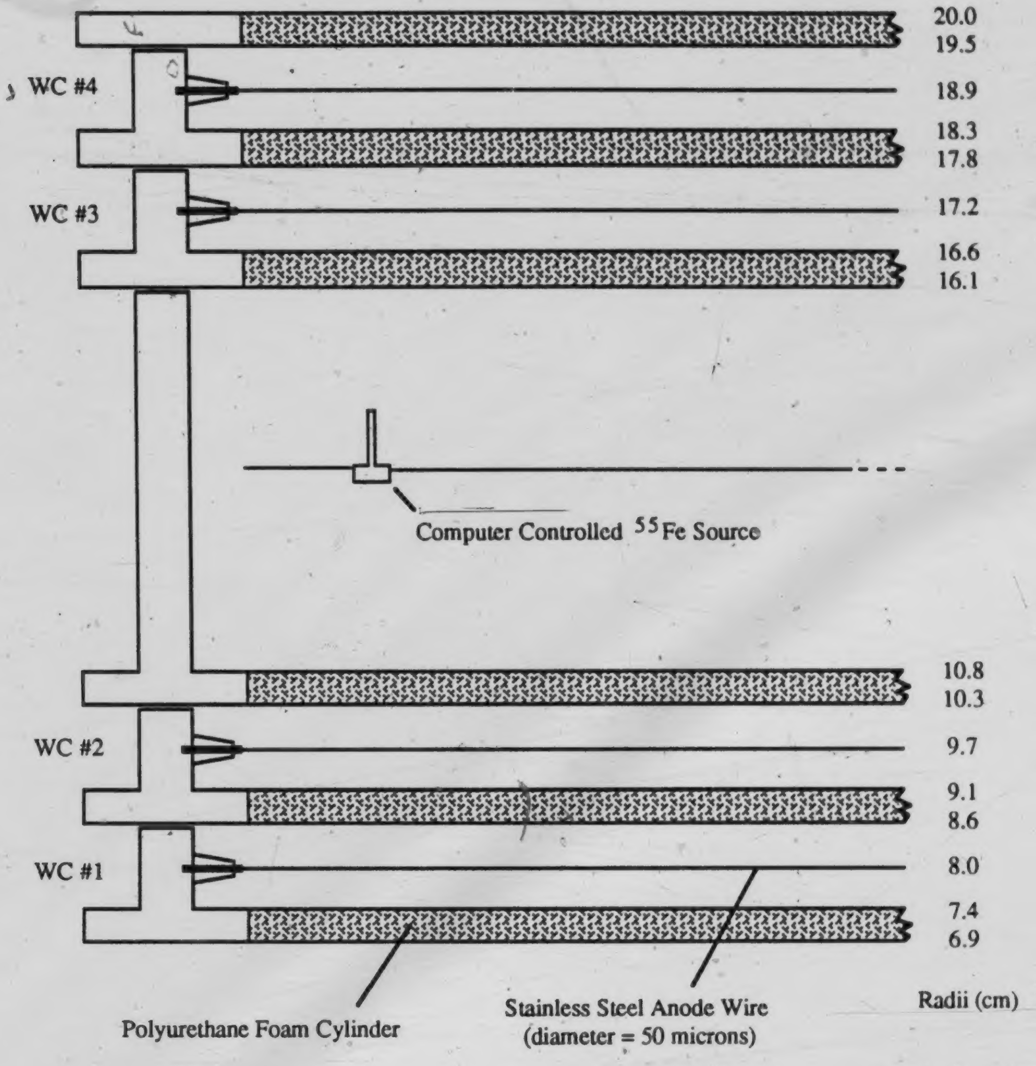

Figure 2-4

Support Structure and Dimensions of the SALAD Wire Chambers

$\phi = 10^\circ$ and 5° respectively. Wire #1 in chambers 3 and 4 lie at $\phi = 0^\circ$ and 2.5° respectively. The wires are equally spaced in ϕ and the wire numbers increase with increasing ϕ.

The wires are calibrated using two ^{55}Fe γ ray sources (E_γ = 5.9 keV) each

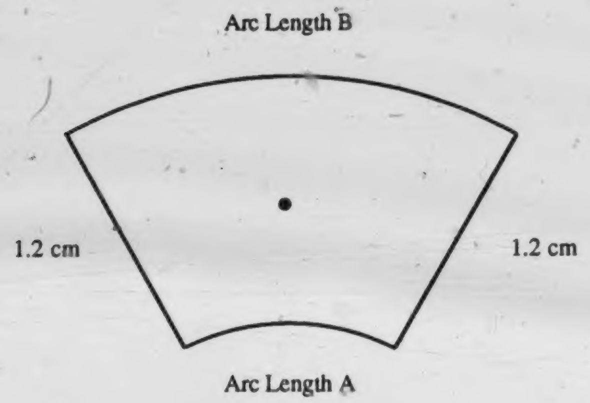

Figure 2-5

Configuration of a Single Wire Chamber Cell (not to scale).

collimated to 1mm. The sources are mounted between the two wire chamber pairs with one source illuminating the inner pair and the other illuminating the outer pair. Figure 2-4 shows the latter. The photon beams from the two sources are separated by 180° in ϕ. The source movement is controlled by computer and the wires are calibrated by positioning the sources at known z positions. For this work the three z positions; $z = 0 \pm 1$ mm and $z = \pm 443 \pm 1$ mm were used. When experimental data is being recorded the radioactive sources are parked in shielded areas. The behavior of the wire chambers over time can be monitored throughout an experiment by performing a source calibration at regular intervals.

During an experiment the E and dE scintillators provide the event trigger (this is discussed in detail in section E). During a source calibration the wire chamber electronics must provide both amplified signals for analog to digital conversion *and* the event trigger. To obtain a trigger, positive feedback operational amplifiers, or Schmitt triggers, are used. The electronic configuration at the ends of the anode wires is shown schematically in figure 2-7.

The graphite coated kapton lining the walls of each wire chamber cell is kept at a high negative potential (~ -3500V) relative to the anode wire at ground potential. Some of the wire chamber gas in a cell is ionized when an energetic charged reaction product

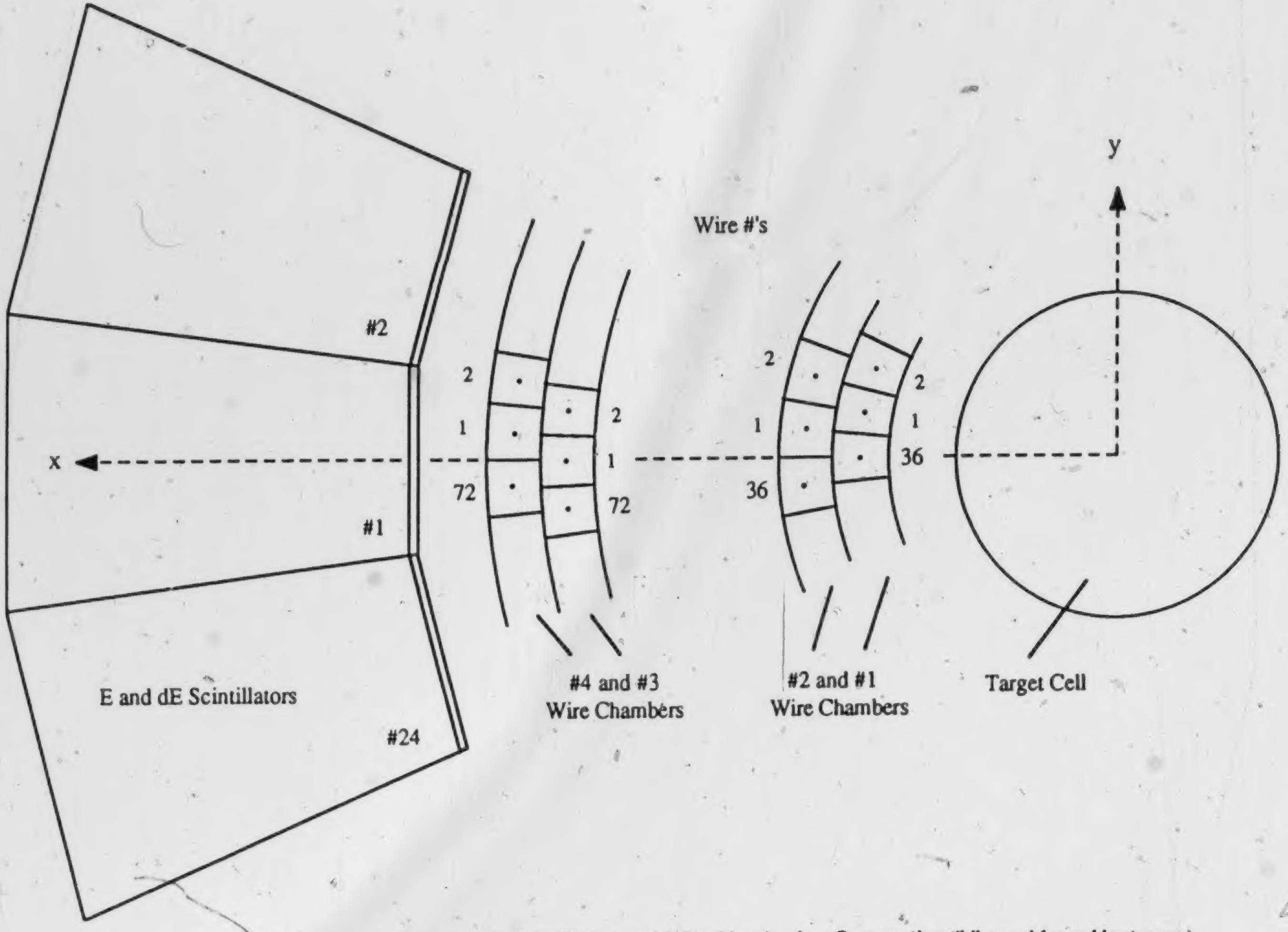

Figure 2-6 Scintillator and Wire Numbering Convention (Viewed from Upstream)

passes through. The free electrons cause more ionization as they accelerate towards the anode wire. A total amount of charge Q is deposited on the wire as a result of this avalanche of electrons. The charge Q splits into two parts, Q_{up} and Q_{dn}, which are collected at the upstream and downstream ends of the wire respectively. As shown in appendix B-I, the calculated position (z) along the wire where Q is deposited is related to Q_{up} and Q_{dn}.

The relative sizes of Q_{up} and Q_{dn} depend partly on the impedance Z of the electronics at the end of each wire. As shown in appendix B-I, the smaller the value of Z the smaller the error in the calculation of z. The impedance Z of the electronics that Q 'sees' is made small by use of an NPN transistor operated in common base mode (figure 2-7). The impedance on the emitter side of the transistor is low (~ 82 Ω) while the impedance on the collector side of the transistor is much higher (~ 10 kΩ).

A portion of the current pulse, upon reaching point A, charges the capacitor C1. If the amplitude of the current pulse at point A is large enough (which depends on the position on the wire where the charge Q is collected), the bias on the Schmitt trigger exceeds threshold and the Schmitt trigger is activated giving an event trigger. The amplitude of the current pulse at A may be too small to activate the Schmitt trigger if the original charge Q is collected over $\sim \frac{2}{3}$ of the wire length from the end. In this case the Schmitt trigger at the other end of the wire will be activated. The actual event trigger is an OR of the Schmitt trigger signals from both ends of the wire.

The wire chamber electronics is organized into 12 *sectors*. One sector includes 18 wires - 6 wires from chambers 3 and 4, and 3 wires from chambers 1 and 2. Since the wires are self triggered in source calibration mode, they are sensitive to background radiation. To prevent the background from swamping the source data, only the sector nearest the radioactive source is turned on when doing a source calibration.

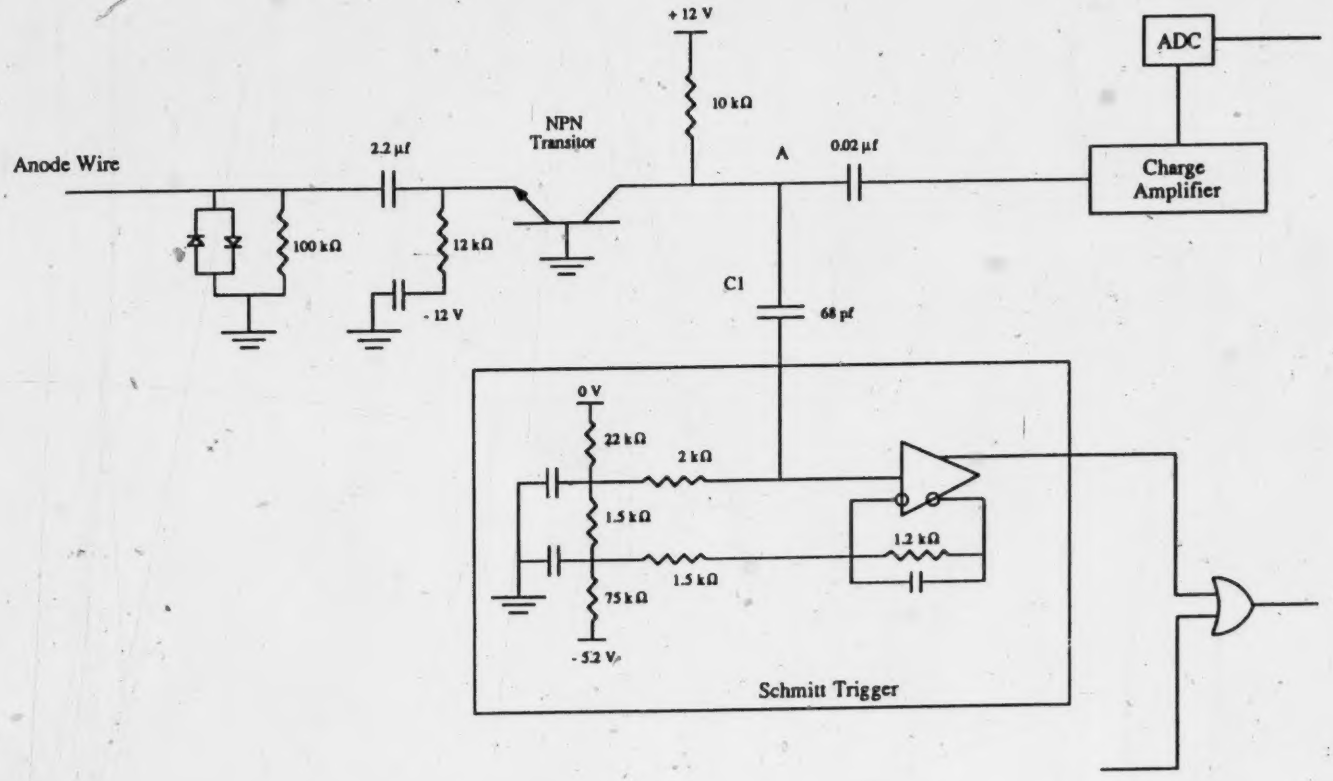

Figure 2-7 Wire Chamber Electronics

E) Calorimeter

The geometry and lengths of the SALAD E and dE scintillators are shown in figures 2-1 and 2-2. There are 24 dE-E pairs each subtending 15° in ϕ. The E and dE scintillators are numbered as shown in figure 2-6. The cross sectional dimensions of the E and dE scintillators are shown in figure 2-8. The E scintillators are 182.9 cm long and the dE scintillators are 180.3 cm long. The E and dE scintillators are centered lengthwise as shown in figure 2-2. Photomultiplier tubes are used to collect light from both ends of the E and dE scintillators.

The E and dE scintillators are individually wrapped in a thin sheet of aluminized mylar. This optically isolates the scintillators along their lengths. The wrapping is open at the ends making it possible for stray light to enter the scintillators. Therefore the calorimeter must be sealed as a unit from light leaks. The light seal consists of (a) a black vinyl tube which fits between wire chamber 4 and calorimeter and between the two photomultiplier support end plates, and (b) the outer steel cylinder. The density, radial and areal thickness of the vinyl light seal, aluminized mylar and E and dE scintillators are given in table 2-1.

The E scintillator light guides are made from 'UVT' (ultraviolet transparent) acrylic plastic. The end fixed to the E scintillator is wedge shaped and is proportionally smaller by 0.16 cm on each side. The light guide is tapered parabolically over a length of 20.25 cm to a circular surface 4.2 cm in diameter. To this surface is fixed a cylindrical light pipe of length 10.8 cm and diameter 4.1 cm. The light pipe is optically coupled to a Philips XP-2202 10 stage photomultiplier tube (PMT).

The dE light guides consist of 4 lengths of 0.32 cm thick x 1.45 cm wide clear plastic. At the scintillator end of the dE light guide, the 4 lengths are joined forming a 0.32 cm thick x 5.80 cm wide surface. At the other end the lengths are joined forming a 1.28 cm x 1.45 cm surface. To this surface is fixed a cylindrical light pipe of length 10.8 cm and diameter 4.1 cm. The light pipe is optically coupled to a Philips XP-2262 12 stage PMT. In addition to the change in cross sectional dimensions from one end to the other, the dE light guide bends around the E scintillator light guide. As a result, the dE and E PMTs' are at the same angle ϕ, but the dE PMT is further from the axis of the detector than the E PMT.

The SALAD scintillators are manufactured by the Bicron Corporation. The

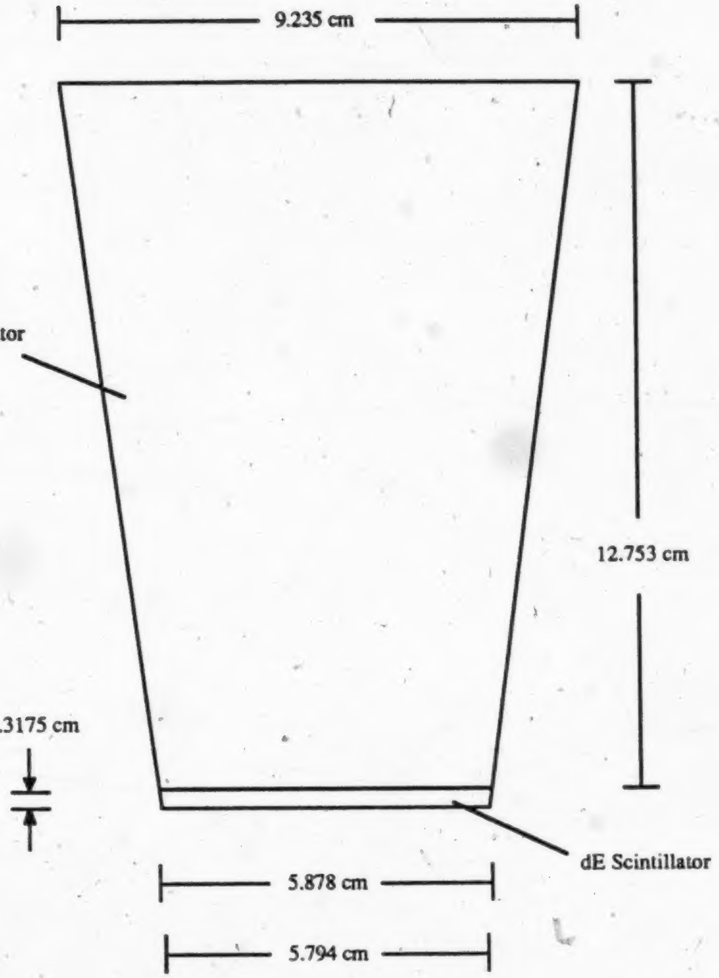

Figure 2-8

Cross Sectional Dimensions of the SALAD E and dE Scintillators.

types of plastic scintillators used in SALAD are BC-408 and BC-412. The base material of the scintillators is polyvinyltoluene. The scintillators have a density of 1.032 g / cm^3 and a refractive index of 1.58. Other physical constants pertaining to these two types of scintillator material are given in table 2-2$^{(14)}$.

The properties of the BC-408 and BC-412 scintillators are most similar to the

Table 2-2

Physical Constants of the SALAD Scintillators.

CONSTANTS	BC - 408	BC - 412
Light Output (% Anthracene)	64	60
Rise Time (ns)	0.9	1.0
Decay Time (ns)	2.1	3.3
Pulse Width FWHM (ns)	~2.5	4.2
Light Attenuation Length* (cm)	210	210
Wavelength of Max. Emission (nm)	425	434
Number of C Atoms per cm^3 ($x\ 10^{22}$)	4.74	4.74
Number of H Atoms per cm^3 ($x\ 10^{22}$)	5.23	5.23
Number of Electrons per cm^3 ($x\ 10^{23}$)	3.37	3.37
Ratio H:C Atoms	1.104	1.104

*1 cm x 20 cm x 200 cm cast sheet with edges polished - phototube at one end.

Nuclear Enterprises Pilot F and NE-110 plastic scintillators respectively. The calorimeter was assembled without regard to scintillator type. There is no correspondence between E or dE scintillator and scintillator type, and no correspondence between scintillator types in a given dE-E pair.

Figure 2-9 shows the scintillator trigger logic circuit. There are 96 channels of information available from which a trigger decision can be made. The circuitry is divided into four *blocks*. The left and right ends of the E and dE scintillators each form a block as shown in figure 2-9. The photomultiplier bases provide a charge and voltage output. The charge output is delayed (~ 160 ns), to match in time the wire chamber information, then integrated at the ADC (Analog to Digital Converter). The voltage output is fed into a discriminator. The discriminator output is fed into a 24 input multilogic unit or MLU.

The 24 input MLU acts as a coincidence unit for a block. A minimum multiplicity ranging from 1 to 4 must be present in order to satisfy the coincidence. The selection of the required multiplicity is made using a 4-position switch (or quad-switch). No selection as to which phototubes in particular go into satisfying the coincidence is possible. Only the number of phototubes can be specified. The quad-switch on the 24 input MLU's determines the *block trigger*.

The output from each 24 input MLU is fed into a 4 input MLU. The 4 input

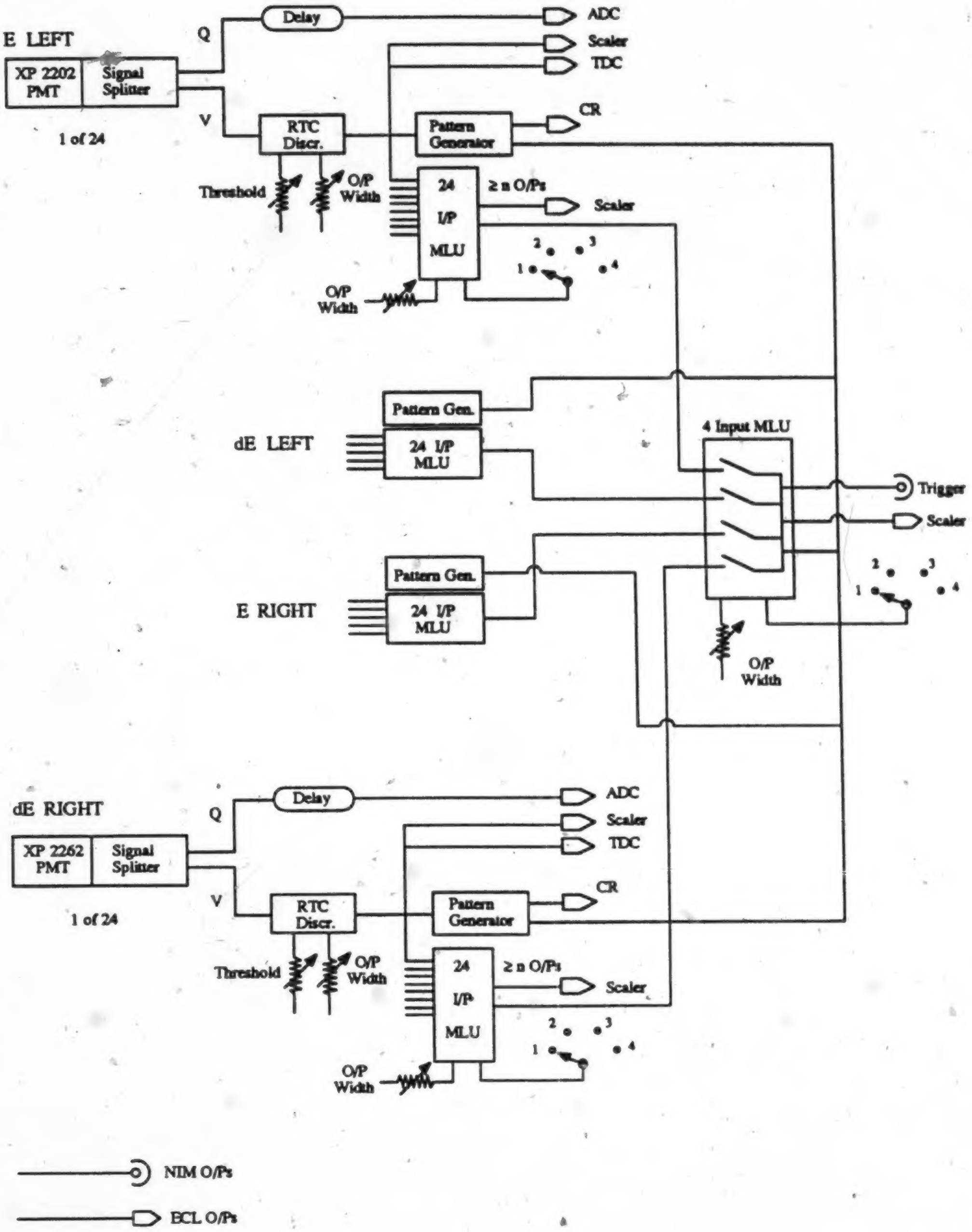

Figure 2-9

SALAD Scintillator Circuitry and Trigger Logic

MLU acts as a coincidence unit for the four blocks. Again the required multiplicity can be set from 1 to 4. A block trigger can be enabled or disabled by closing or opening its corresponding toggle switch on the 4 input MLU. An event trigger is obtained only when a sufficient number of enabled block trigger signals are present to satisfy the multiplicity condition selected on the 4 input MLU quad switch.

CHAPTER 3

SALAD SCINTILLATOR PION TESTS

A) Introduction

SALAD will be used to study photonuclear interactions at the Saskatoon Accelerator Laboratory (SAL). Many experiments will involve the production of pions. The p(p,p)p scattering tests of chapter 4 were performed at $E_p = 220$ MeV. This is below the pion threshold of 287.5 MeV via $p(p,\pi^+)d$. Thus it was necessary to test the response of the SALAD scintillators to pions in a separate experiment. This testing provided an opportunity to determine both the energy resolution and light attenuation of the SALAD E and dE scintillators.

B) Procedure

Two SALAD E-dE scintillator pairs were tested at TRIUMF on the high luminosity low energy pion channel M13. The layout for M13 is shown in figure 3–1(15). One SALAD scintillator pair was placed above the other with the final focus F3 of the pion beam directed at the pair below as shown in figure 3-2. Before reaching the SALAD scintillators the beam passed through a 12.7 cm x 12.7 cm multiwire proportional chamber and a 2 cm wide x 3 cm tall x 0.318 cm thick scintillator (this will be referred to as the 'Beam' Scintillator). These were used to monitor the beam profile and intensity. During transportation of the scintillators to TRIUMF two photo-multiplier tubes were damaged. Run time was limited so no on site repairs were possible. As a result there is no data for either the left end of the dE scintillator below and the right end of the E scintillator above. The 'below' and 'above' orientation is shown in figure 3-2. The 'left' and 'right' orientation was chosen as shown in figure 3-7.

The M13 channel was initially set for π^+ of kinetic energy 65.0 MeV (momentum = 149.6 MeV/c). In subsequent measurements lower beam energies were chosen by altering the magnetic fields of dipoles B1 and B2 via computer control to

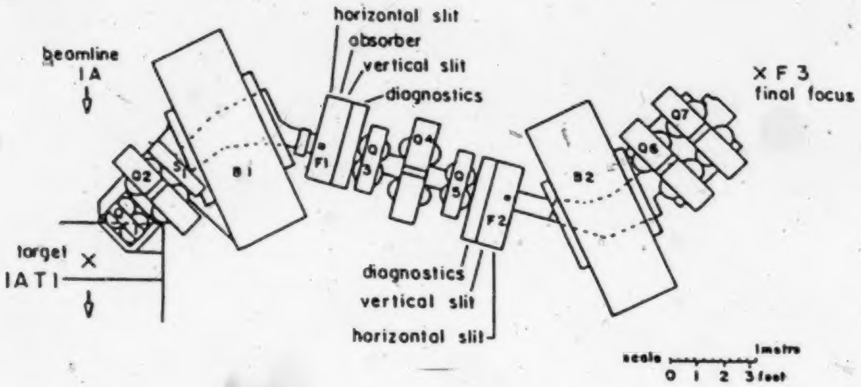

Figure 3-1 Beam Line M13 (Modified from C. Oram et al. NIM 75 (1981) 95).

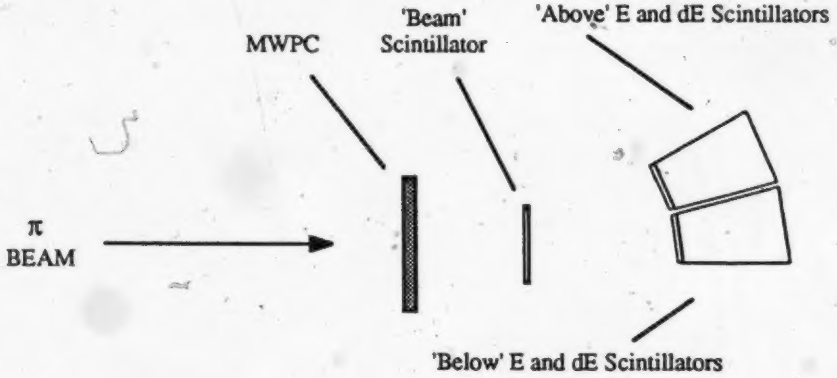
MWPC
'Beam' Scintillator
'Above' E and dE Scintillators
π
BEAM
'Below' E and dE Scintillators

Figure 3-2
Orientation of the Wire Chamber and Scintillators Relative to the Pion Beam.

select various percentages of the initial momentum. The pion momenta, kinetic energies, velocity and flight times between the pion production target 1AT1 and the SALAD scintillators are listed in table 3-1. Flight time calculations are discussed in appendix B-II.

In table 3-2 the energy lost by the pions in the various scintillators as

Table 3-1

Pion Data for SALAD Scintillator Tests.

Pion Momentum (Mev / c)	Pion Kinetic Energy (MeV)	Pion Velocity $v\pi/c$	Time of Flight Through M13 Channel (ns)
149.6	65.0	0.73	42.0
145.8	62.3	0.72	42.6
127.1	49.2	0.67	45.8
104.7	34.9	0.60	51.1
77.8	20.2	0.49	62.6

calculated by the program LOSSPROG(13) is given. The energy loss was calculated assuming that the energy loss properties of the Bicron Corporation scintillators are approximated accurately by the compound CH_2 of density $\rho = 1.032$ g / cm^3. Values in parenthesis in table 3-2 indicate remaining beam energy. The energy loss in the multiwire proportional chamber is negligible compared to the plastic scintillators and so is not included in table 3-2.

Table 3-2

Kinetic Energy Lost by the Pions in the Beam, dE and E Scintillators (Remaining Kinetic Energy in Parenthesis).

Pion Energy (MeV)	Energy Lost in Beam Scintillator (MeV)	Energy Lost in dE Scintillator (MeV)	Energy Lost in E Scintillator (MeV)
62.3	1.0 (61.3)	1.0 (60.3)	60.3
49.2	1.2 (48.0)	1.2 (46.8)	46.8
34.9	1.4 (33.5)	1.5 (32.0)	32.0
20.2	2.1 (18.1)	2.3 (15.8)	15.8

The front end electronics for the SALAD scintillator tests is shown schematically in figure 3-3. An event is triggered by a triple coincidence between the beam scintillator, the below dE-Right scintillator (since the dE-Left photomultiplier tube was not functional) and one end of the below E scintillator. The prefix 'A' is given to the ADC data related to the scintillator pair above the pair hit directly by the beam. The letters 'P' and 'D' following a data name indicate 'prompt' or 'delayed' ADC

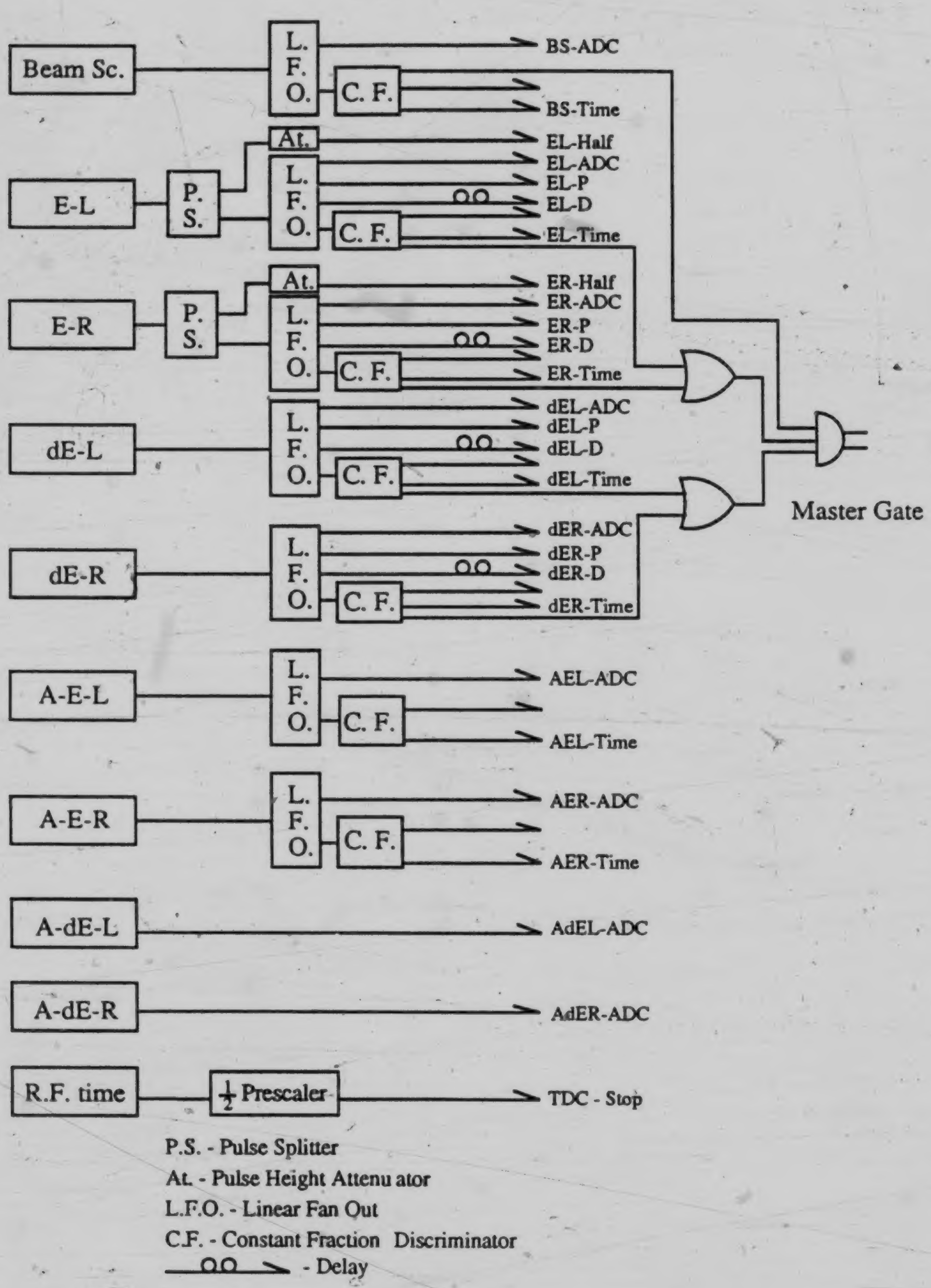

Figure 3-3

Front End Electronics for the SALAD Scintillator Pion Tests.

data. 'Half' indicates the signal attenuator was set to 0.5. The prompt and delayed data is used for π^+ / π^- separation studies which will not be discussed here.

The TDCs are started by the event trigger and are stopped by the cyclotron RF (radio frequency) pulse prescaled by one half. The analog to digital converters were set to give ~ 0.25 pC / channel. The linearity of the 1024 channel ADC was confirmed using the attenuator.

The beam and dE scintillator gains were set using a collimated ^{60}Co source. The 1.2 MeV γ rays give a Compton edge energy of ~ 1 MeV. As shown in table 3-2 this is approximately equal to the energy lost by the 62.3 MeV pions in both the beam and dE scintillators. The voltages of the beam and dE photomultiplier tubes were set so that the Compton edge gave a 200 mV pulse which corresponded to ~ 130 ADC channels. Minimum ionizing particles deposit ~ 0.6 MeV in the thin scintillators and give a ~ 120 mV pulse which is well above the discriminator thresholds which had been set at 50 mV.

The SALAD E scintillator gains were matched by placing the ^{60}Co source at the midpoint and adjusting the photomultiplier high voltages at each end to give a 50 mV pulse. This ensured that the more energetic pions would give pulses above the discriminator threshold. When the 62.3 MeV pion beam struck the E scintillator at its midpoint the E_{Right} and E_{Left} energy peaks were both in ADC channel ~ 500. The 20.2 MeV pions gave E_{Right} and E_{Left} energy peaks in ADC channel ~100. Thus the range of ADC channels available accommodated the range of pion energies studied. The analysis package *PERSEUS*(16) was used to study the SALAD scintillator pion test data.

C) Results

I) Beam Profile

The beam profile was monitored by the multiwire proportional wire chamber. A typical profile is shown in figure 3-4 for E_π = 20.2 MeV. Since it is important to know the position where the pions stop in the SALAD scintillators, cuts are made on the beam profile spectra. The cuts were chosen to limit the cross-sectional area of the beam while utilizing most of the events. The beam profiles vary slightly with beam energy so the cuts applied also vary slightly. The size of the beam is determined

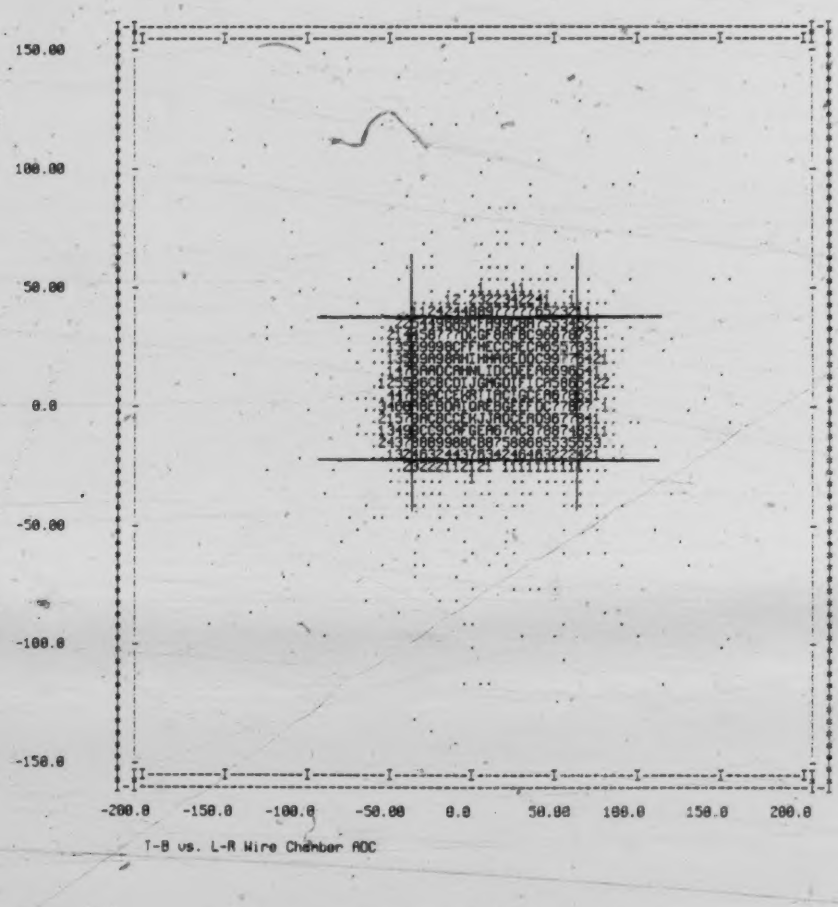

Figure 3-4 A Typical Beam Profile.

from the MWPC wire spacing which was 1 mm. The average beam size used in the following studies is ~15 mm wide x ~10 mm tall. The cuts applied to the 20.0 MeV beam profile are shown in figure 3-4.

II) Time of Flight Spectra

The time of flight of the beam relative to the cyclotron RF was measured. These 'TRF' spectra for pion beam energies of 20.2, 34.9, 49.2 and 62.3 MeV are shown in figure 3-5. Beam profile cuts have been applied to these spectra. The TDC start is the event trigger, and the TDC stop is the cyclotron RF divided by 2. The division by 2 gives a stop as much as twice the cyclotron period after the start. This allows a complete RF cycle to be observed without distortion from the edges of the coincidence overlap in the event trigger hardware.

The 20.2 MeV spectrum shows three distinctly separate peaks indicating a multiparticle beam composition. Pions, muons and positrons are produced at the T1 pion production target. Muons and positrons also come from subsequent pion decays. (positively charged pions decay predominantly into positively charged muons via $\pi^+ \rightarrow \mu^+ + \nu_\mu$ with a mean lifetime of 26.02 ns and positively charged muons decay into positrons predominantly via $\mu^+ \rightarrow e^+ + \nu_\mu + \nu_e$ with a mean life time of 2.20 µs). The kinematics of the pion decay is given in appendix B-II. The momentum of the various particles in a given TRF spectrum is the same as determined by the B1 and B2 dipole combination. Pions are expected to be the most abundant particle in the TRF spectra so we tentatively identify the largest peaks in the TRF spectra as pions, the second largest peak as muons and the smallest as positrons.

The TRF spectra represent the time of arrival of the particles at the SALAD scintillators relative to the cyclotron RF. This includes the time T_p taken for the protons to exit the cyclotron and strike the T1 pion production target. For all pion energies studied the proton energy is constant. For a given pion energy, the first pion peak corresponds to a time $T_1 = T_p + T_\pi$ where T_π is the time of flight of the pion through the M13 channel. The second pion peak corresponds to a time $T_2 = T_1 + T_{RF}$ where T_{RF} is the RF period of the cyclotron. The difference in time between these two

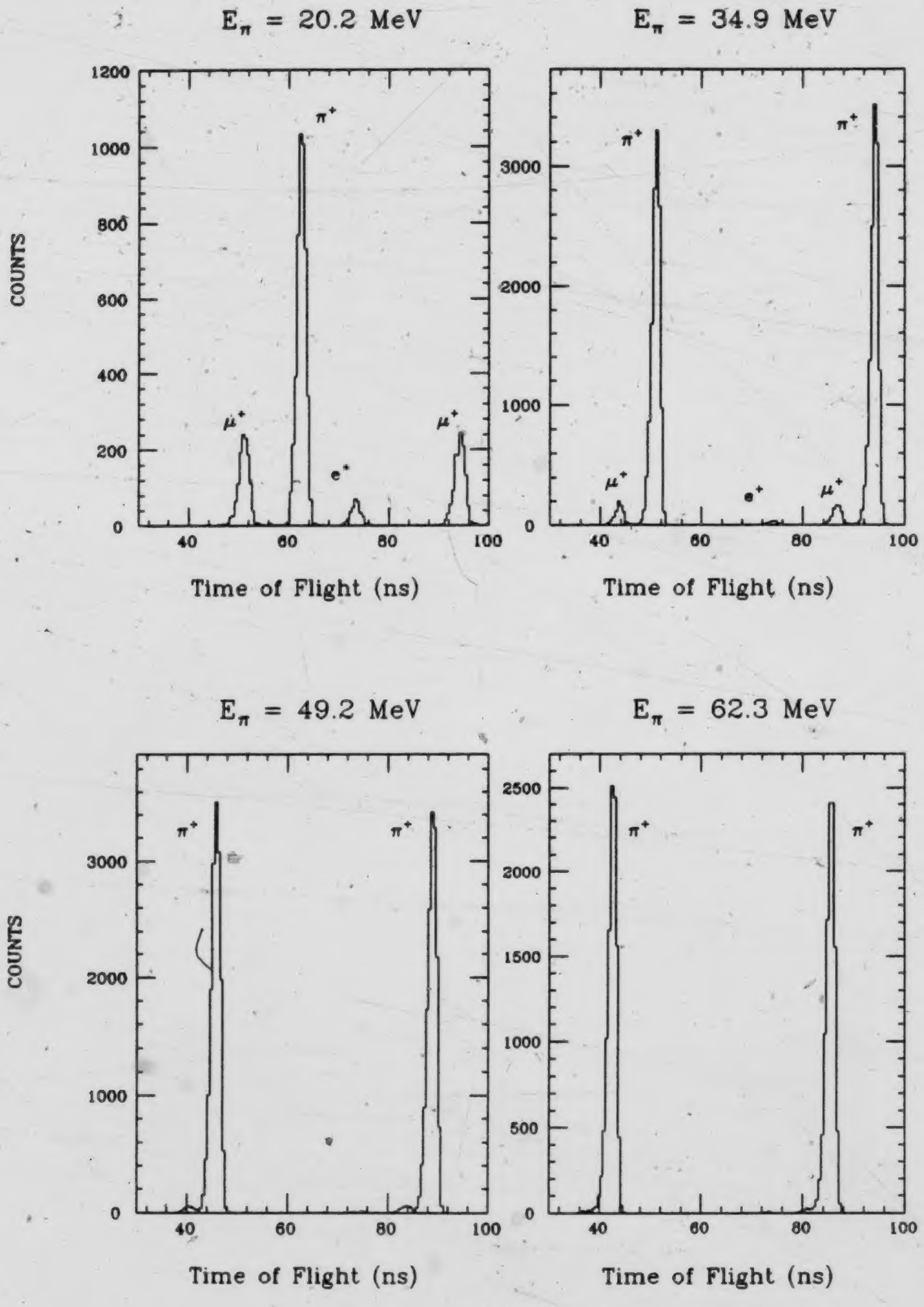

E_π = 20.2 MeV

E_π = 34.9 MeV

E_π = 49.2 MeV

E_π = 62.3 MeV

Figure 3-5 TRF Spectra for the Various Pion Beam Energies.

peaks is then T_{RF} which is 43 ns. This allows a calibration of the time axis on the TRF spectra. The calibration scale is the same for all three TRF spectra displaying two pion peaks and can be safely applied to the 20.2 MeV spectrum. The time given for the first pion peak in each TRF spectrum is the time of flight of the pions through the M13 channel for that energy as given in table 3-1. The time T_p is the same for all spectra and so has been subtracted out.

The muons observed in the TRF spectra come from the T1 production target and from pions that decay in the vicinity of the target. In appendix B-II the time of flight of the pions and muons through the M13 channel is calculated assuming both particles come from the T1 target. From these values the difference in flight time can be determined. The calculated differences are consistent with the observed differences in figure 3-5 confirming the assumed identification of the peaks.

These TRF spectra allow cuts to be made on the pions which are the particle of interest for the following studies. At the two highest beam energies there is no distinct separation between the pions and muons as the two distributions begin to overlap. Thus these pion cuts do not eliminate all muons. However, tight cuts can still eliminate the majority of muons, and because the ratio of muons to pions at these higher energies is very small, any muons missed by the cuts will not influence the results of the following studies.

III) Beam Scintillator Spectra

The energy deposited by the particles in the 'beam' scintillator at 20.2, 34.9, 49.2 and 62.3 MeV is shown in figure 3-6. Beam profile cuts have been applied to these histograms. The energy scale has been calibrated by associating the ADC value of the pion peak in each spectrum with the energy loss values of table 3-2. A linear fit to the four data points was done showing 1 ADC channel corresponds to 0.0125 MeV. The linear regression equations used are given in appendix B-III.

The multiple peak structure of the 20.2 MeV spectrum is interesting. Placing cuts on each particle in the 20.2 MeV TRF spectrum shows that the tallest peak in the energy spectrum corresponds to pions, and the smallest peak corresponds to positrons.

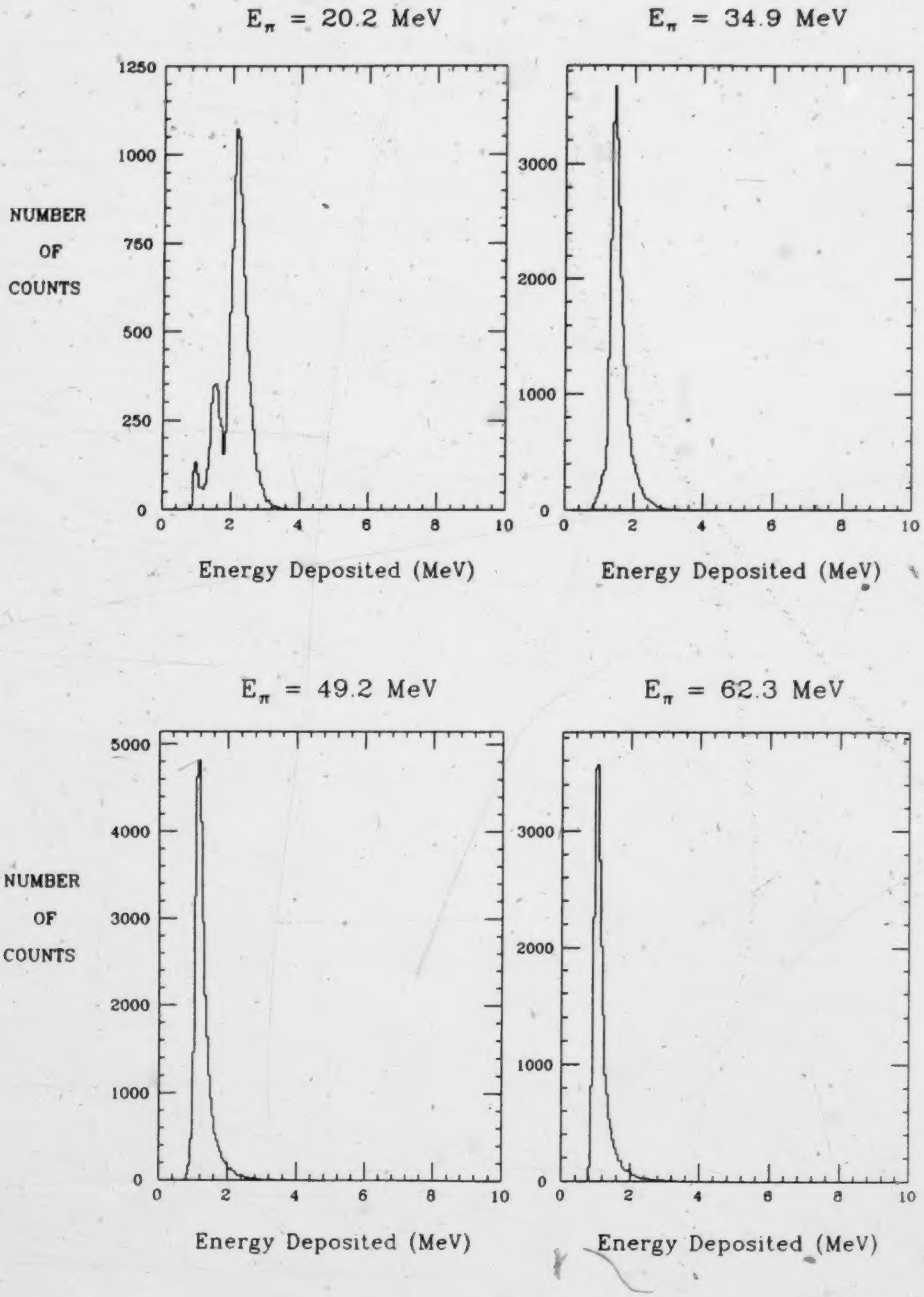

Figure 3-6

Beam Scintillator Spectra for the Four Pion Beam Energies.

This spectrum shows that pions lose more energy in the thin beam scintillator than do muons of the same momentum. This observation is verified by calculations described in appendix B-IV. The calibrated energy scale shows the mean energy deposited in the beam scintillator by the muons is 1.48 MeV. A LOSSPROG calculation gives the same result. This indicates the energy scale is calibrated correctly and reconfirms the identification of the three peaks in the TRF spectra

The individual peaks are no longer separated for pion beam energies of 34.9 MeV and higher. Only a small protrusion to the left of the pion peak is noticeable. As the pion energy increases this protrusion is reduced for two reasons. First, the energy lost by the various particles is approaching the same minimum ionizing value causing the peaks to move closer together, and second, the number of muons and positrons decreases relative to the number of pions as shown in the TRF spectra. When the pion energy reaches 62.3 MeV the protrusion is negligible.

The energy loss distribution in the beam scintillator spectra is observed to be consistent with a Landau distribution. The characteristic high energy tail of this distribution is due to the infrequent interactions that result in a large amount of energy lost by the pions. A Gaussian distribution is not expected as shown in appendix B-V. The beam scintillator is too thin for pions of these energies to give a Gaussian distribution.

IV) Light Attenuation and Collection

The procedure for measuring the light attenuation of the SALAD E and dE scintillators is as follows. The scintillators were illuminated at various locations along their length with a pion beam of constant energy (E_π = 62.3 MeV). The location of the beam relative to the left and right ends of the scintillators is shown in figure 3-7. To prevent ADC overflows when the particles stop near the end of the scintillator, a signal attenuator was placed between the photomultiplier tubes and the Analog to Digital Converter. The attenuator was set to reduce the pulse heights by a factor of $\frac{1}{2}$. The 'half height' data is used for all beam positions.

When an energetic pion stops in a scintillator, a number N_0 of photons are

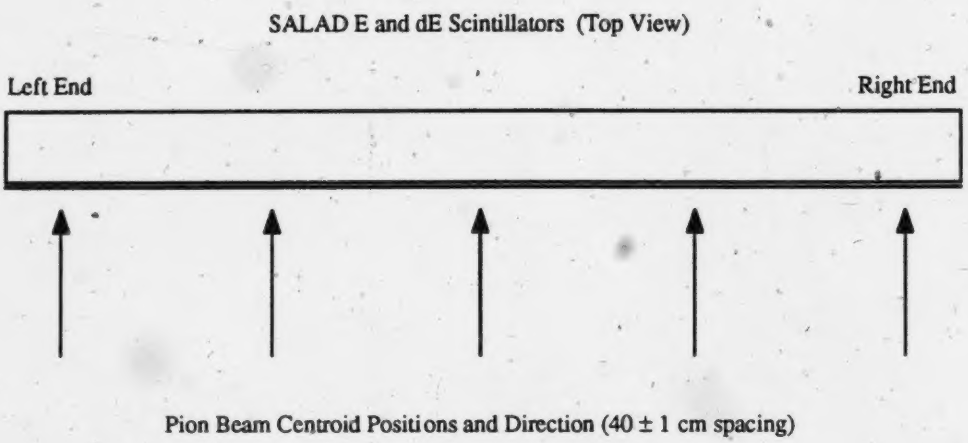
SALAD E and dE Scintillators (Top View)
Left End
Right End
Pion Beam Centroid Positions and Direction (40 ± 1 cm spacing)

Figure 3-7
62.3 MeV Pion Beam Positions Relative to the SALAD Scintillators for Light Attenuation Measurements.

produced. As outlined in appendix B-VI, the ADC value recorded for this event by one end of the scintillator is related to N_0 by,

$$\mathrm{ADC} = \alpha N_0 e^{-\mu l} \quad , \qquad (3.1)$$

where l is the distance between the end of the scintillator and the point where the photons originate, μ is the attenuation coefficient of the scintillator and α is a factor that depends on the light collection efficiency at the end of the scintillator and on the external electronics which includes the photomultiplier amplification and the analog to digital conversion.

To make an accurate estimation of the light attenuation and light collecting efficiency of the SALAD scintillators a mono-energetic sample of pions is needed. This will ensure that N_0 remains the same for each beam position. Making pion cuts on the TRF spectra ensures that only pions are studied. Energy cuts on the beam scintillator spectra which remove the high energy tail ensure that pions of as narrow an energy range as possible are studied. For the E scintillator attenuation and light collection studies, energy cuts similar to those made on the beam scintillator spectra are made on the SALAD dE scintillator spectra (these spectra are shown in figure

3–14 and are discussed in section C-VI). To ensure that the location of the pions relative to the end of the scintillators are known, beam profile cuts are made. As stated in section C-I, the average beam size is ~15 mm x ~10 mm.

The centroid of the half height ADC distributions are recorded for each beam position and are shown in table 3-3. The standard deviation σ of each distribution can be calculated using(17)

$$\sigma^2 = \frac{1}{N-1}\sum_{i=1}^{N}(x_i - \bar{x})^2 \quad , \qquad (3.2)$$

where the sample mean $\bar{x}$ is given by

$$\bar{x} = \frac{1}{N}\sum_{i=1}^{N} x_i \quad .$$

However, all of the data should not be included in these calculations because the width of these distributions are increased by both the momentum spread of the pion beam and the energy released from πN interactions. Evidence for these contributions is shown in figure 3-8. The energy collected by the left end of the E scintillator is plotted against the energy collected by the right end for a pion beam of energy $E_\pi = 62.3$ MeV which strikes the middle of the scintillator. The energy scales have been calibrated using a pion beam of four different energies directed at the midpoint of the E scintillator. The light collecting properties of the left and right ends of the E scintillator are symmetric about the midpoint of the scintillator in terms of both geometry and light attenuation. Since the pions stop in the middle of the scintillator it is assumed that an equal number of photons are collected at each end (see appendix B-VI). With the photomultiplier gains matched in software, the left and right ADC centroid values are assigned half the pion kinetic energies stated in table 3-2. A linear fit of the four pion energies to their corresponding ADC centroids gives the energy scale shown in figure 3-8.

The energy of any point on the histogram is found by adding the left and right energies. The momentum spread of the pion beam smears the data out along a diagonal. On this diagonal energies as high as ~140 MeV (approximately the rest mass of the pion) are observed. This is an indication that some nuclear interactions

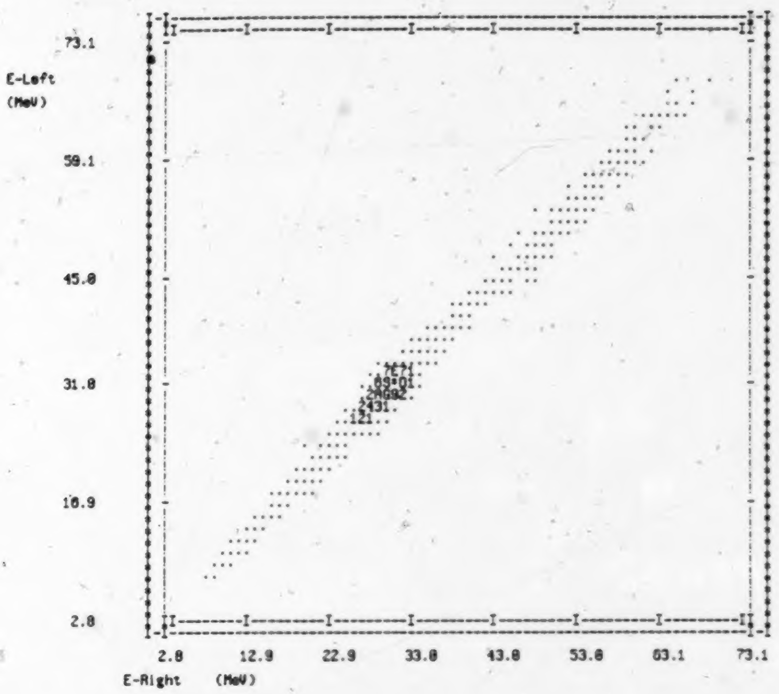

Figure 3-8
Energy Measured by the Left vs. Right Ends
of the SALAD E Scintillator (Beam Energy = 62.3 MeV).

take place in the scintillator in which the pion is annihilated. The momentum spread is, however, the dominant effect.

To find the standard deviation of the E_{Right} distributions without the contribution from the momentum spread of the beam, horizontal cross sections are made in figure 3-8 at the E_{Left} energy corresponding to half the energy deposited in the E scintillator. To find the standard deviation of the E_{Left} distributions, vertical cross sections are made at the appropriate E_{Right} energy. This is done for each beam position. The standard deviation of the resulting one dimensional histograms are calculated using equation 3.2. The results are the centroid errors given in table 3-3.

A similar two dimensional histogram cannot be made for the dE scintillator since data is not available for the left end. Instead a two dimensional histogram in which the total energy deposited in the E scintillator is plotted against the energy

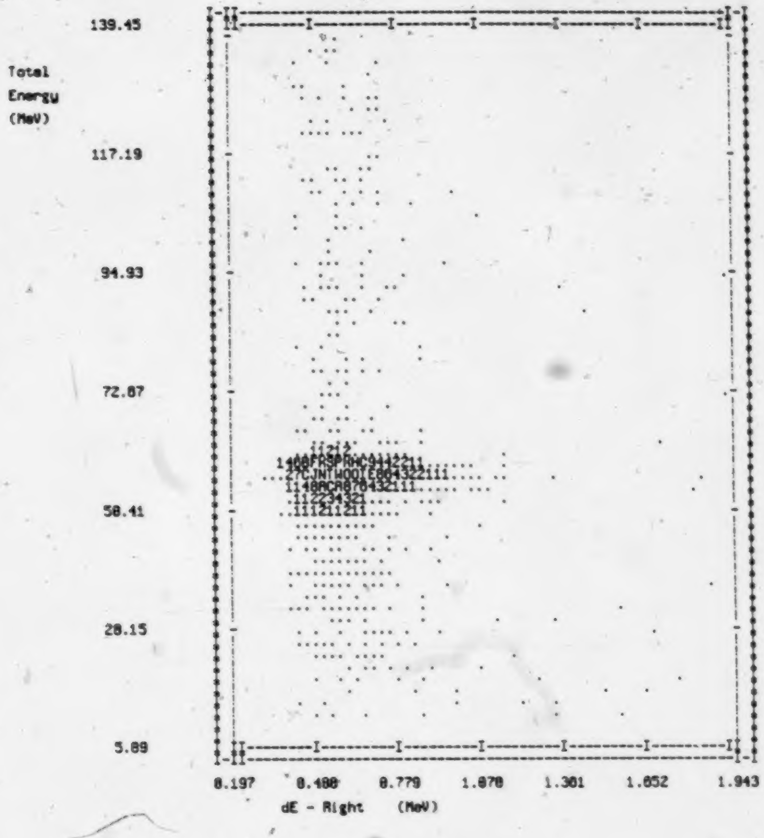

Figure 3-9
Energy Measured by E Scintillator vs. the Right End
of the SALAD dE Scintillator (Beam Energy = 62.3 MeV).

measured by the right end of the dE scintillator. This is shown in figure 3-9. The energy scales are also calibrated using the four pion beam energies with the beam directed at the midpoint of the scintillators. The dE_{Right} ADC centroid values are assigned half the energy deposited in the dE scintillator as stated in table 3-2. A linear fit of the four energies to their corresponding ADC centroids gives the dE energy scale shown. The half height E_{Left} and E_{Right} ADC values are combined as outlined in appendix B-VI to give a position independent ADC_{Total} value. The E_{Total} energy scale is calibrated by associating the ADC_{Total} centroid values with the energy deposited in the E scintillator as stated in table 3-2. A linear fit to the four pion energies gives the total energy scale shown.

Figure 3-9 shows that the energy spread in the pion beam does not spread the dE scintillator data out along a diagonal as it does for the E scintillator data. However, to analyze the dE_{Right} data for only E_{Total} = 60.3 MeV, horizontal cross sections are made to figure 3-9 at this energy. This is done for each beam position. The standard deviation of the resulting one dimensional histograms are calculated using equation 3.2. The results are the centroid errors given in table 3-3.

Table 3-3 ADC Centroids as a Function of Beam Position.

Distance Between Beam and Scintillator End (± 1.8 cm)	E Scintillator (Left End)	E Scintillator (Right End)	dE Scintillator (Right End)
10.0	280 ± 10	240 ± 10	203 ± 31
50.0	265 ± 9	249 ± 9	174 ± 38
90.0	227 ± 8	228 ± 8	125 ± 35
130.0	195 ± 8	197 ± 8	85 ± 28
170.0	166 ± 7	167 ± 7	64 ± 21

To find the attenuation coefficients of the scintillators we take the natural logarithm of equation 3-1. This gives,

$$\ln(\mathrm{ADC}) = -\mu l + \ln(\alpha N_o) \ .$$

A graph of the natural log of the ADC values in table 3-3 as a function of l should be linear with a slope equal to the negative of the attenuation coefficient of the scintillator. The natural logarithms of the ADC values are shown in table 3-4 and are plotted in figure 3-10.

The slope of figure 3-10(a) is the attenuation coefficient of the E scintillator as determined from the left end data. This gives $\mu_L = (3.4 \pm 0.4) \times 10^{-3}$ / cm. The slope of figure 3-10(b) is the attenuation coefficient of the E scintillator as determined from the right end data. This gives $\mu_R = (2.4 \pm 0.6) \times 10^{-3}$ / cm. Taking a weighted average of the left and right ends gives an attenuation coefficient for the E scintillator of

Table 3-4 Natural Logarithms of ADC Centroids for Each Scintillator End.

Distance Between Beam and Scintillator End (± 1.8 cm)	E Scintillator (Left End)	E Scintillator (Right End)	dE Scintillator (Right End)
10.0	5.63 ± 0.04	5.48 ± 0.04	5.31 ± 0.15
50.0	5.58 ± 0.03	5.52 ± 0.04	5.16 ± 0.22
90.0	5.42 ± 0.04	5.43 ± 0.03	4.83 ± 0.28
130.0	5.27 ± 0.04	5.28 ± 0.04	4.45 ± 0.33
170.0	5.11 ± 0.04	5.12 ± 0.04	4.16 ± 0.33

$\mu_E = (3.1 \pm 0.3) \times 10^{-3}$ / cm. Referring to equation 3.1, the attenuation length $\lambda = \frac{1}{\mu}$ is the length over which N_o is reduced by a factor of $\frac{1}{e}$. For the E scintillator the attenuation length is $\lambda_E = 323 \pm 31$ cm. The attenuation coefficient of the dE scintillator is found from the slope of figure 3-10(c). This gives $\mu_{dE} = (7.5 \pm 2.3) \times 10^{-3}$ / cm. The attenuation length of the dE scintillator is then $\lambda_{dE} = 133 \pm 41$ cm.

The attenuation lengths of a sheet of plastic scintillator (BC412) of fixed width and length (12 cm x 200 cm) but varying thickness have been measured by the manufacturer(18). For the thicknesses 5 mm, 10 mm and 20 mm the attenuation lengths were found to be 195 cm, 212 cm and 275 cm respectively. The SALAD E scintillator of dimensions 12.7 cm wide x 183 cm long x 76 mm average thickness was found to have an attenuation length of 323 ± 31 cm. The SALAD dE scintillator of dimensions 5.8 cm average width x 180 cm long x 3.2 mm thick was found to have an attenuation length of 133 ± 41 cm. Both of these results are reasonable based on the manufacturer's results.

The attenuation lengths of the E and dE scintillators are quite different even though they are made of the same material. The inherent clarity of a scintillator to its own fluorescent light is known as its bulk attenuation. The E and dE scintillators have the same bulk attenuation length. However, the measured attenuation length of a scintillator is some fraction of its bulk attenuation length depending on its shape and the smoothness of its surfaces. For many scintillator geometries, the light reflects internally many times before reaching the phototube (as in the case of the thin dE scintillator). Thus, even though the light travels a relatively small distance lengthwise along the scintillator, the total distance traveled is much larger. A short thin

(a) E Scintillator (Left End)

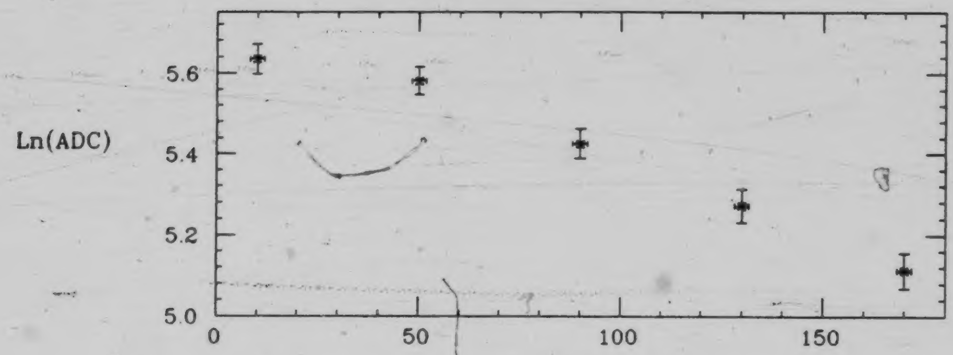

(b) E Scintillator (Right End)

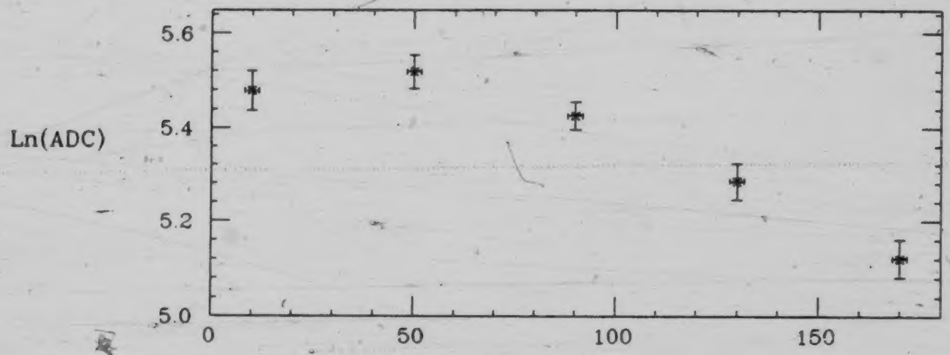

(c) dE Scintillator (Right End)

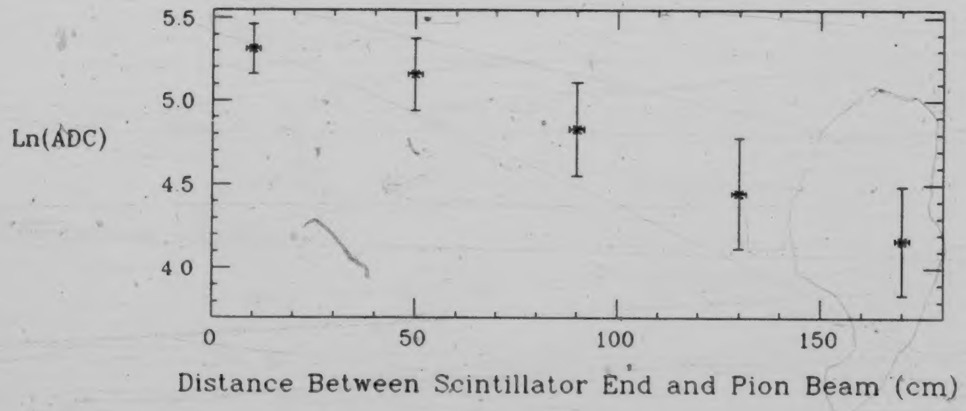

Figure 3-10 Log of ADC Centroid as a Function of Beam Position for the SALAD Scintillators.

scintillator will attenuate the light to the same extent as a longer thicker scintillator. Also, a fraction of the light can be lost through the side of a scintillator with each internal reflection. The amount of light lost depends on the smoothness of the surface with a highly polished surface giving the best internal reflection. This causes N_o to be reduced to $\frac{1}{e}N_o$ faster than by bulk attenuation alone. This problem is worse for a thin scintillator in which many internal reflections take place. Hence the attenuation length of a scintillator is smaller than its bulk attenuation length, and smaller still for thin scintillators.

To study the total light collection properties of the SALAD E scintillator as a function of position, the half height E_{Left} and E_{Right} ADC values are combined as outlined in appendix B-VI to give a position independent ADC_{Total} value. To eliminate the effects of the momentum spread of the pion beam, horizontal cuts are made to a two dimensional histogram of E_{Left} versus E_{Total}. The ADC_{Total} centroids and their standard deviations are found from the resulting one dimensional E_{Total} spectra. They are given in table 3-5 and shown in figure 3-11.

Table 3-5 Total Light Collected as a Function of Beam Position for the SALAD E Scintillator.

Beam Position from Center of E Scintillator (± 1.8 cm)	Centroid (ADC Channels)	I/I_{max} (%)
-80.0	216.3 ± 6.8	94.5 ± 3.9
-40.0	227.9 ± 6.3	99.6 ± 3.8
0.0	228.8 ± 5.9	100.0 ± 3.7
40.0	221.7 ± 7.1	96.9 ± 4.0
80.0	196.4 ± 6.2	85.8 ± 3.5

Overall, a very nearly uniform total light collection is observed. The poor result for the right end (80.0 ± 1.8 cm position) is due to the anomalously low value of the ADC centroid for the right end as shown in table 3-3. This low value is unusual. The initial number of photons produced in the scintillation process is the same for this beam position as for the other positions. This is indicated by the

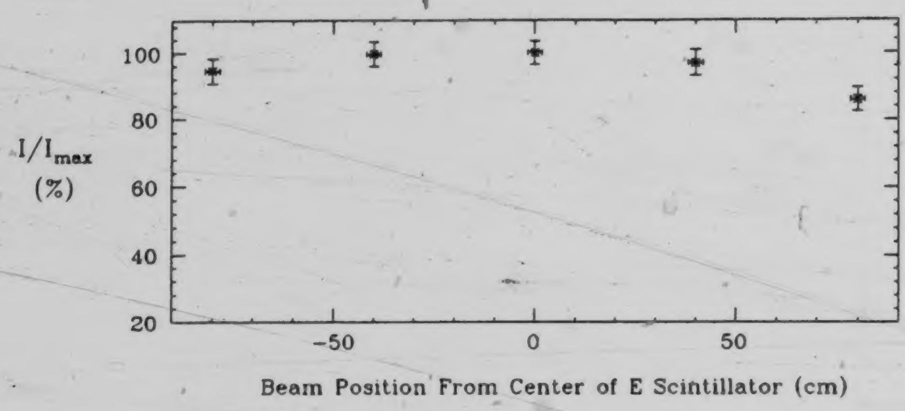

Figure 3-11 Total Light Collected
in the SALAD E Scintillator as a Function of Position.

consistent result for this position in the E_{Left} data. An obstruction in light transmission may be the cause, but this would affect the data for all beam positions, not just the end position. The symmetry in the light collection of the left and right ends seems to indicate that the suspect value is a result of electronics and not the result of a problem in the light collection of the E scintillator. A total light collection study could not be made for the dE scintillator since data from the left end is not available.

V) *SALAD E Scintillator Energy Resolution*

To make an accurate estimation of the energy resolution of the SALAD scintillators a mono-energetic sample of pions is needed. Making pion cuts on the TRF spectra ensure that only pions are studied. Energy cuts on the beam scintillator spectra which remove the high energy tail ensure that pions of as narrow an energy range as possible are studied. For the E scintillator studies, energy cuts similar to those made on the beam scintillator spectra are made on the SALAD dE scintillator spectra (these spectra are shown in figure 3-14 and are discussed in section VI).

These cuts as well as the usual beam profile cuts are made for all the energy resolution studies.

The energy deposited by the pions in the E scintillator for the four pion beam energies is shown in figure 3-12. The energy scale has been calibrated by associating the position independent ADC value (see appendix B-VI) of the pion peak in each spectrum with the energy loss values of table 3-2. A linear fit to the four data points gives the energy scale shown.

It is straight forward to determine the Full Width at Half Maximum (FWHM) values of each histogram in figure 3-12 and hence determine the energy resolution of the E scintillators as a function of energy. However, as observed in the light attenuation studies, the pion beam is not monoenergetic. The width of these distributions is greater than that due to the energy resolution alone. To bypass this problem and measure the intrinsic energy resolution of the E scintillator, a two dimensional histogram of the energy measured by the left end is plotted against the total energy measured. A composite of all four pion energies is shown in figure 3-13. The vertical axis is calibrated as in figure 3-8 and the horizontal axis is calibrated as the vertical axis in figure 3-9 except the half height data is not used.

The diagonal shape is again caused primarily by the momentum spread of the pion beam. It is the width of the diagonal that reflects the actual energy resolution of the E scintillator. To measure the energy resolution, four horizontal cross sections are made in figure 3-13 at the E_{Left} energies corresponding to half the pion energies deposited in the scintillator. The standard deviations of the resulting one dimensional total energy histograms are calculated using equation 3.2. Using the relation between the standard deviation and the FWHM of a normal distribution (FWHM $\approx 2.35\ \sigma$), the energy resolution for each energy is determined. The results are shown in table 3-6.

Table 3-6

SALAD E Scintillator Energy Resolution.

Pion Energy E (MeV)	Centroid (ADC Channels)	σ_E (ADC Channels)	σ_E (MeV)	FWHM (MeV)	Resolution %	$E_{Res}\% \cdot \sqrt{E}$
15.75	90.61	7.19	0.80	1.88	11.9	47.4
31.98	230.50	7.36	0.82	1.93	6.0	34.1
46.86	369.60	9.05	1.00	2.35	5.0	34.3
60.19	487.96	9.57	1.07	2.51	4.2	32.4

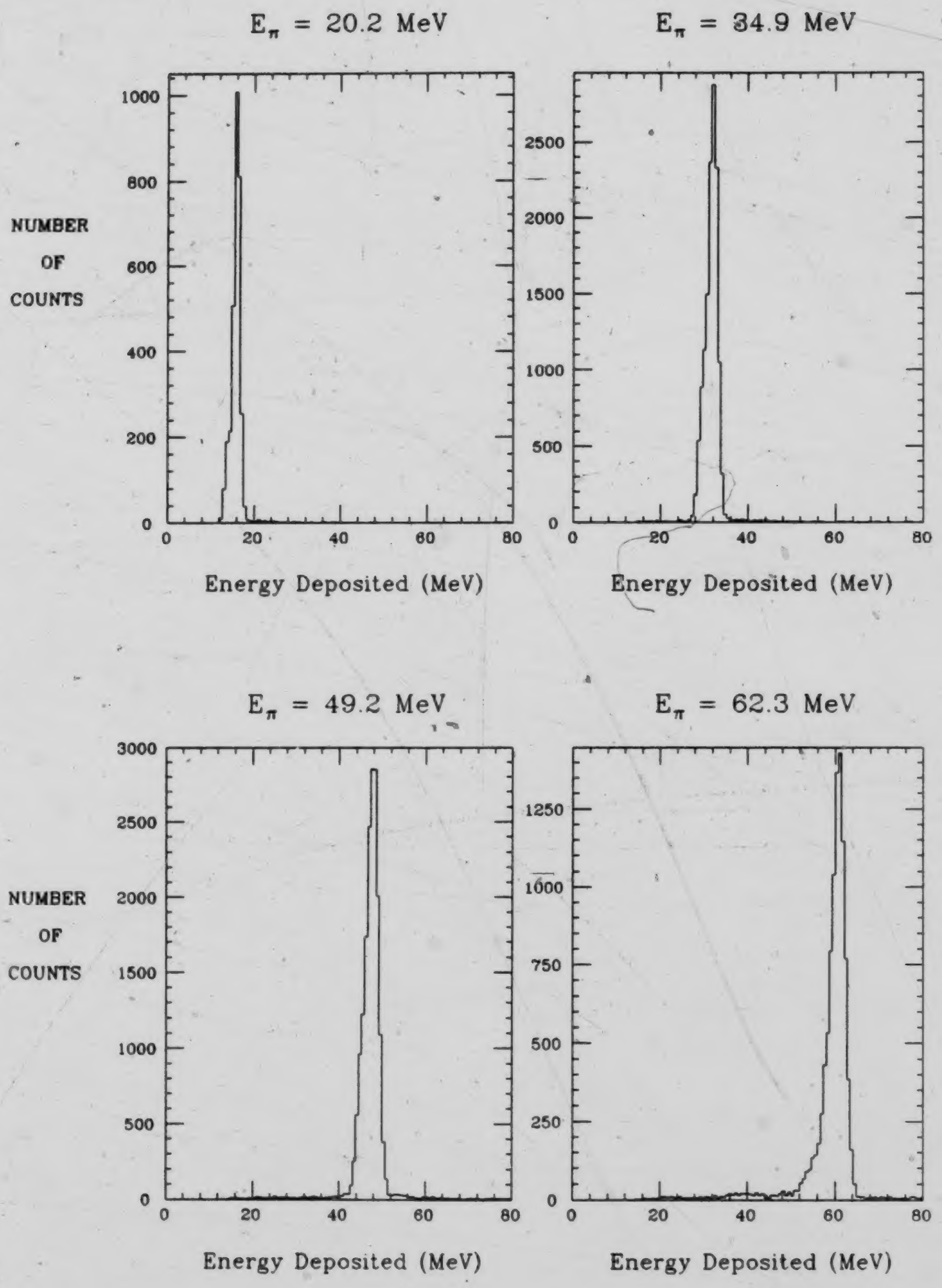

Figure 3-12

E Scintillator Energy Spectra.

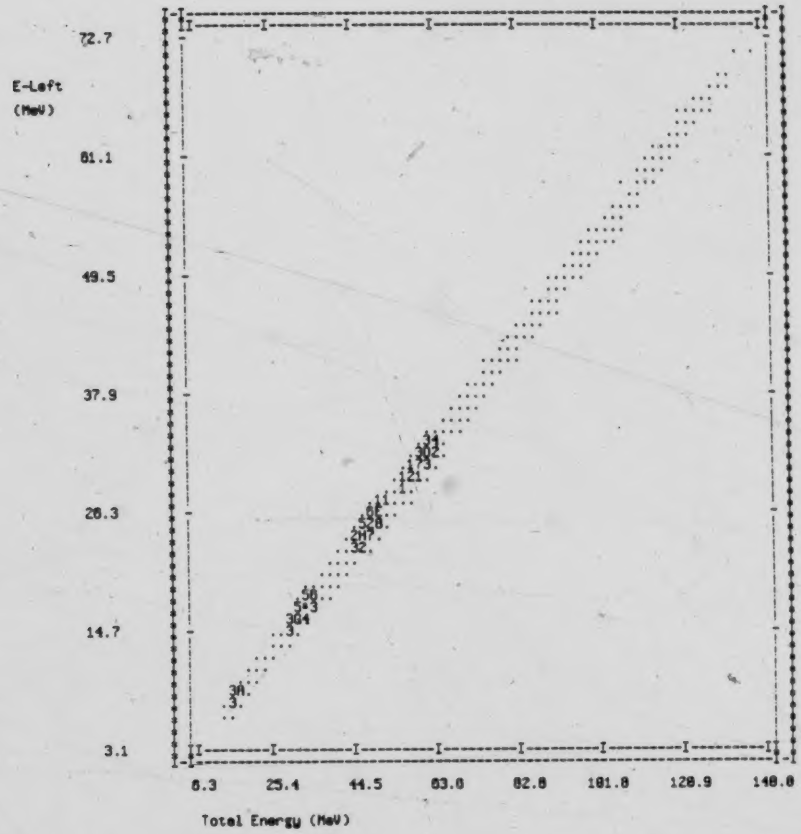

Figure 3-13

E_{Left} vs. Total Energy Measured in the SALAD E Scintillator.

The results for σ shown in table 3-6 depend slightly on how E_{Left} is binned. If the bin size is too small the number of counts / bin becomes too small reducing statistics. If the bin size is too large then a unique pion energy is not being selected. As shown in appendix B-VII, a $1/\sqrt{E}$ dependence of the energy resolution is expected. The values in the last column in table 3-6 are the product of the percentage energy resolution and the square root of the energy deposited in the scintillator. The E_{Left} bin size chosen gives consistent values of $E_{Res}\% * \sqrt{E}$ except for the 15.75 MeV case where the number of counts is low making this result unreliable. Taking a simple average of the last three values allows the energy resolution of the SALAD E scintillator to be written,

$$E_{Res} \approx \frac{33.6}{\sqrt{E}} \% \ .$$

The position dependence of the energy resolution is shown qualitatively in table 3-5. The nearly constant standard deviations of the ADC_{Total} centroids indicate that the energy resolution of the E scintillator is very nearly position independent.

VI) SALAD dE Scintillator Energy Resolution

As stated in the procedure, no data is available for the left end of the dE scintillator due to damage to the photomultiplier tube. The energy spectra for the right end of the dE scintillator are shown in figure 3-14. Beam profile, beam scintillator and pion cuts have been applied to these spectra. Since each end of the scintillator measures half of the total energy deposited, half of the energy values stated in table 3-2 are used to calibrate the energy scales in figure 3-14.

To analyze the dE_{Right} data for specific E_{Total} values, horizontal cuts are made to a two dimensional histogram of E_{Total} versus dE_{Right}. An example of this histogram is shown in figure 3-9. The ADC centroids and their standard deviations are found from the resulting one dimensional dE_{Right} spectra.

In attempting to predict what the centroid and variance (square of the standard deviation) of the *total* dE scintillator data would be if data from the left end was available, we will treat the dE data as though it were normally distributed. As in the case of the E scintillator, the light collecting properties of the dE scintillator are symmetric about its midpoint. Thus it is assumed that the dE_{Left} ADC values that would have been observed will have the same centroid and variance as the observed right ADC values. The centroid values of the total dE data are given by,

$$ADC_{dE} = ADC_{Left} + ADC_{Right}$$

With the above assumption this gives $ADC_{dE} = 2ADC_{Right}$. In general the standard

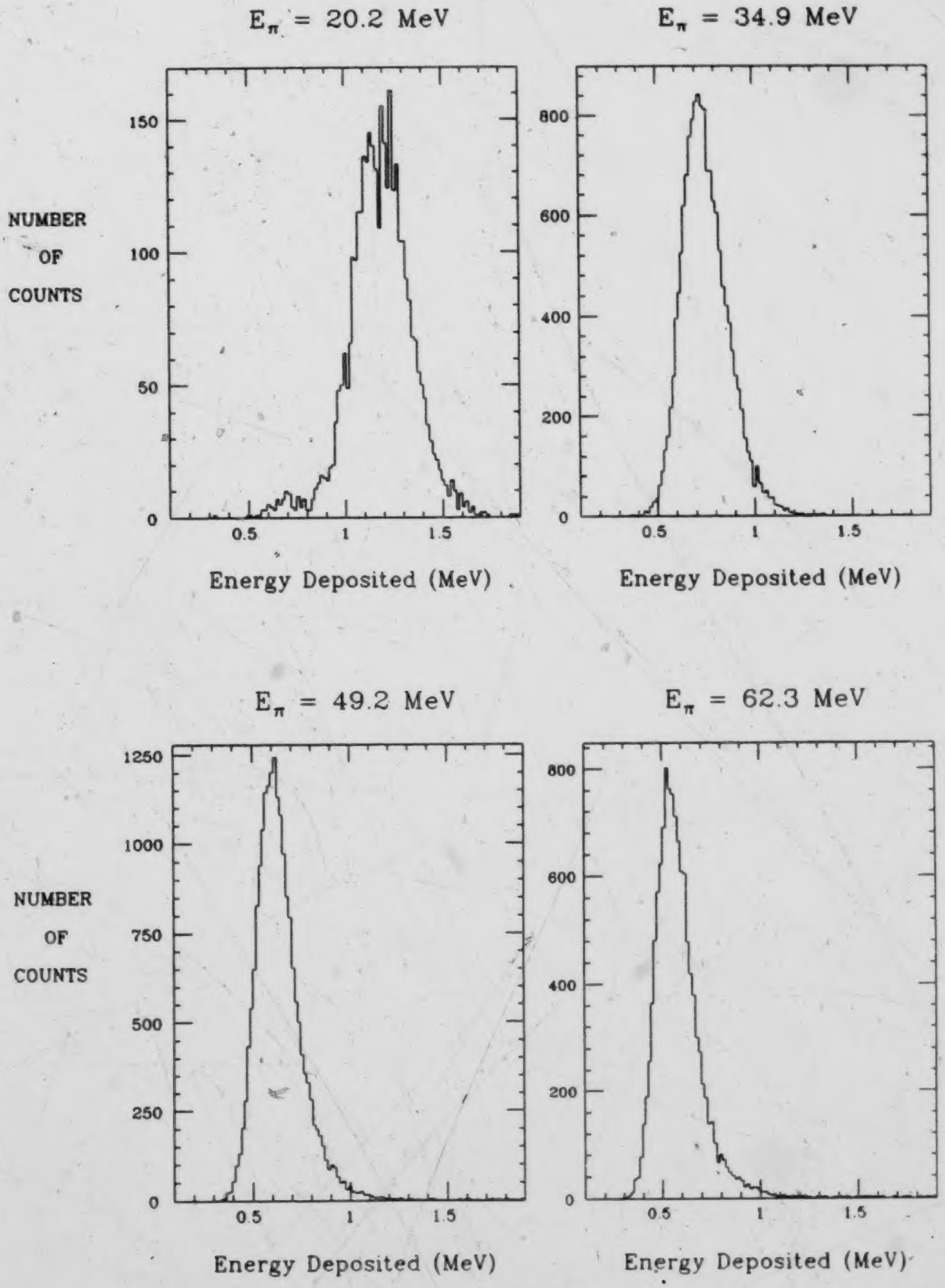

Figure 3-14

dE Right Scintillator Energy Spectra.

deviation of any quantity u can be calculated from$^{(19)}$

$$\sigma_u^2 = \left(\frac{\partial u}{\partial x}\right)^2 \sigma_x^2 + \left(\frac{\partial u}{\partial y}\right)^2 \sigma_y^2 + \ldots$$

where u = u (x, y, ...) and the quantities x, y, ... are independent. In this case,

$$\frac{\partial\, ADC_{dE}}{\partial\, ADC_L} = \frac{\partial\, ADC_{dE}}{\partial\, ADC_R} = 1$$

which gives

$$\sigma_{dE}^2 = \sigma_{Left}^2 + \sigma_{Right}^2$$

or with the above assumptions this reduces to $\sigma_{dE}^2 = 2\sigma_{Right}^2$. Using these relations gives the predicted total dE scintillator data shown in table 3-7.

Table 3-7
Expected Total dE Scintillator Data.

Energy Deposited E (MeV)	Centroid (ADC Channels)	σ_{dE} (ADC Channels)
2.33	670.82	65.04
1.48	350.62	52.43
1.19	274.60	47.82
1.05	241.16	45.19

With this data it is possible to deduce the energy resolution of the SALAD dE scintillators as a function of energy. Linear regression is used to convert ADC channels to an energy scale in MeV. The energy resolution of the dE scintillator is calculated for each energy. The results are shown in table 3-8.

The results for $dE_{Res}\% * \sqrt{E}$ in table 3-8 are very consistent. Had the data for the left end of the dE scintillator been available, an analysis method like that used on the E scintillator data could have been applied. However, as an estimate of the dE scintillator energy resolution, the average of the values in the last column of table 3-8

Table 3-8

SALAD dE Scintillator Energy Resolution.

Energy Deposited E (MeV)	σ_{dE} (MeV)	FWHM (MeV)	Resolution %	$dE_{Res}\% * \sqrt{E}$
2.33	0.19	0.45	19.2	29.3
1.48	0.15	0.35	23.8	29.0
1.19	0.14	0.33	27.6	30.2
1.05	0.13	0.31	29.1	29.8

is taken. The energy resolution of the dE scintillator is approximately given by,

$$dE_{Res} \approx \frac{29.6}{\sqrt{E}} \% \ .$$

CHAPTER 4

SALAD EFFICIENCY TEST

A) Introduction

The number of reaction products $\mathbb{N}(\theta)$ observed by a perfectly efficient detector in a given time interval t is given by,

$$\mathbb{N}(\theta) = \int R(\theta)\,dt \quad , \tag{4.1}$$

where $R(\theta)$ is the detection rate of a perfectly efficient 4π detector as given by equation 2.1. Because SALAD subtends a solid angle less than 4π steradians, and because not all particles within the acceptance are detected, the actual number of reaction products observed is $N(\theta)$ which is related to $\mathbb{N}(\theta)$ by

$$N(\theta) = \varepsilon'(\theta) \frac{d\Omega(\theta)}{2\pi \sin\theta \, d\theta} \mathbb{N}(\theta) \tag{4.2a}$$

where $\varepsilon'(\theta)$ is the probability that a particle passing through the acceptance of the detector will be detected. In practice, the efficiency $\varepsilon(\theta)$ is defined as

$$\varepsilon(\theta) = \varepsilon'(\theta) \frac{d\Omega(\theta)}{2\pi \sin\theta \, d\theta} \quad . \tag{4.2b}$$

Therefore $\varepsilon(\theta)$ accounts for the loss of particles which fall within the acceptance of the detector but are not detected as well as the loss of particles which fall outside the acceptance of the detector.

Most often the quantity being measured in an experiment is the differential cross section $d\sigma/d\Omega$ of the interaction. To show $d\sigma/d\Omega$ explicitly in equation 4.2 we insert equation 2.1,

$$N(\theta) = \int \varepsilon(\theta)\, N_T \frac{d\sigma}{d\Omega}(\theta)\; 2\pi \sin\theta \, d\theta \; F_B(t)\, dt \quad . \tag{4.3}$$

$F_B(t)$ is the beam flux and N_T is the number of target particles per unit area. The differential cross section is then given by,

$$\frac{d\sigma}{d\Omega}(\theta) = \frac{N(\theta)}{\int \varepsilon(\theta)\, N_T\, 2\pi \sin\theta\, d\theta\, F_B(t)\, dt} \quad . \qquad (4.4)$$

A measurement of $N(\theta)$ for an interaction and a calculation of the efficiency $\varepsilon(\theta)$ of the Saskatoon Alberta Large Acceptance Detector (SALAD) for the same interaction from a Monte Carlo analysis allows a determination of the differential cross section of the interaction.

The Monte Carlo calculation of the efficiency was tested by observing p(p,p)p elastic scattering at $E_p = 220$ MeV. The data was collected at TRIUMF on beam line 1B. The p-p events can be grouped into two categories - those events in which both outgoing protons are detected in coincidence and those events in which only one of the outgoing protons is detected. The coincidence efficiency $\varepsilon(\theta)$ as determined from a Monte Carlo analysis is combined with the observed number of coincidence events $N(\theta)$, to predict the shape of the p-p differential cross section. A comparison with the theoretical p-p differential cross section serves to test the calculation of the efficiency.

B) Procedure

For this efficiency study a beam of ~ 225 MeV protons of intensity on the order of $\sim 10^4$ / sec was required. The experimental set up is shown schematically in figure 4-1. A primary beam of 225 MeV and intensity 10^9 / sec (160 pA) was extracted from the cyclotron using an E-foil on stripper 1. The collimators C1, C2 and C3 are made from mild steel and are cylindrical of diameter 11.43 cm. Collimator C1 is 6.35 cm long while C2 and C3 are 7.62 cm long. The holes through their centers are 2.4 mm, 3.2 mm and 6.4 mm in diameter respectively. The proton flux through C1 was $\sim 10^7$ protons / sec. Downstream of C1 was placed a 0.8 mm thick steel sheet to diffuse the transmitted beam. The final bending magnet 1BB3 transported the collimated beam into the beam line 1B cave.

The beam exits the vacuum system through a thin mylar window. The second collimator C2 was placed next to the exit window. This collimator defined the beam

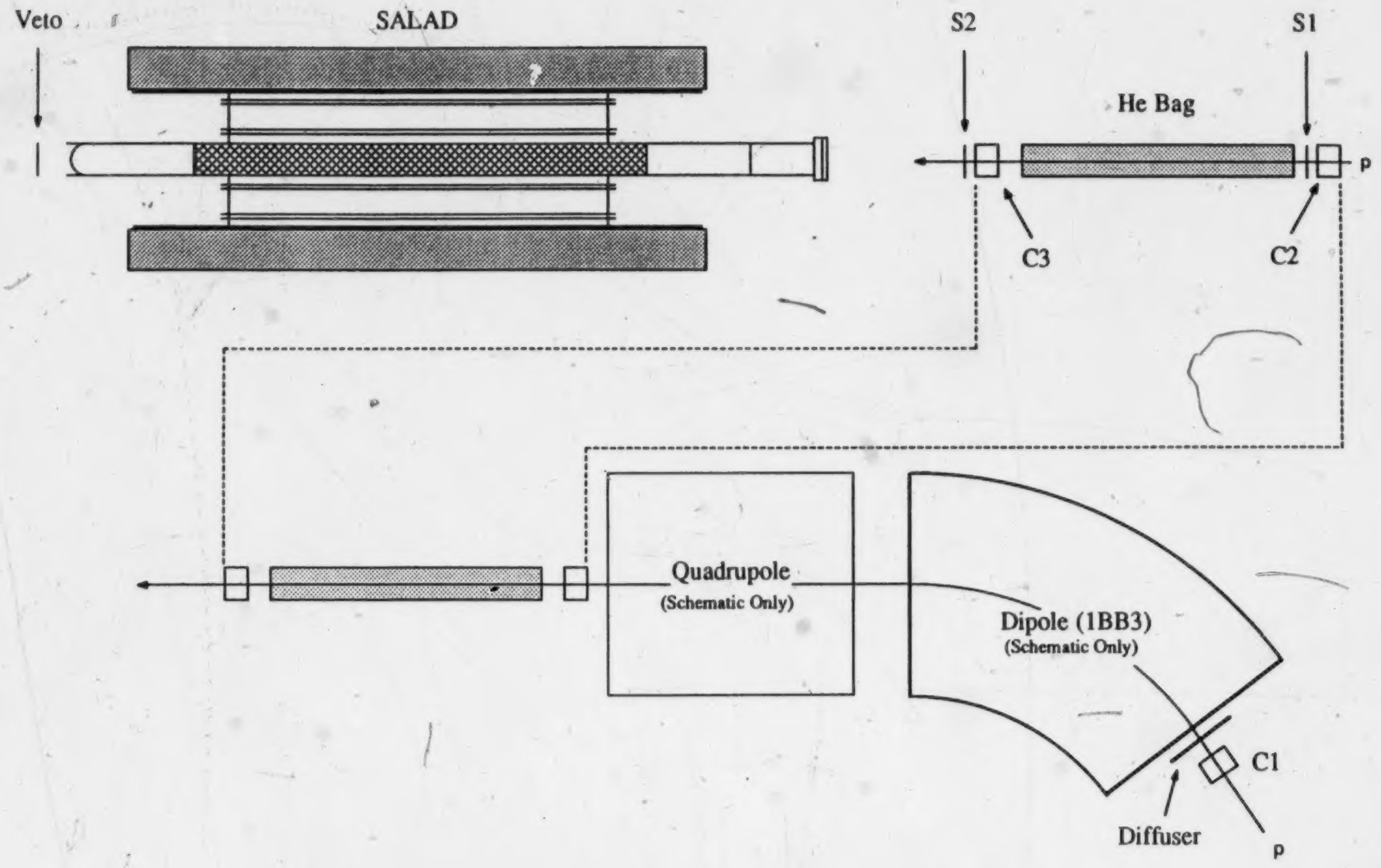

Figure 4-1 SALAD Efficiency Test on TRIUMF Beam Line 1B.
E_p = 220 MeV. Collimators and Event Trigger Scintillators Shown.

incident on the target. The beam emerging from C2 had an intensity on the order of ~ 10^4 protons / sec. A thin plastic scintillator S1 was placed between C2 and the 91.5 cm long helium bag. A clean-up collimator C3 was placed downstream of the helium bag followed by a thin plastic scintillator S2. The SALAD target window was 46.5 cm downstream of C3. LOSSPROG(13) calculations show that 5 MeV of proton kinetic energy is lost in the diffuser, S1 and S2. Thus the p-p interaction energy is 220 MeV.

The signature of a scattering event in the SALAD target cell is a signal from S1 and S2 in coincidence with no signal from a veto counter located downstream of the target ($S1\cdot S2\cdot\overline{veto}$). The number of protons incident on the SALAD target cell is given by S1, S2 and veto in coincidence ($S1\cdot S2\cdot veto$). For all but one run the SALAD trigger logic (see chapter 2) was set at one dE signal from both the upstream and downstream ends ($1dE_{up}\cdot 1dE_{dn}$). One run was completed by using the very strict coincidence trigger ($2E_{up}\cdot 2E_{dn}\cdot 2dE_{up}\cdot 2dE_{dn}$). The master event trigger was thus the coincidence ($S1\cdot S2\cdot\overline{veto}$)$\cdot$(SALAD).

After transport to TRIUMF, it was found that wire chamber 3 would not hold high voltage. Time constraints did not allow on site repairs and the efficiency test was made without the use of wire chamber 3. The E and dE scintillator high voltages were adjusted using an on line analysis package. The shape of the scintillator spectra was used as the criteria for adjusting the voltages. The dE scintillator thresholds were set roughly at 2 MeV and the E scintillator thresholds were set roughly at 17 MeV.

C) Wire Chamber Calibration

An event is recorded by a wire in a wire chamber when an energetic charged reaction product ionizes some of the wire chamber gas mixture. The free electrons cause more ionization as they accelerate toward the anode wire. This avalanche of electrons deposits a total amount of charge Q on the anode wire. SALAD employs the Self Quenching Streamer (or SQS) mode of wire chamber operation which is discussed in detail in appendix A. If the same amount of charge Q is deposited on the anode wire for every event then the ADC value recorded by one end of the wire, which is a measure of the fraction of Q reaching the end of the wire, is linearly related to the position on the wire where Q was collected. The usual method of position determination, and the method used here, employs a charge division readout. This method does not require Q to be the same for each event, although in SQS mode, Q is very nearly independent of the primary ionization. The method of charge division readout is outlined in appendix B-I.

To find the effective half length (L), and offset (L_o), for each wire in each wire chamber, a computer controlled radioactive ^{55}Fe source is used (discussed in detail in chapter 2). The collimated source irradiates the wires in three known z positions, z = 0, and z = ± 443 mm. The ADC values of the upstream and downstream ends are recorded for each source position and three $\mathbb{R}$ values are calculated as outlined in appendix B-I. A linear fit to the three ($\mathbb{R}$,z) pairs of data give values of L and L_o for every wire. Typical values of the effective half length, L, are 750 mm. The offset, L_o, equals zero on average but typically varies between -10 mm and 10 mm. The total charge collected as a function of the position of the source is illustrated in figure 4-2. The error bars are statistical. The spectra show that QSUM (the sum of the upstream and downstream ADC values) is independent of position as it should be.

To illustrate the ability of the SALAD wire chambers to reconstruct z positions, the values of L and L_o found from the source data are applied to the source data. The calculated source positions are shown in figure 4-3. Again the error bars are statistical. In these spectra one channel corresponds to 0.5 mm. At the center of the wire the resolution is ~ 3 mm FWHM ($\sigma_z \sim 1.3$ mm) while ± 44 cm from the center of the wire the resolution is ~ 6 mm FWHM ($\sigma_z \sim 2.6$ mm).

D) Track Reconstruction

The wire chamber analysis routine systematically searches for wires that display a *hit*. An anode wire is said to display a hit if it has a non-zero QSUM value. A track is said to have been found if (a) there is at least one hit found in the outer two wire chambers (3 and 4) and at least one hit found in the inner two wire chambers (1 and 2), and (b) a straight line can be drawn in the x-y plane which intersects the target cell and the wire cells whose wires show a hit.

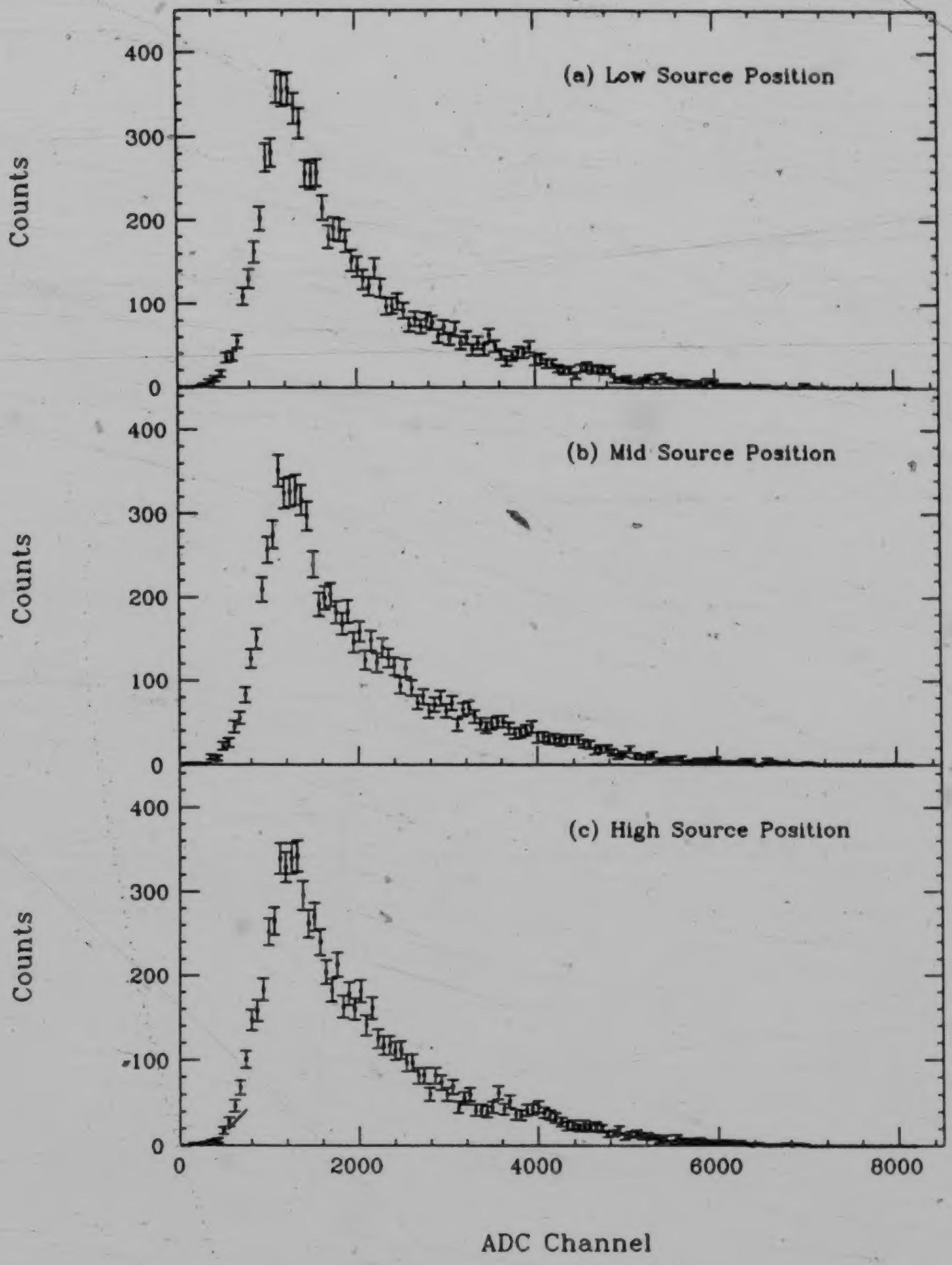

Figure 4-2 Typical QSUM Spectra of a Single Wire for the Three Source Positions.

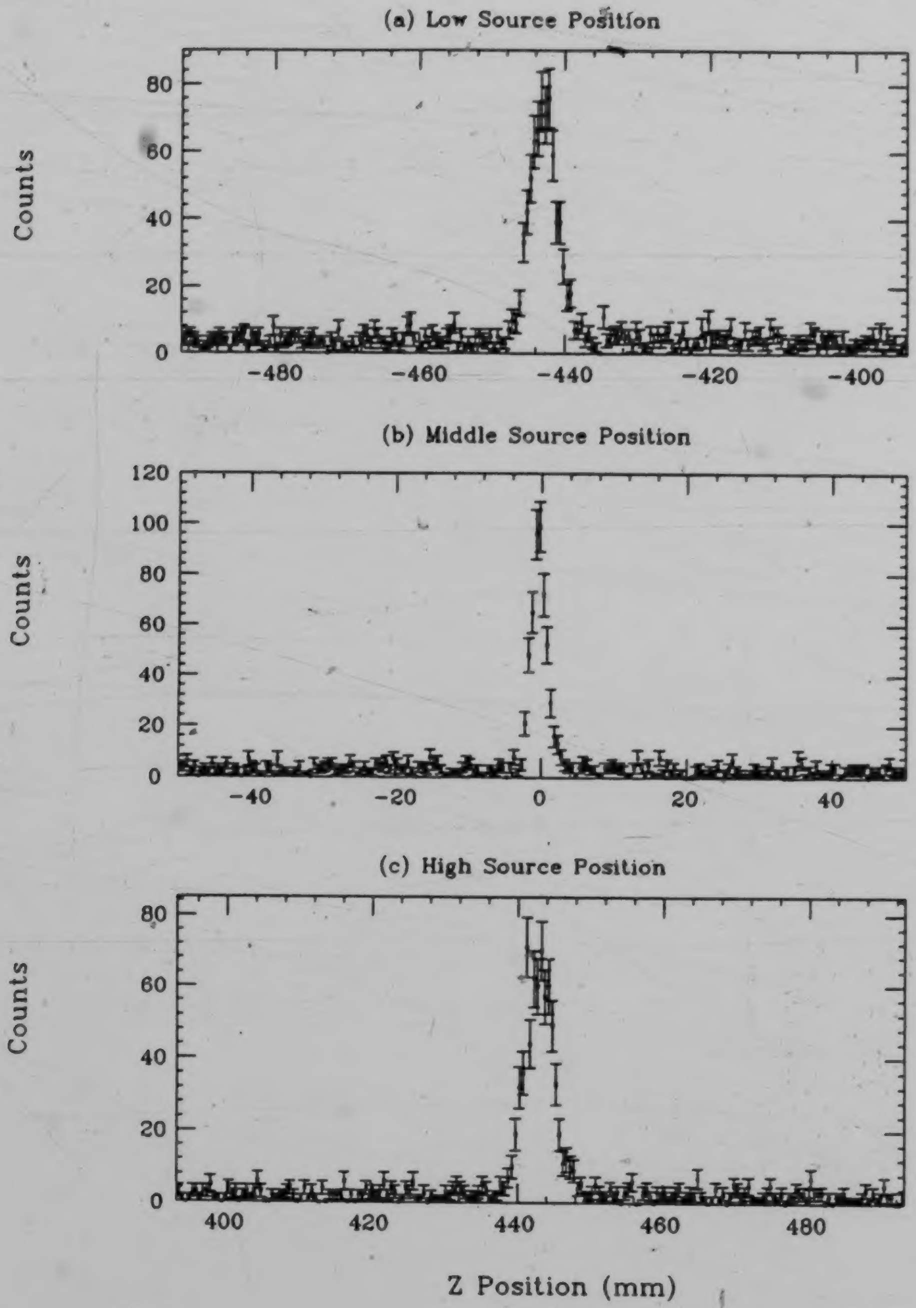

Figure 4-3 Calculated Source Positions for the Wire of Figure 4-2.

The search for hits starts at wire #1 in the outer chambers. If a hit is not found in either outer chamber a track cannot be reconstructed and the event is discarded. If a hit is found on a wire in chamber 4 (3) a search is made for a hit on all the wires in chamber 3 (4) such that the straight line condition is satisfied. For example, if the first hit (this will be referred to as the *primary* hit) is found on wire i in wire chamber 4 (3), wires i, i + 1, i - 1 and i + 2 in wire chamber 3 (4) are studied for a second hit. If a second hit is not found the tracking routine goes on to search the inner wire chambers. If a second hit is found, the difference in the z positions of the hits is calculated. From geometry it is known that if the difference in z positions is greater than ~ 14 cm, the hits cannot lie on a ray intercepting both the target cell and a dE scintillator (in the case that both outgoing protons must be observed the maximum z-difference is ~ 10 cm). If the z–difference is greater than 20 cm, the second hit is rejected and the search continues for a new second hit.

The search for hits in the inner wire chambers begins at wire number $j = i / 2$, where i is the wire number of this primary hit. The search spans the wires $j - 4 \leq k \leq j + 4$ of both inner chambers. If a hit is not found on these wires a track involving the primary hit cannot be reconstructed and the tracking routine returns to the outer chambers in search of a new primary hit. If a hit is found on wire k in wire chamber 2 then wires k, k + 1, k - 1 and k + 2 in wire chamber 1 are studied for a hit. If a hit is found on wire k in wire chamber 1 then wires k, k + 1, k - 1, k + 2 and k - 2 in wire chamber 2 are studied for a hit. If hits are found in both inner chambers a z-difference check is made. If this check is failed the last hit found is rejected and the search continues for another hit.

When a pattern of hits is found which suggests a track originating from the target, a linear fit is calculated for the hits involved. The tracking routine then returns to the outer chambers in search of a new track involving a new primary hit. An event has been analyzed when the outer chambers have been searched entirely for primary hits and all possible tracks have been found.

The (x,y) position of a hit is estimated to be (x_w,y_w) where x_w and y_w are the physical positions of the wire showing the hit. The z position of a hit is calculated from charge division readout. The track analysis routine uses the values of (x_w ,y_w ,z) of each hit to determine for each track the direction of the scattered proton through the detector, $\left(\frac{dx}{dz}, \frac{dy}{dz}, \frac{dz}{dz}\right)$, and the point where the particle crosses the $z = 0$ plane, $(x_o, y_o, z = 0)$. Also calculated for each track are the cylindrical coordinate angles θ and ϕ. Since the direction of the incident protons is not measured, θ is calculated relative to the coordinate axes of the detector as shown in figure 2-2. For a beam incident along the detector axis, θ is approximately equal to the scattering angle of the p-p interaction.

For tracks involving more than two hits, a tracking error estimate is made using the expression

$$\chi^2_{track} = \frac{1}{N-2} \sum_{i=1}^{N} \left(x_i - x_w\right)^2 + \left(y_i - y_w\right)^2 , \qquad (4.5)$$

where N is the number of wires utilized in reconstructing the track, x_i and y_i are calculated using

$$x = x_o + \frac{dx}{dz} z \quad , \qquad (4.6a)$$

and

$$y = y_o + \frac{dy}{dz} z \quad , \qquad (4.6b)$$

where z is found from charge division readout.

An example of a typical track reconstruction is shown in figure 4-4 for a p-p event. The components of SALAD are shown schematically only. Figure 4-4 (a) shows the event in the x - y plane. The wire chamber cells and scintillators which display a hit are indicated with an X. Figure 4-4 (b) shows the same event in the r - z plane. The calculated z positions of the hits on the wires are indicated with an X. The interaction vertex and reconstructed tracks 1 and 2 are shown.

E) The Reduced Data Set

The raw data set contains a very large amount of background. A reduced data set is made by analyzing the raw data and imposing the condition that at least one track be found in an event. Implicit in this cut are the geometrical restrictions of the track

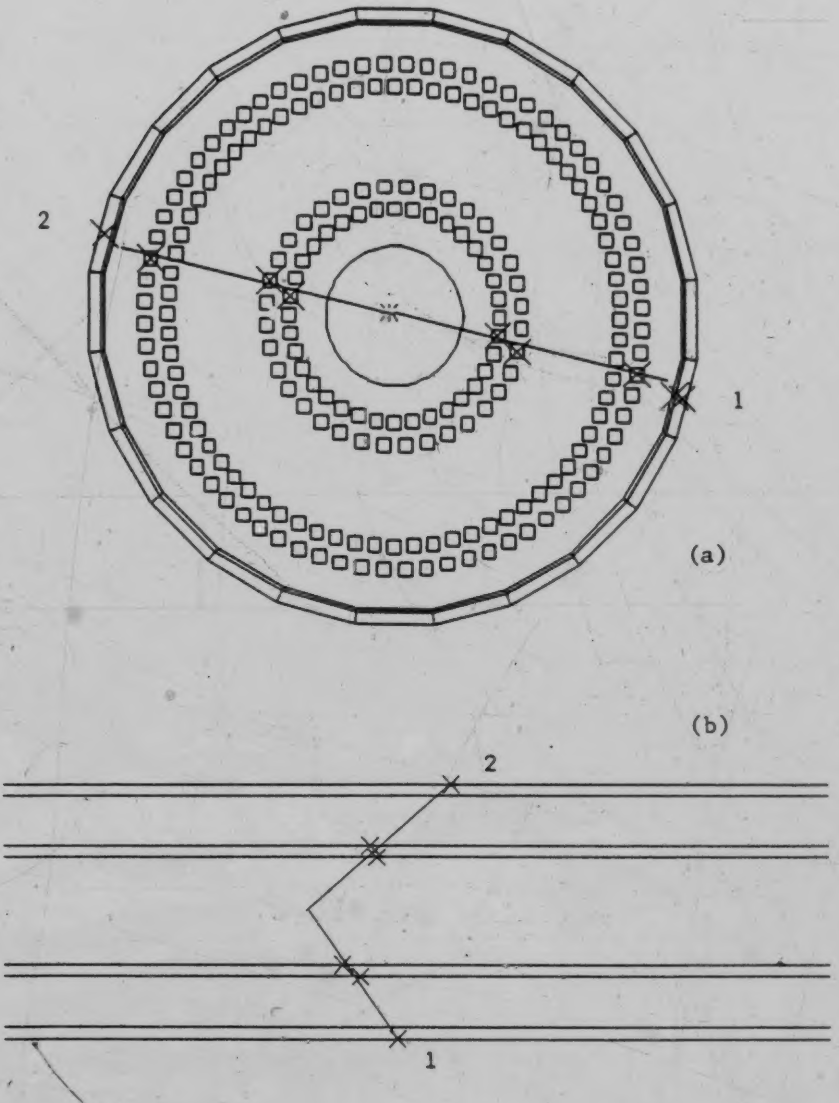

Figure 4-4 Reconstructed Tracks for a Typical p-p Scattering Event.

reconstruction routine. No kinematic or energy analysis restrictions are applied at this stage of data reduction. This condition reduces the data set by 90% without rejecting any p-p events.

To isolate coincidence events, the data set is reduced further by rejecting those events in which only one track is found. Again no kinematic or energy loss restrictions are applied to this cut. This condition further reduces the data set by 95%. Although only 0.5% of the raw data set remains, no p-p coincidence events have been rejected.

In the center of momentum frame the protons move away from each other in a straight line. In the laboratory frame the protons lie in a plane and are separated by an angle that depends on the energy of the incident beam. For a beam energy of 220 MeV this opening angle varies between 87° and 90°. If one proton is scattered at an angle of 43.5° with respect to the direction of the incident proton, the other proton also scatters at 43.5°. The opening angle in this case is 87°. As the scattering angle of one proton increases from 43.5° the scattering angle of the other proton decreases from 43.5° such that the opening angle increases from 87° to 90°. In the extreme case, one proton scatters at 90° and the other at 0° resulting in an opening angle of 90°. The geometrical and energy loss properties of SALAD discussed in section G place restrictions on the event trigger such that the opening angle of the p-p coincidence events is ~ 87°.

Not only are the events coplanar and have a small range of opening angle but, the outgoing protons must originate from a single point within the target cell. However, due to the finite resolution of the wire chambers the two outgoing protons rarely appear to originate from a point. Instead the minimum distance between the outgoing tracks is calculated as shown in figure 4-5. This is done by finding the point A on track 1 nearest track 2 and then finding the point B on track 2 nearest track 1. The vertex of the event is defined as the midpoint of the line AB. Thus each two track event can be required to satisfy both a minimum distance cut, as well as the kinematic cuts of coplanarity and opening angle.

Two other parameters are monitored to which cuts can be applied. One parameter is the radial distance of the interaction vertex from the z - axis. A 'Good Target' restriction is made by requiring that the vertex lie within the gas target volume. The z - coordinate of the vertex, z_{vtx}, must lie between a *Z-LOW* and *Z–HIGH* value and the radial distance of the vertex, R_{vtx}, be less than a *RADIUS–CUT* value. The other parameter is the root mean square, or RMS, error in the track reconstruction which is given by the square root of equation 4.3. A 'Good-Tracks' restriction is made by ensuring that the RMS value of both outgoing tracks be less than some *RMS-CUT* value.

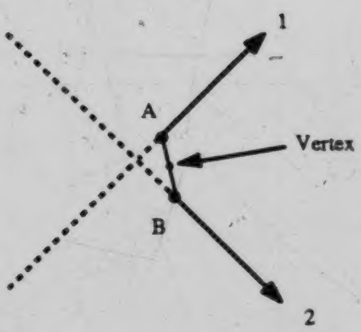

Figure 4-5 Minimum Distance and Interaction Vertex Definitions.

The reduced data set is produced by applying the following coplanarity, opening angle, minimum distance, good-target and good-tracks cuts to those events which show two tracks. The opening angle is calculated simply from $\theta_1 + \theta_2$ and those events which satisfy

$$\theta_1 + \theta_2 - 87^\circ < \delta_{(\theta_1 + \theta_2)} = 60^\circ \qquad (4.7)$$

are accepted. If a scattering event is coplanar then $\phi_1 - \phi_2 = 180^\circ$. Those events which satisfy

$$|\phi_1 - \phi_2| - 180^\circ < \delta_{|\phi_1 - \phi_2|} = 100^\circ \qquad (4.8)$$

are accepted. Those events which satisfy the minimum distance cut

$$|\text{Distance}| < \delta_{\text{Distance}} = 80 \text{ mm} \quad . \qquad (4.9)$$

are accepted. The Good-Target parameters are set at

$$-120.0 \text{ cm} \leq z_{vtx} \leq 120.0 \text{ cm} \ , \qquad (4.10a)$$

$$R_{vtx} < 55 \text{ mm} \ , \qquad (4.10b)$$

and the Good-Tracks parameter was set at

$$\text{RMS-CUT} < 70 \text{ mm} . \qquad (4.11)$$

These cuts are deliberately set very wide to give as much freedom as possible in the choice of the final tight cuts to be made later.

The above cuts reduce the data set by another ~ 50%. Nearly all of the rejected events fail the RADIUS - CUT since a large number of events involve the wall of the target cell. This can be seen in figure 4-6 where the x - y position of the interaction vertex is shown for those events which satisfy the minimum distance and Good-Tracks cuts. Figure 4-6 (a) corresponds to the H_2 gas target cell and figure 4-6 (b) corresponds to a CH_2 disk of uniform areal thickness. The CH_2 target shows a very small fraction of the beam extends beyond a radius of ~ 3 cm. Although the number of beam protons is small in the region of the target cell wall, the areal thickness of the wall is high making an interaction likely.

The opening angle, coplanarity and minimum distance spectra of the reduced data set are shown in figures 4-7, 4-8 and 4-9 respectively. The error bars in each figure are statistical. All of the above cuts are applied to each spectrum except the cut of the parameter histogrammed. The discontinuous structure of the coplanarity and minimum distance spectra is a result of the discrete wire positions within the wire chambers. The opening angle and coplanarity spectra display a large background which comes primarily from the wall of the target cell (p - ^{12}C and p - ^{27}Al events) as shown in figures 4-6 (a) and 4-10. The radial position of the vertex is shown in figure 4-10. The events involving the target wall and the events involving the H_2 gas are clearly separated in this figure. The RMS error is shown in figure 4-11. The granularity of the wires in the wire chambers causes the discontinuous structure of this histogram.

The distribution of greatest interest is $N(\theta)$, the number of protons scattered into an angle θ. $N(\theta)$ is shown in figure 4-12 for the reduced data set. The events plotted in figure 4-12 pass all of the above cuts and are therefore consistent with p-p elastic scattering kinematics. The extended tail near 100° indicates that some background is still present in the reduced data set. The remaining background is removed using the final reduction cuts discussed next.

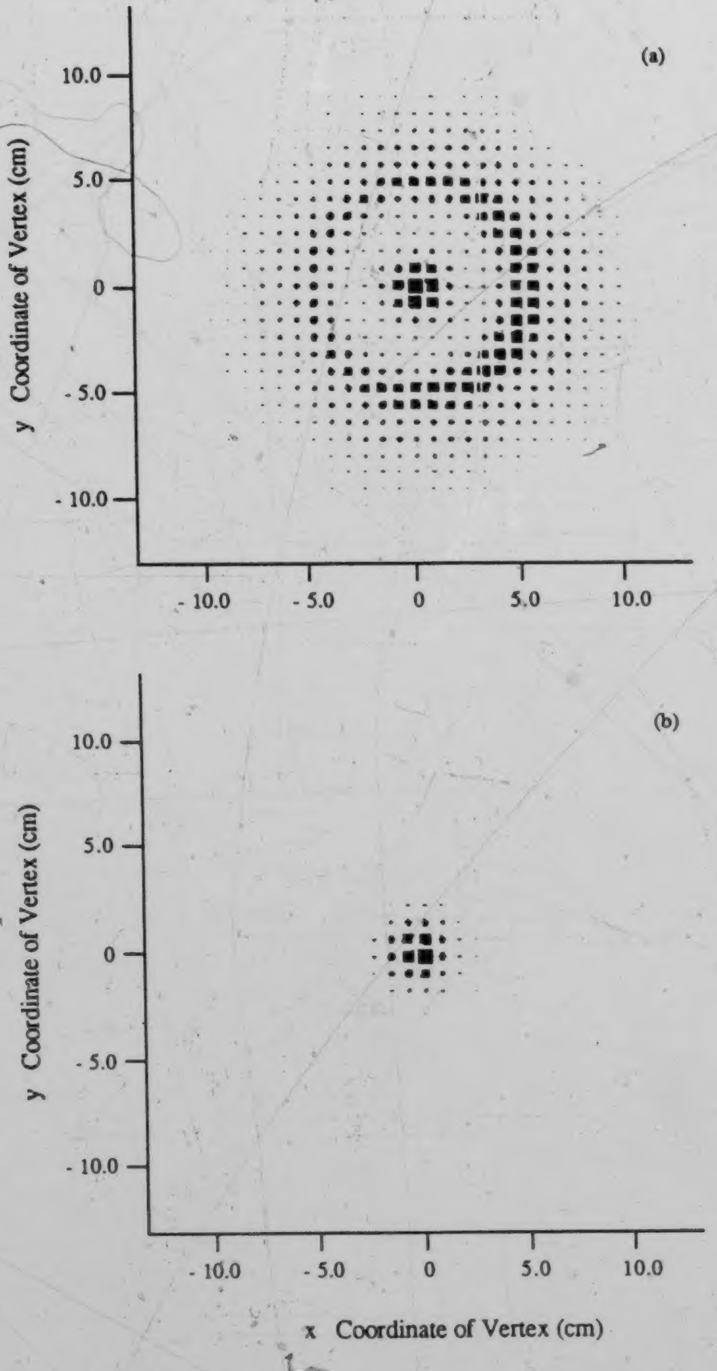

Figure 4-6 Interaction Vertex in the x-y Plane for (a) the H_2 Gas Target Cell and (b) a CH_2 Target of Uniform Areal Thickness.

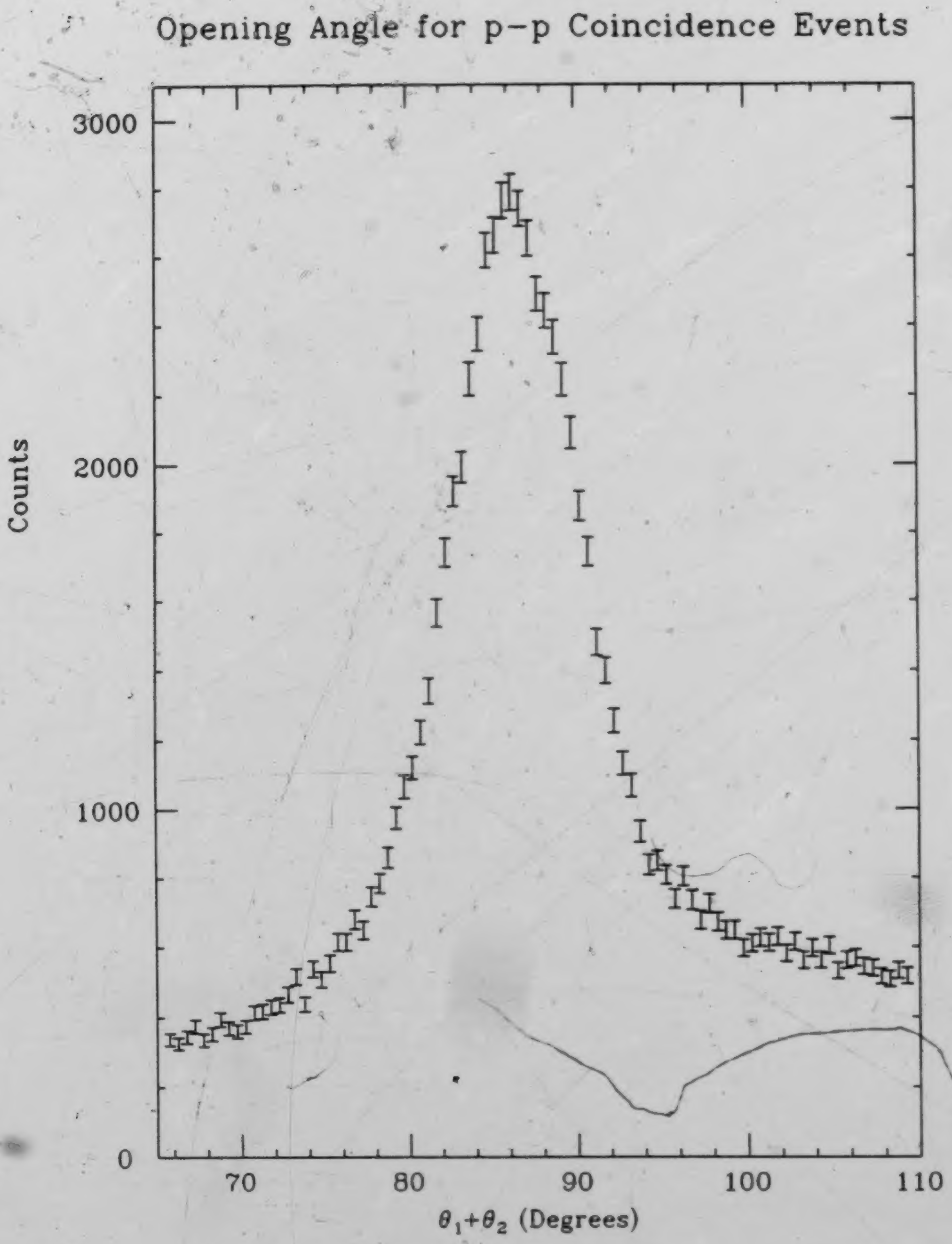

Figure 4-7 Opening Angle of the Reduced p-p Data Set.

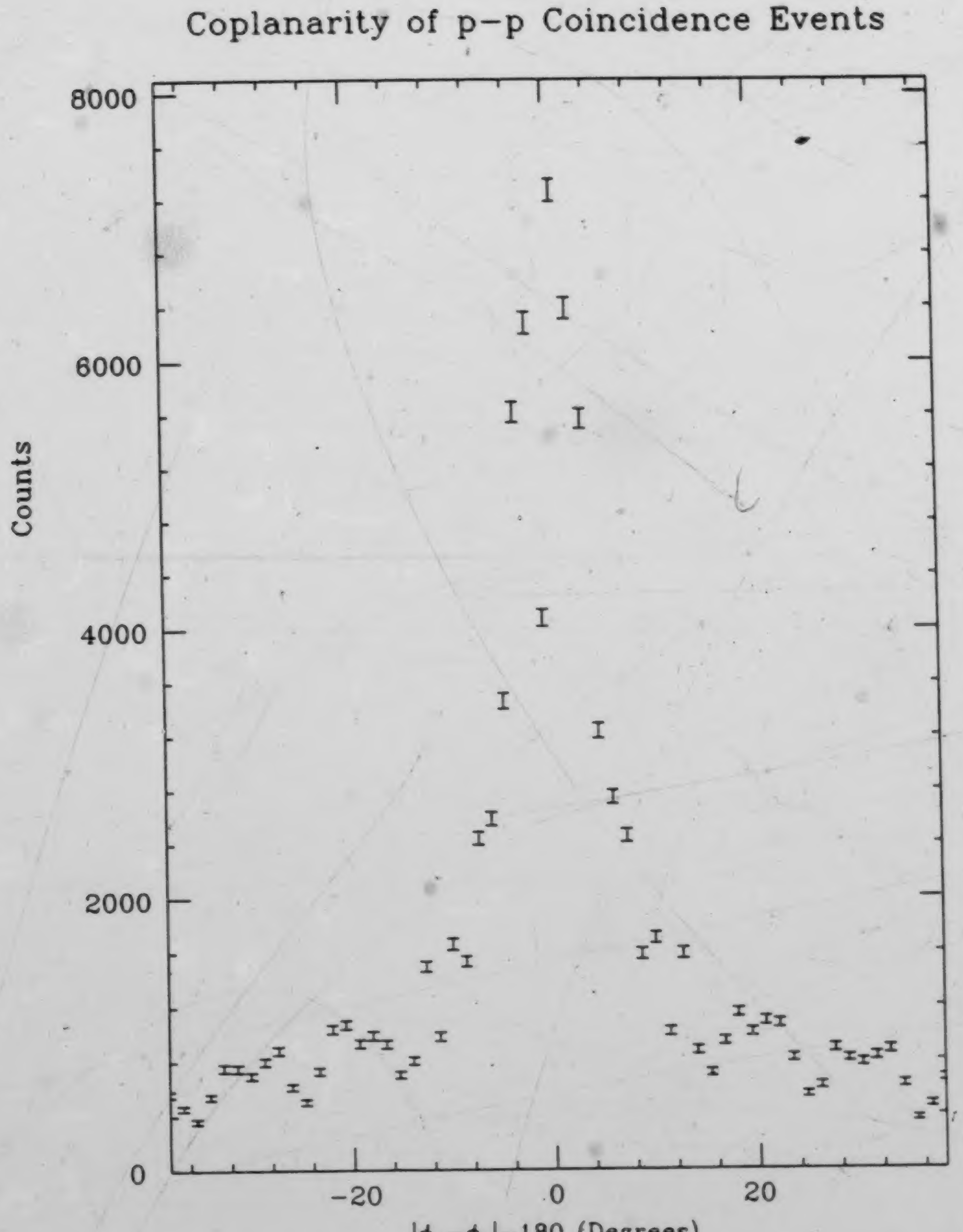

Figure 4-8 Coplanarity of the Reduced p-p Data Set.

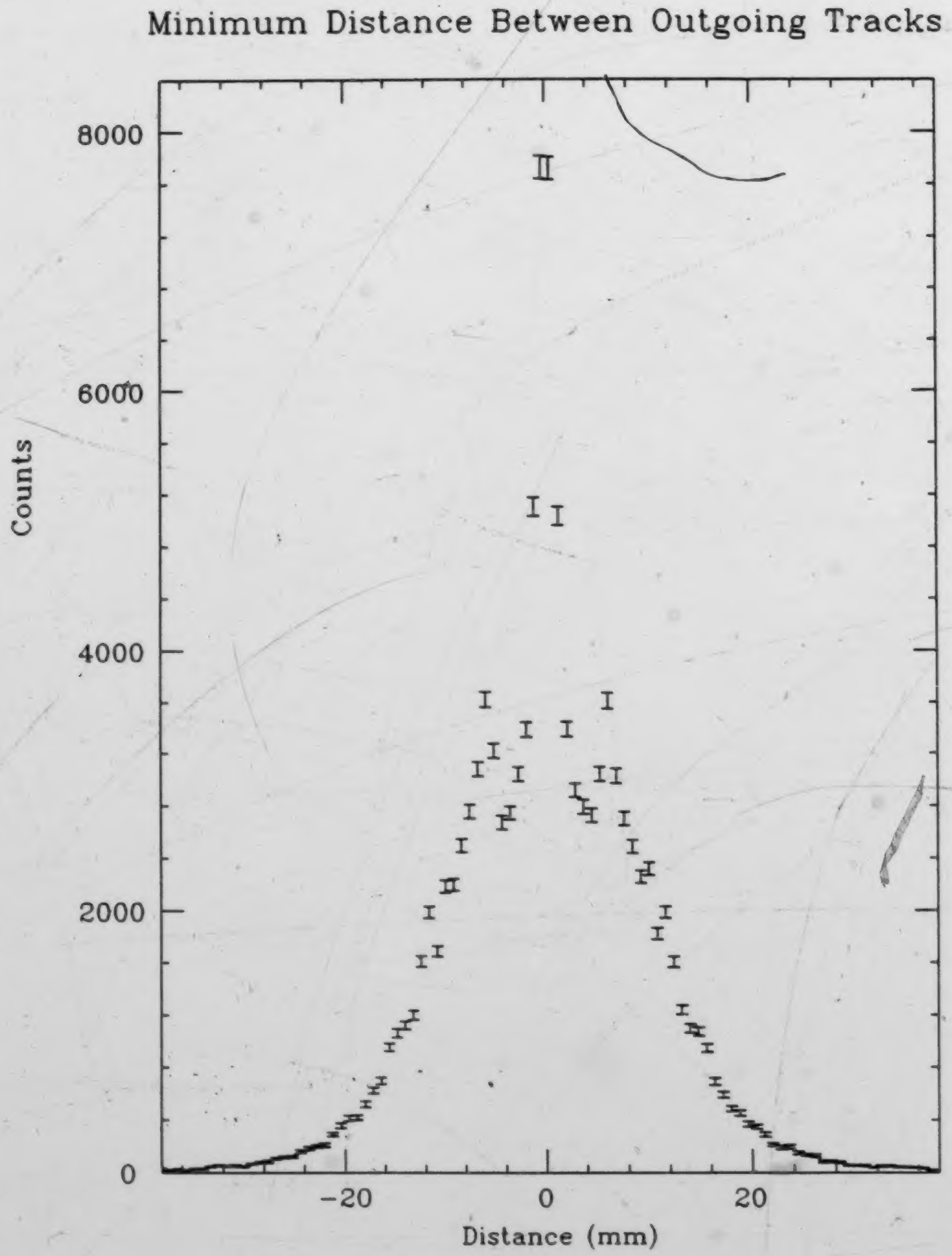

Figure 4-9 Minimum Distance Between Outgoing Protons for the Reduced p-p Data Set.

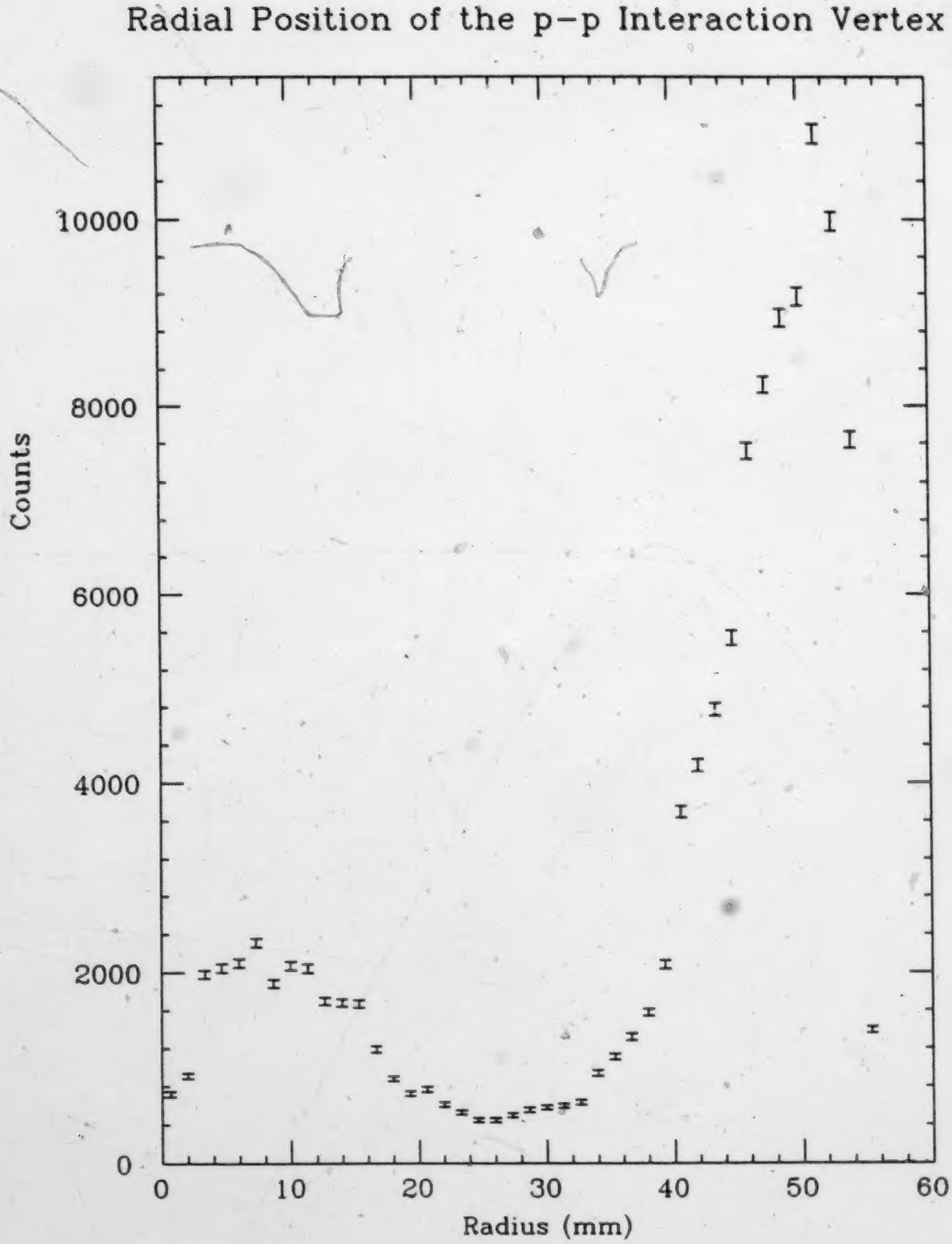

Figure 4-10 Radial Vertex Position for the Reduced p-p Data Set.

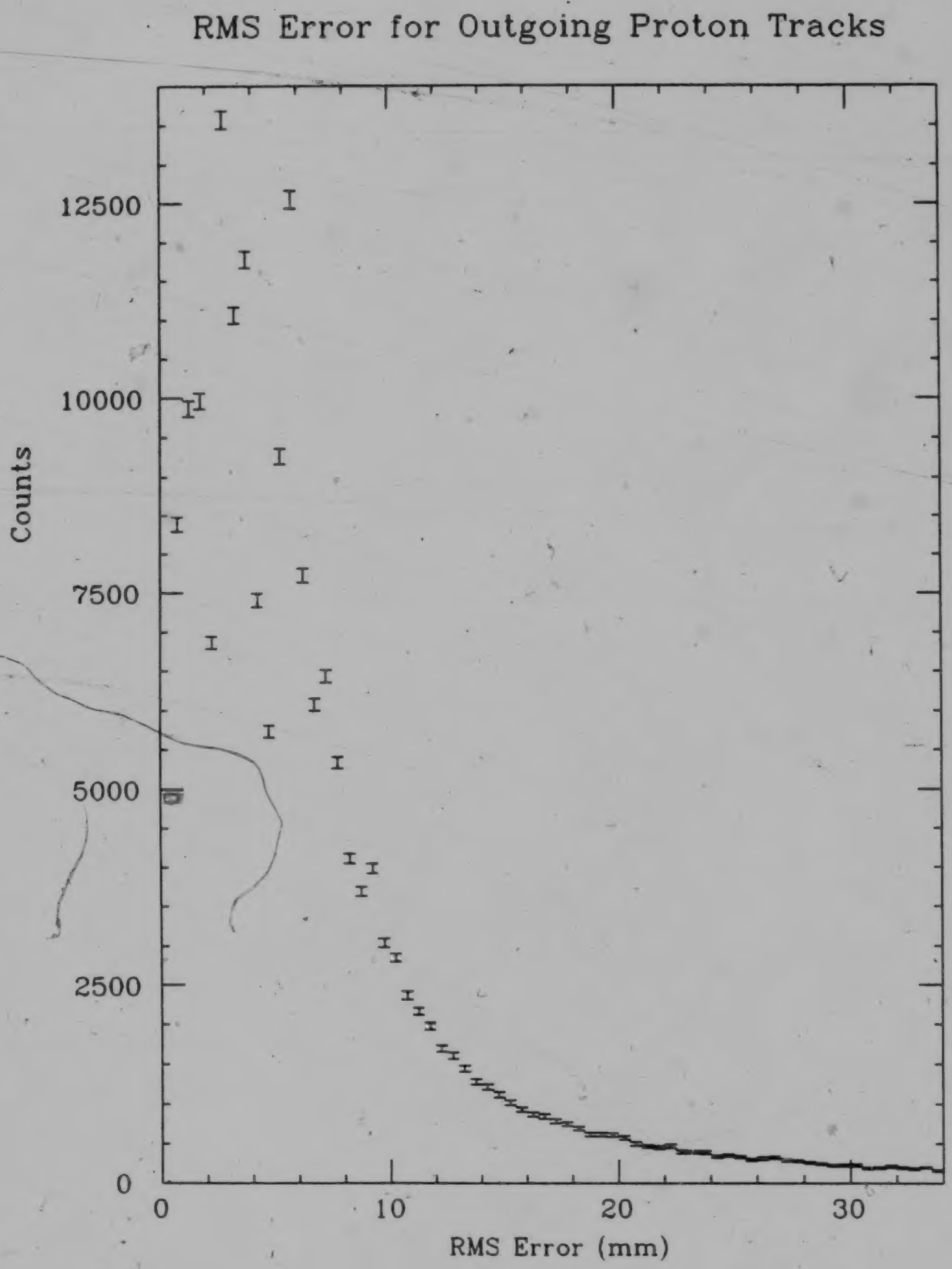

Figure 4-11 RMS Error of Reconstructed Tracks for the Reduced p-p Data Set.

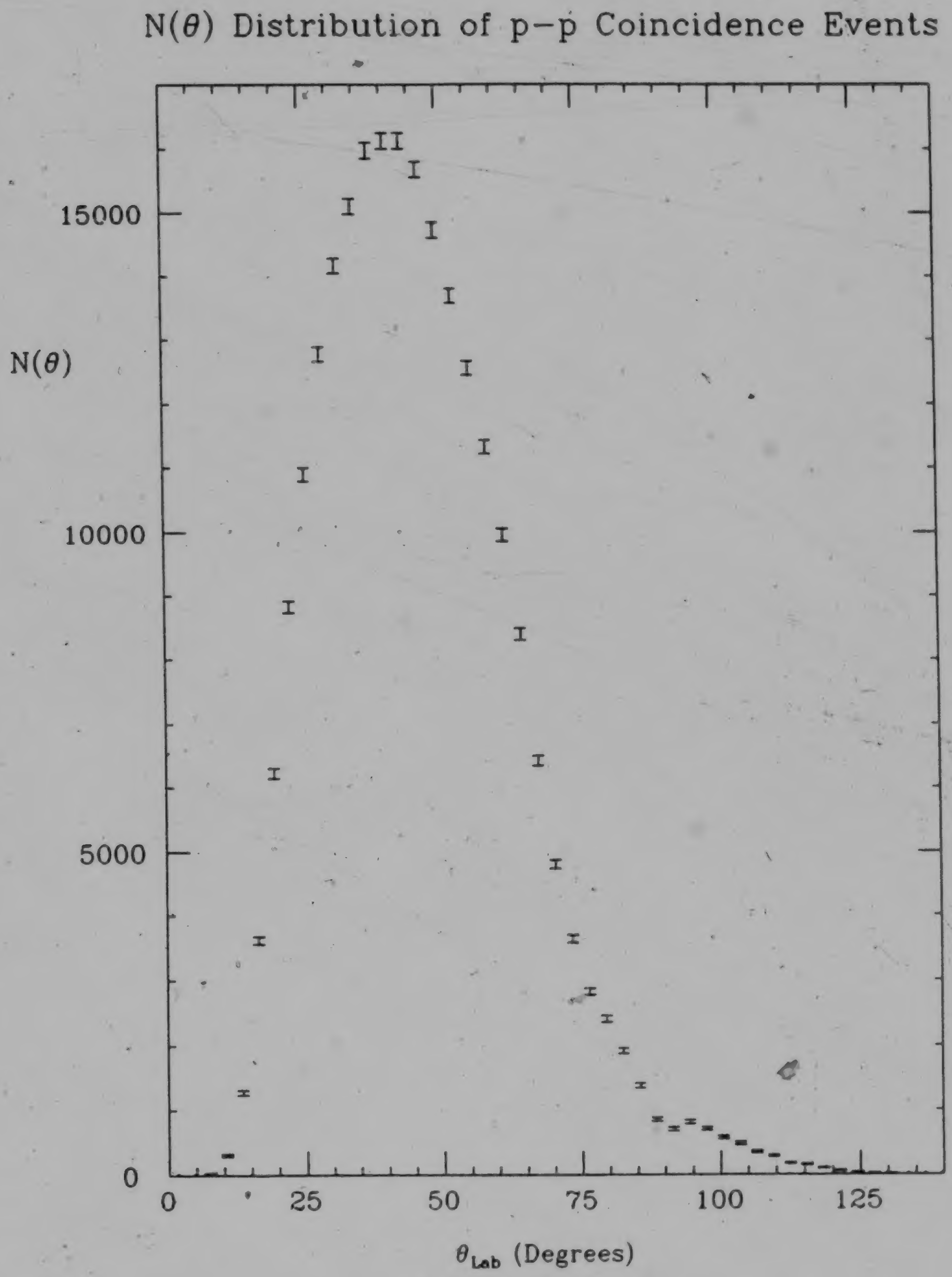

Figure 4-12 Anglular Distribution of Scattered Protons for the Reduced p-p Data Set.

F) The Final Data Set

Further cuts need to be applied to the reduced data set to remove the background from the N(θ) distribution shown in figure 4-12. The cuts must be strict enough to remove the background but not so strict as to remove true p-p coincidence events.

The obvious cut to make is to remove events from the target wall as displayed in figure 4-10. However, such a cut requires a guess as to where the distribution of counts from the H_2 gas ends. Before applying this cut, the effects on the radial vertex position and N(θ) plots by applying tight cuts to the opening angle, coplanarity and minimum distance spectra are explored.

One at a time, successively tighter cuts are made on each of these three spectra. The number of coincidence events, as given by the number of counts in the N(θ) distribution, is recorded for each cut. The fraction of counts remaining in the N(θ) spectrum after each cut is shown in figures 4-13 to 4-15. Each plot displays a linear section when the cuts are wide. This indicates that a flat background is present. The cut chosen is a point near the end of this linear region as shown in the figures.

The following observations were made after the application of these three cuts. The tail in the N(θ) distribution at high angles now extends to ~ 85°. The radial vertex position spectrum still has two peaks. The number of counts in the H_2 region is virtually unchanged but the number of counts in the target wall region is reduced by ~ 65%. The number of counts at the minimum between the two regions has gone from 400 to 200 counts per channel, and the minimum has shifted from ~ 25 to ~ 30 mm. With the separation between the two regions more sharply defined a cut on the radial vertex postion is made at 30 mm.

The addition of this vertex position cut reduces the number of counts in each spectrum by ~ 50%. The opening angle, coplanarity, minimum distance and radial vertex position spectra of the final data set are shown in figures 4-16 to 4-19 respectively. The cuts applied to each spectrum are shown in these figures. The N(θ) distribution of the final data set is shown in figure 4-20.

The effect of an RMS cut was tested by making an RMS cut of 15mm as well as the above kinematic minimum distance and radial vertex position cuts. The addition of this cut did not reduce the background in any spectrum. This cut did however reduce

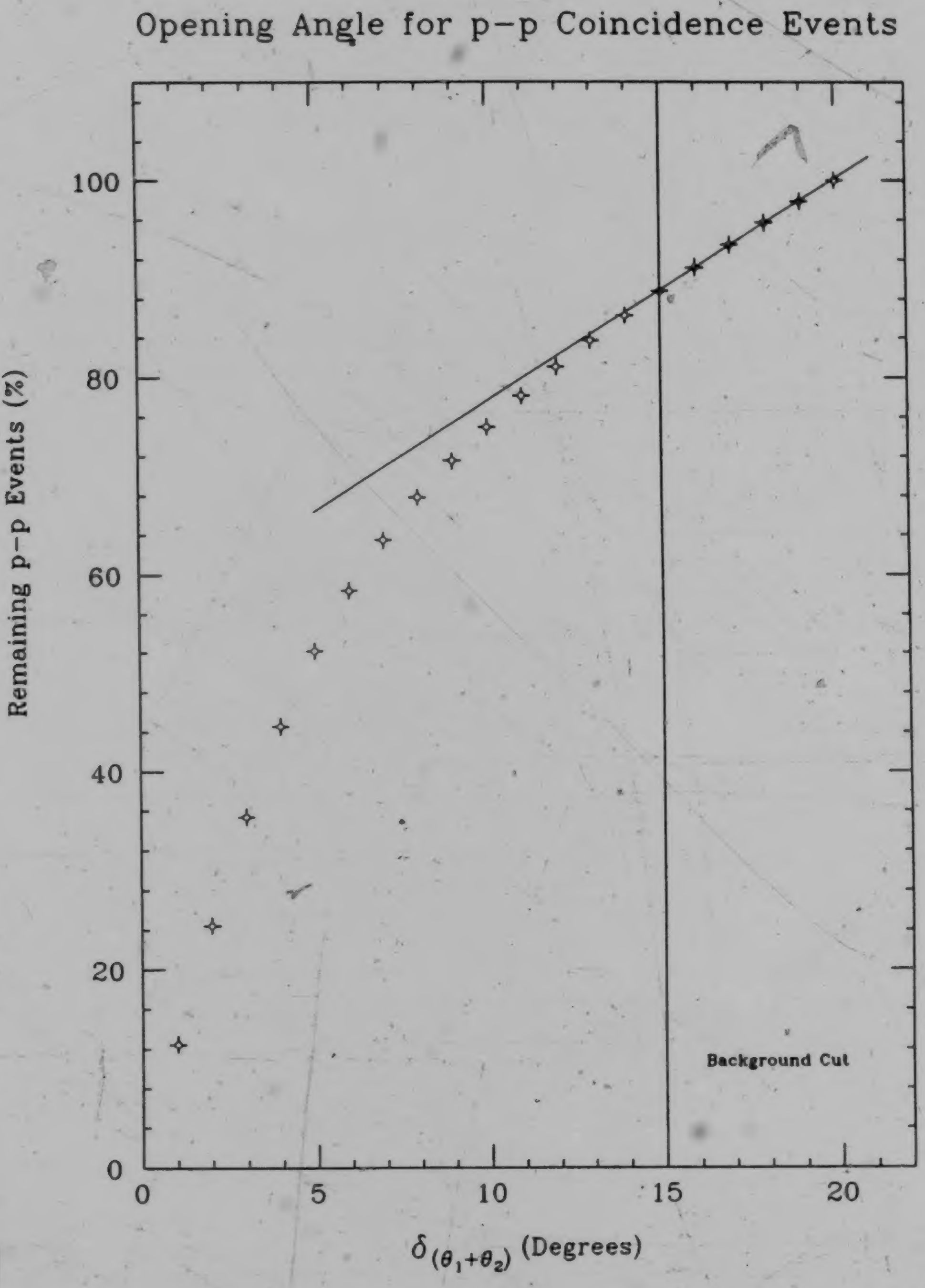

Figure 4-13 Fraction of p-p Events in the N(θ) Spectrum as a Function of Opening Angle Cut.

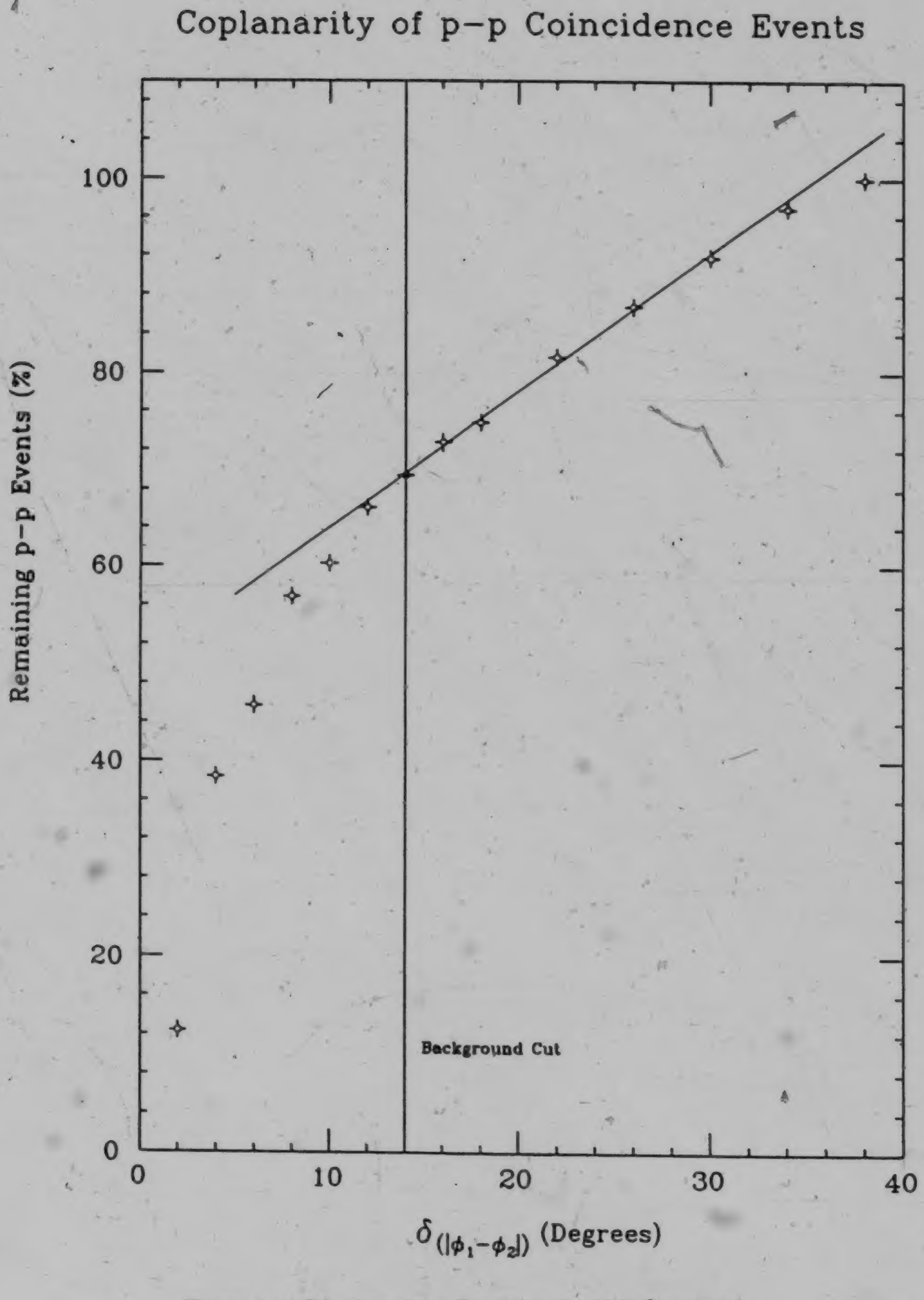

Figure 4-14 Fraction of p-p Events in the N(θ) Spectrum as a Function of Coplanarity Cut.

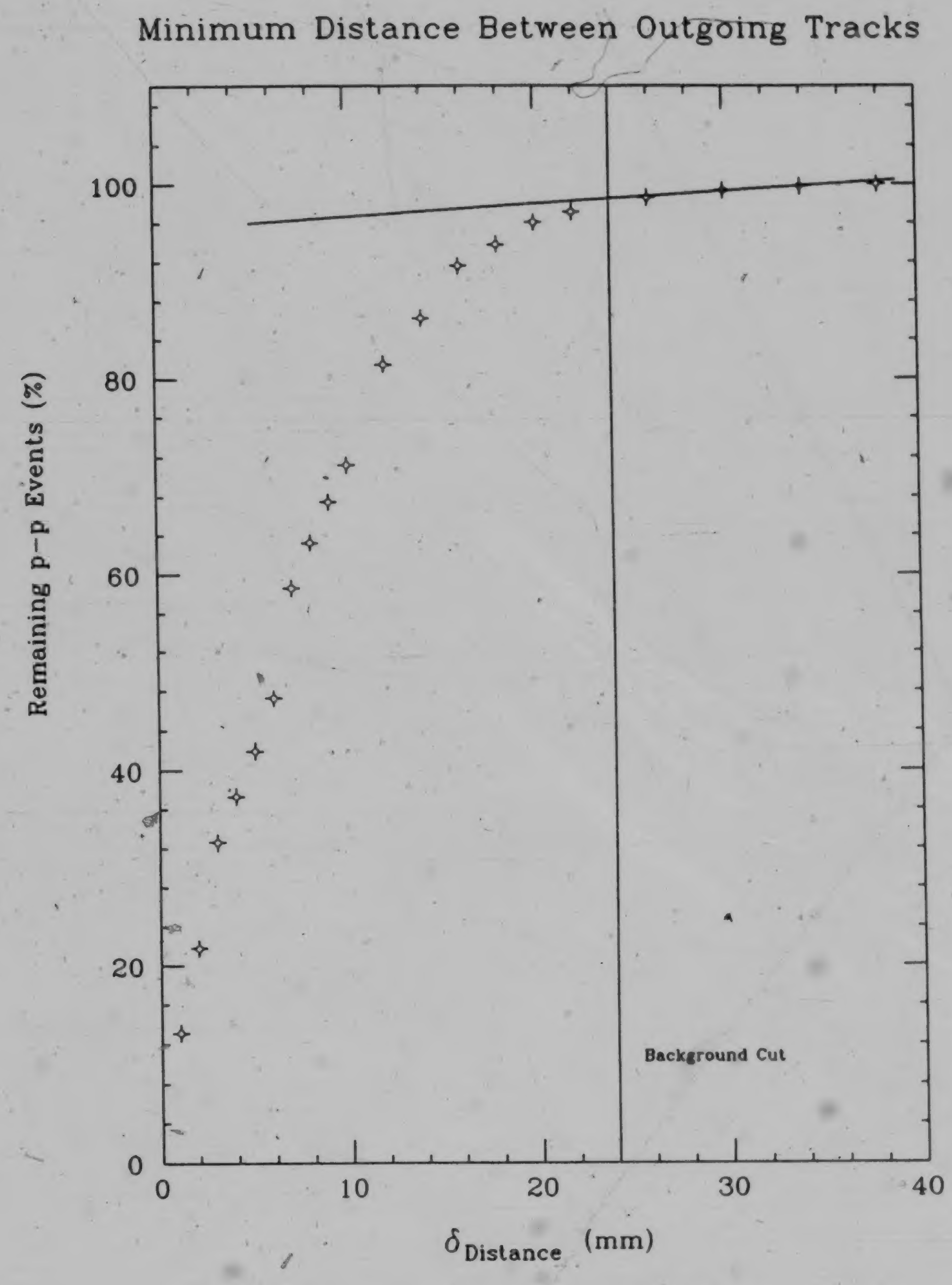

Figure 4-15 Fraction of p-p Events in the N(θ) Spectrum as a Function of Minimum Distance Cut.

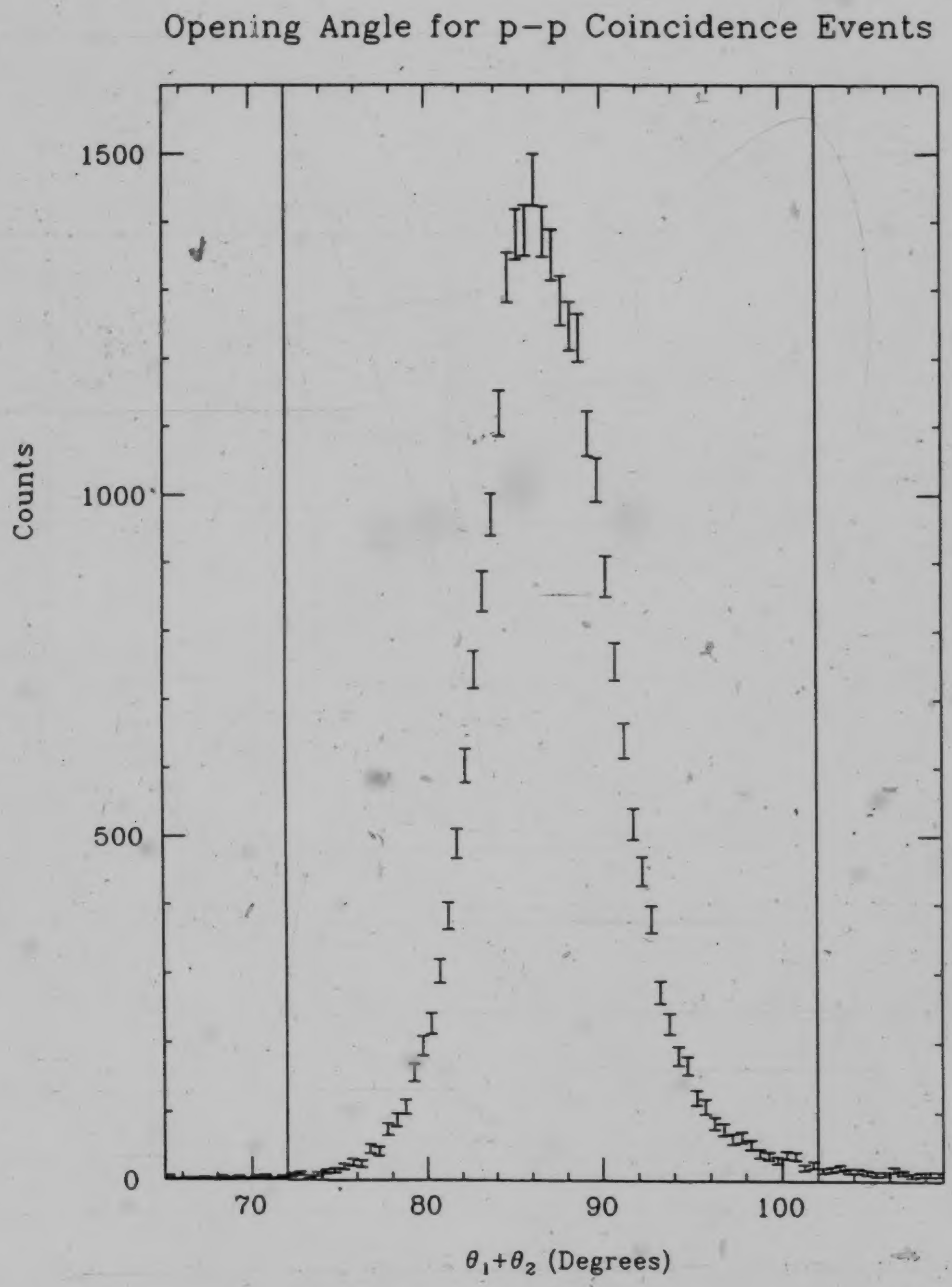

Figure 4.16 Opening Angle of the Final p-p Data Set.

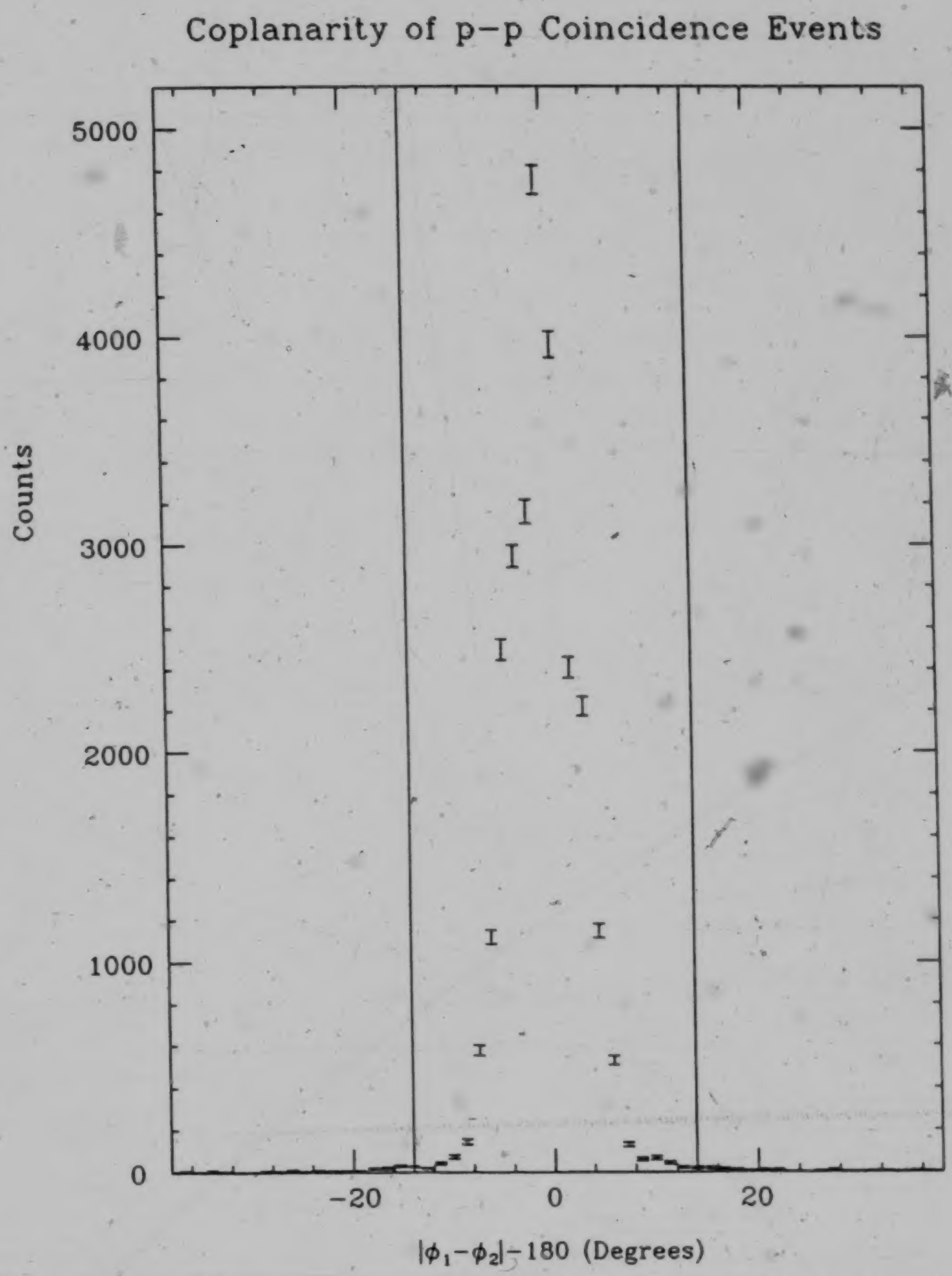

Figure 4-17 Coplanarity of the Final p-p Data Set.

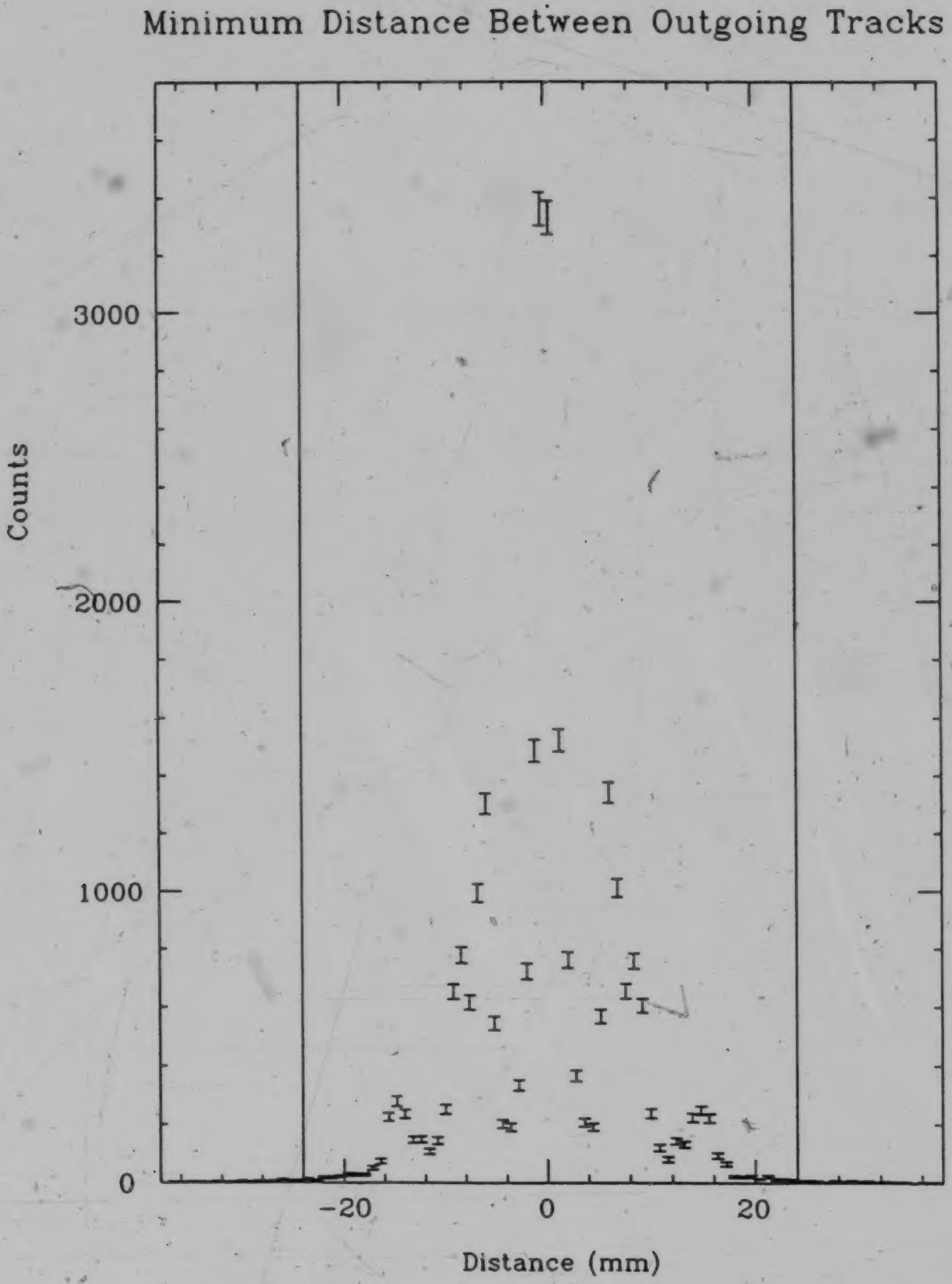

Figure 4-18 Minimum Distance Between Outgoing Protons for the Final p-p Data Set.

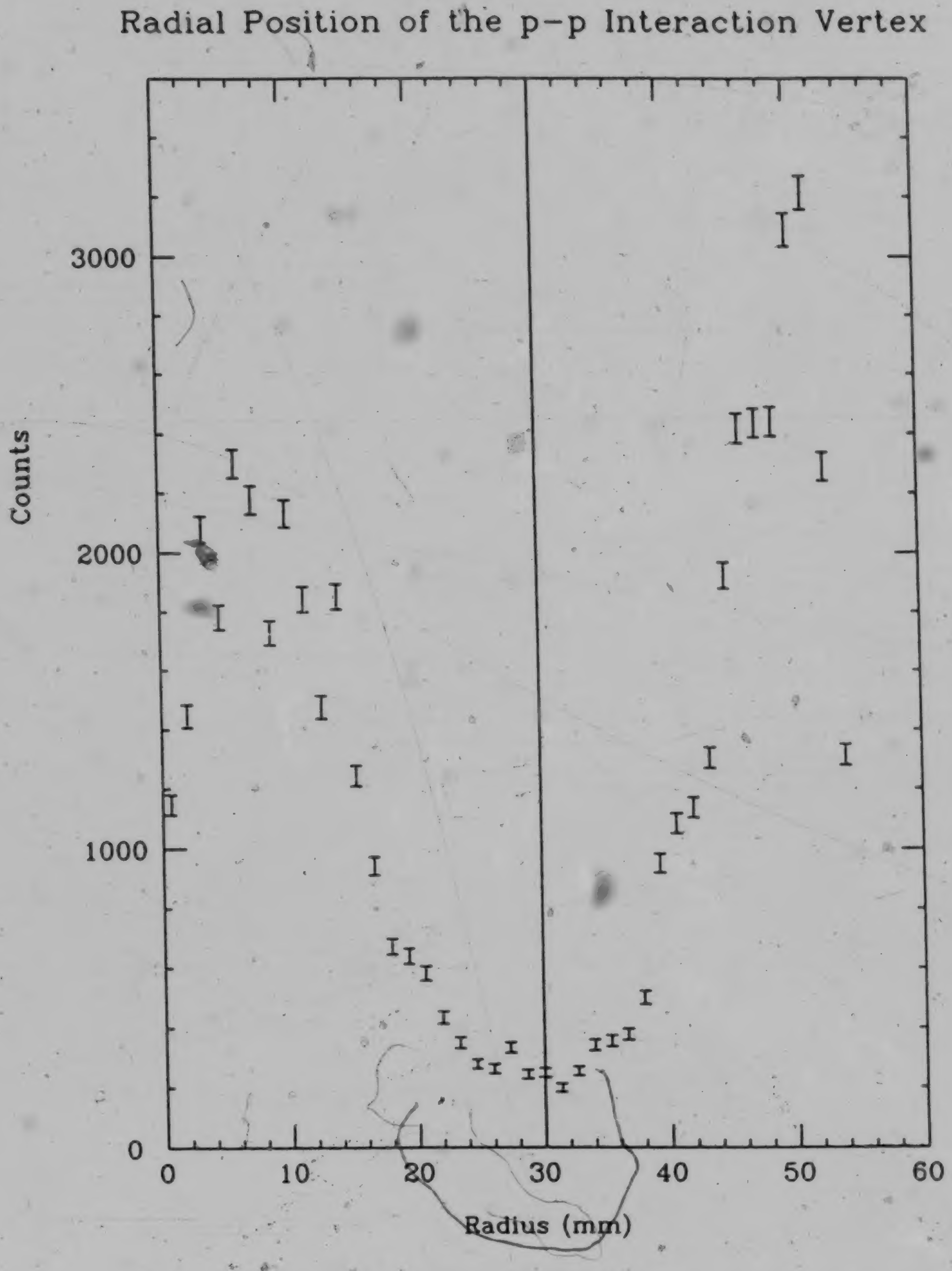

Figure 4-19 Radial Vertex Position for the Final p-p Data Set.

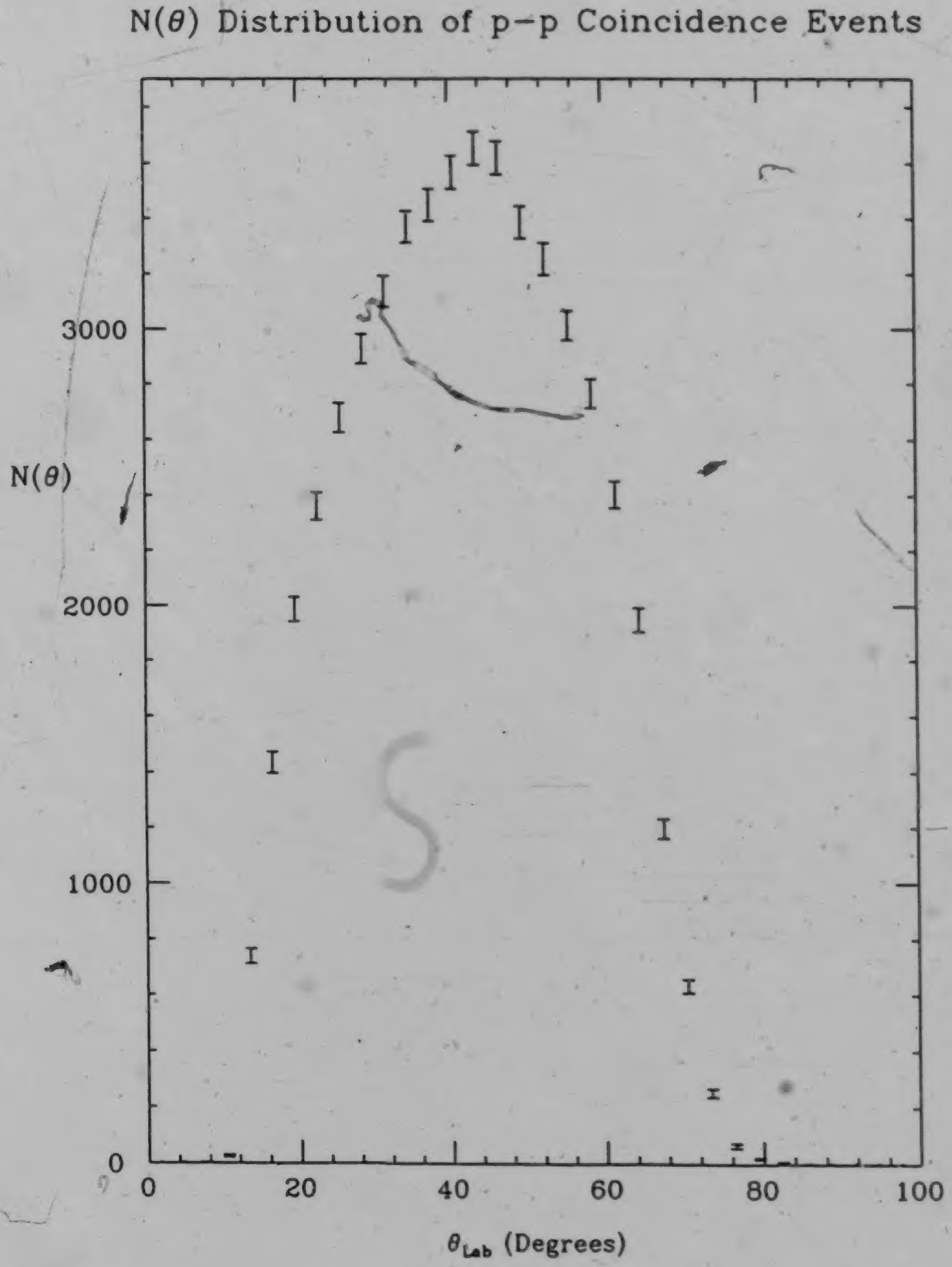

Figure 4-20 Anglular Distribution of Scattered Protons for the Final p-p Data Set.

the number of counts in the H_2 region of the radial vertex position spectra by 5%. Since this cut does not improve the good p-p to background ratio, it is left at the value of 70 mm.

In order to estimate the number of bad p-p events included in the final data set, those events which pass all except the coplanarity cut were studied. This was done simply by reversing the coplanarity restriction and rejecting those events for which

$$|\phi_1 - \phi_2| - 180^\circ < \delta_{|\phi_1 - \phi_2|} = 14^\circ \qquad (4.12)$$

The two resulting histograms of interest are shown in figures 4-21 (a) and (b). Figure 4-21 (a) is an opening angle spectrum of the non-coplanar events. It is believed that the background beneath the opening angle spectrum of figure 4-16 has a similar angular distribution. To test this we take the ratio N_1 / N_2 where N_1 (N_2) is the number of events in figure 4-16 (4-21 a) below $\theta_1 + \theta_2 = 72^\circ$. This ratio is compared to N_3 / N_4 where N_3 (N_4) is the number of events in figure 4-16 (4-21 a) above $\theta_1 + \theta_2 = 102^\circ$. The results

$$\frac{N_1}{N_2} = 1.07 \pm 0.18\,, \qquad \text{and} \qquad \frac{N_3}{N_4} = 1.09 \pm 0.07 \qquad (4.13)$$

are the same within statistical error indicating that the two distributions have the same shape in their outer regions. To estimate the number of background counts in figure 4–16, and hence the background counts in the $N(\theta)$ distribution of figure 4-20, the number of counts in figure 4-21 (a) in the region $72^\circ < \theta_1 + \theta_2 < 102^\circ$ is determined. This number is scaled by the weighted average of the above ratios (1.09 ± 0.07) and twice this result gives the number of bad p-p events included in the $N(\theta)$ distribution. It is found that 1.5 ± 0.2 % of the events in figure 4-20 are background events. The error estimate includes only statistical sources of uncertainty.

The analysis was repeated by sampling the regions below $\theta_1 + \theta_2 = 74^\circ$ and above $\theta_1 + \theta_2 = 104^\circ$. This trial gave a result of 1.6 ± 0.2 % background where the error estimate is statistical. The difference between these results gives a measure of the systematic error in this analysis. Thus the number of bad p-p events included in the $N(\theta)$ distribution is ~ 1.6 ± 0.3 %.

A similar study could have been performed by observing the coplanarity

(a) Opening Angle of Non-Coplanar Events

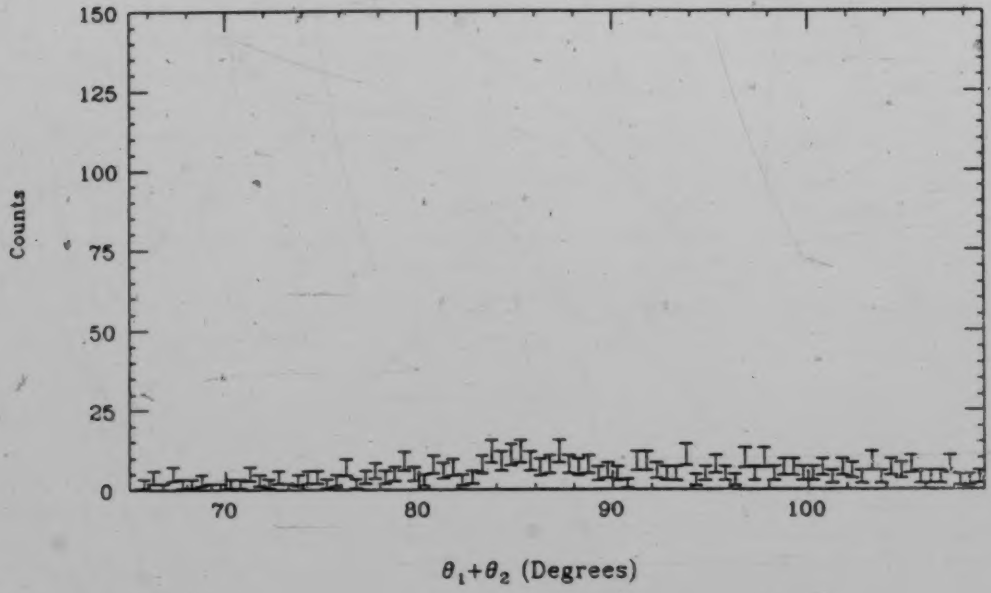

(b) Radial Vertex Position of Non-Coplanar Events

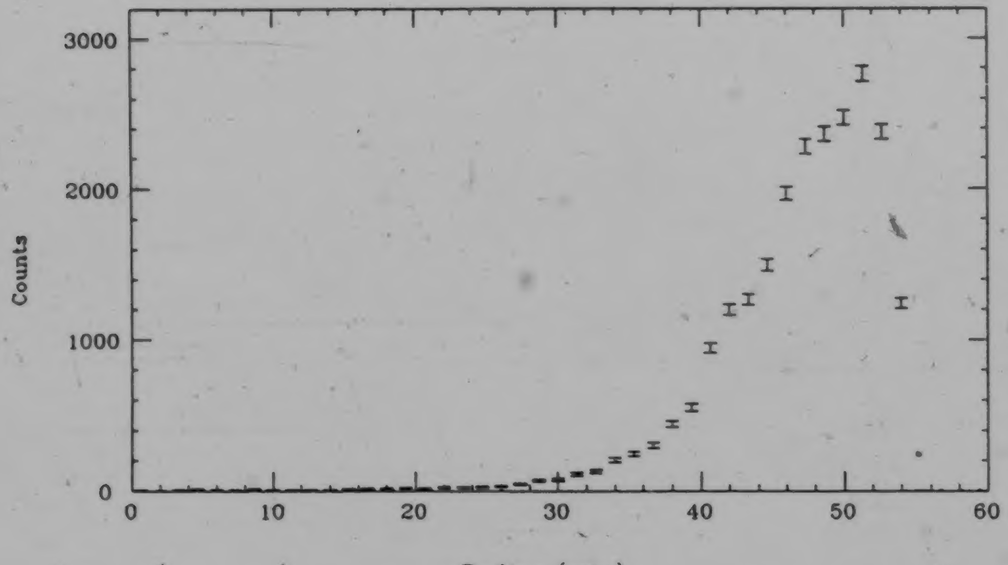

Figure 4-21 Opening Angle and Vertex Position of p-p Events Failing the Coplanarity Test.

distribution of those events that satisfy all cuts except opening angle. However, the coplanarity test can be passed by any two - body interaction. Since the opening angle restriction is fairly specific to p - p events the above result provides the most reliable estimate of the background.

The number of good p-p events rejected by the final cuts can be estimated from figure 4-21 (b) which shows the spectrum of the radial position of the interaction vertex for the non-coplanar events. It is believed that the background counts from the wall of the target has a similar distribution. This allows the target wall to be subtracted from figure 4-19. The tail of the resulting H_2 distribution in figure 4-19 can be observed and the number of good p-p events outside the RADIUS - CUT < 30 mm can be estimated. Figure 4-21 (b) is normalized to the target wall of figure 4-19 based on the number of counts outside R = 38.0 mm for both figures. The number of counts outside R = 30 mm after the subtraction of the target wall indicates that the number of good p-p events rejected by the radius cut is 2.7 ± 0.2 % of the counts in the N(θ) distribution. The error estimate is statistical only.

The analysis was repeated by normalizing the target wall of the two figures based on the number of counts outside R = 42.0 mm. This trial gave a result of 3.8 ± 0.4 % where the error estimate is statistical. The systematic error in this analysis can be estimated from the difference in the two results. Thus the number of good p-p events rejected by the final cuts is ~ 3 ± 1 % of the counts in the N(θ) distribution.

G) Scintillator Energy Calibration

As shown in chapter 3 the total light collected by the E scintillators varies by only a few percent over their length (figure 3-11). The total light collected by the dE scintillators is assumed to be position independent also. The position independence of the total light collection allows for a simple energy calibration of the SALAD scintillators.

The measured upstream and downstream ADC values of a given E or dE scintillator are combined as outlined in appendix B-VI to remove the position dependence of the individual ADC values. This new quantity ADC_{Total}, is converted to an energy value by dividing by a constant factor or *gain*. Thus the measured energy is given by

$$E_{Measured} = \frac{ADC_{Total}}{gain} . \qquad (4.14)$$

To determine the gain for a given E or dE scintillator bar, a calculation of E_{Calc}, the actual energy deposited in the scintillator, is made. If the proton beam energy, the interaction vertex and the direction of the scattered proton through the detector are known, the amount of energy lost in each material in the detector can be calculated. The vertex position can be confidently determined for p-p coincidence events only, so the reduced data set is used for the gain determinations.

An initial guess as to the gain for a given scintillator is made and a histogram of the missing energy (E_{Calc} - $E_{Measured}$) is made. If the gain is correct this histogram will have a centroid of zero and a width indicative of the energy resolution of the scintillator. If the centroid is non-zero a new gain is calculated which will bring the centroid closer to zero. A new energy difference histogram is made and if necessary a new gain is calculated. This iterative process rapidly converges and a gain is determined for each E and dE scintillator. The results of the scintillator energy calibration is shown in figure 4-22. Each missing energy spectrum is a sum over of all 24 scintillators.

A program ELOSS was written to quickly calculate the values of E_{Calc}. ELOSS utilizes range versus energy tables for protons in the materials used to construct SALAD. The energy scale in each table ranges from 1 MeV to 500 MeV in increments of 1 MeV. A linear interpolation is used to find the range R of a proton of energy E_1 in a given material. Then a linear interpolation is used to find the energy E_2 of a proton whose range is R - t where t is the thickness of material through which the proton is entering. The energy lost by the proton is given by,

$$E_{Loss} = E_1 - E_2 . \qquad (4.15)$$

The range - energy tables were generated using LOSSPROG(13). A comparison was made between ELOSS and LOSSPROG for calculating E_{Loss} values for protons of energy between 1MeV and 220 MeV incident on a thick (127.0 mm) and thin (3.2 mm) sheet of CH_2. The worst disagreement in E_{Loss} values was 0.15% in the case of the

(a) E–Scintillator Missing Energy

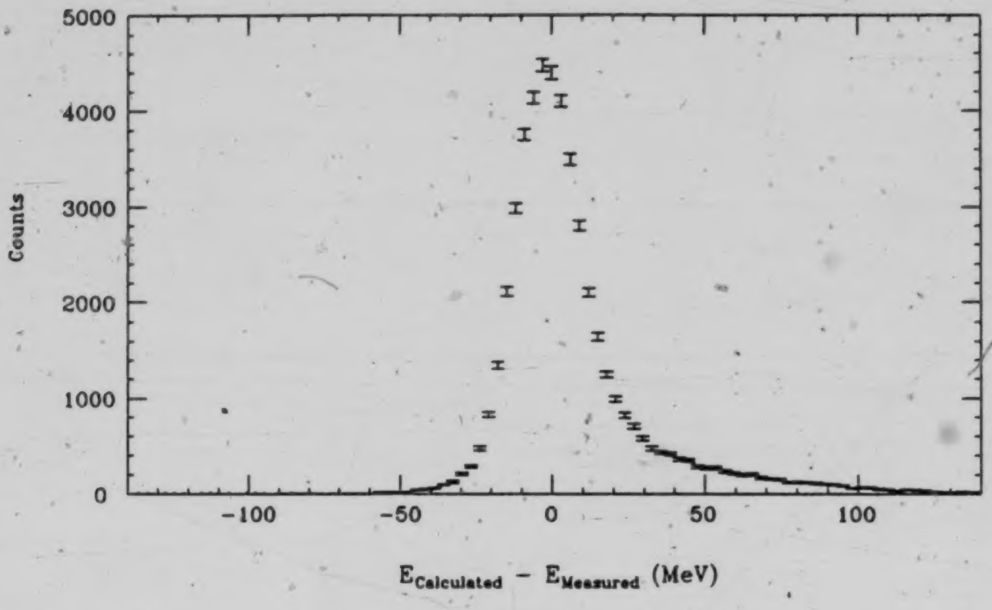

(b) dE–Scintillator Missing Energy

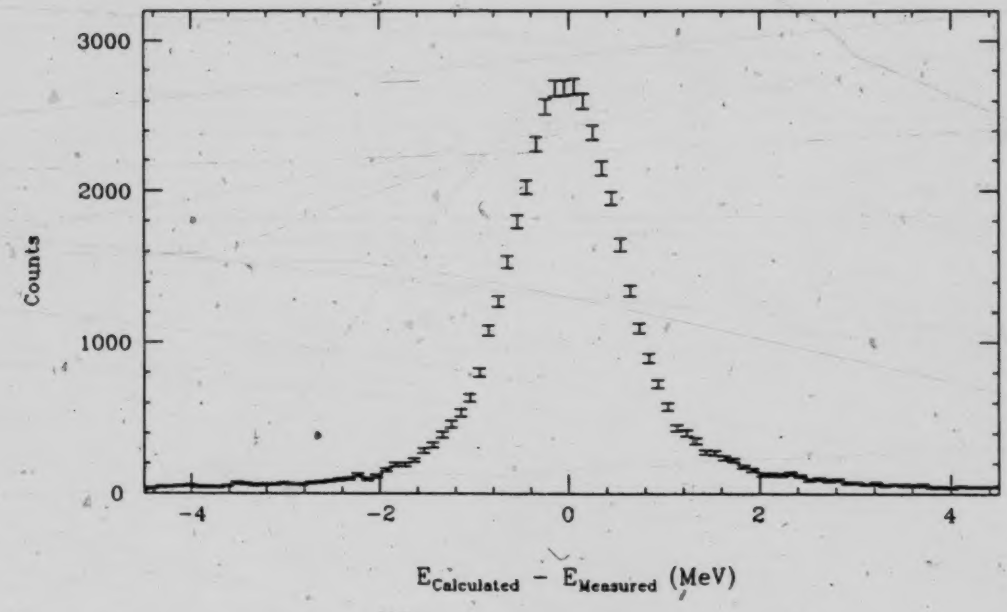

Figure 4-22 Missing Energy Spectra of the SALAD E and dE Scintillators.

thick sheet and 1.8% in the case of the thin sheet. These deviations are not significant considering that the estimated error in E_{Loss} values generated by LOSSPROG is ~ 5%.

The range R of a particle of charge ze, mass m and kinetic energy T are related to the range R_p and energy T_p of a proton in the same medium by the relations,

$$R = \frac{m}{z^2 m_p} R_p \qquad \text{and} \qquad T = \frac{m}{m_p} T_p \quad , \qquad (4.16)$$

where m_p is the proton mass. These relations allow the range - energy tables for protons used in ELOSS to be converted to range - energy tables for particles heavier than electrons. ELOSS can be used to calculate E_{Loss} values for protons, pions, muons, deuterons, ^{3}He and ^{4}He.

ELOSS was used to calculate the energy lost by the scattered protons in SALAD as a function of θ_{Lab}, for interactions which take place on the z - axis of the detector and which do not pass through the aluminum portion of the target cell. The results are shown in figure 4-23. The top curve is the kinematic energy of the scattered proton for a beam energy of 220 MeV. The middle curve shows the energy of the proton as it enters the dE scintillator. The difference in energy between the top and middle curves for a given angle is the energy lost in all the materials between the target gas and the dE scintillator as listed in table 2-1. The bottom curve shows the energy deposited in the E scintillators which stop the protons for all lab angles. The difference in energy between the middle and bottom curves for a given angle is the energy deposited in the dE scintillators.

It is known from geometry that a proton scattered at an angle of 8° cannot pass through both the inner and outer wire chamber pairs, strike a dE scintillator and give an event trigger. This geometrical cut off is indicated in figure 4-23. This figure also shows that protons scattered at 72° do not have enough energy to get to the dE scintillators. Such an event can still be triggered as the complementary proton is scattered at 17° which is above the geometrical cut off. The large angle, or energy loss, cut off is ~ 84°. At this angle the proton does not have enough energy to reach wire chamber 4. If a hit is not recorded in wire chamber 4 a track cannot be found (as wire chamber 3 was not operational) and the event is not included in the p-p coincidence data set.

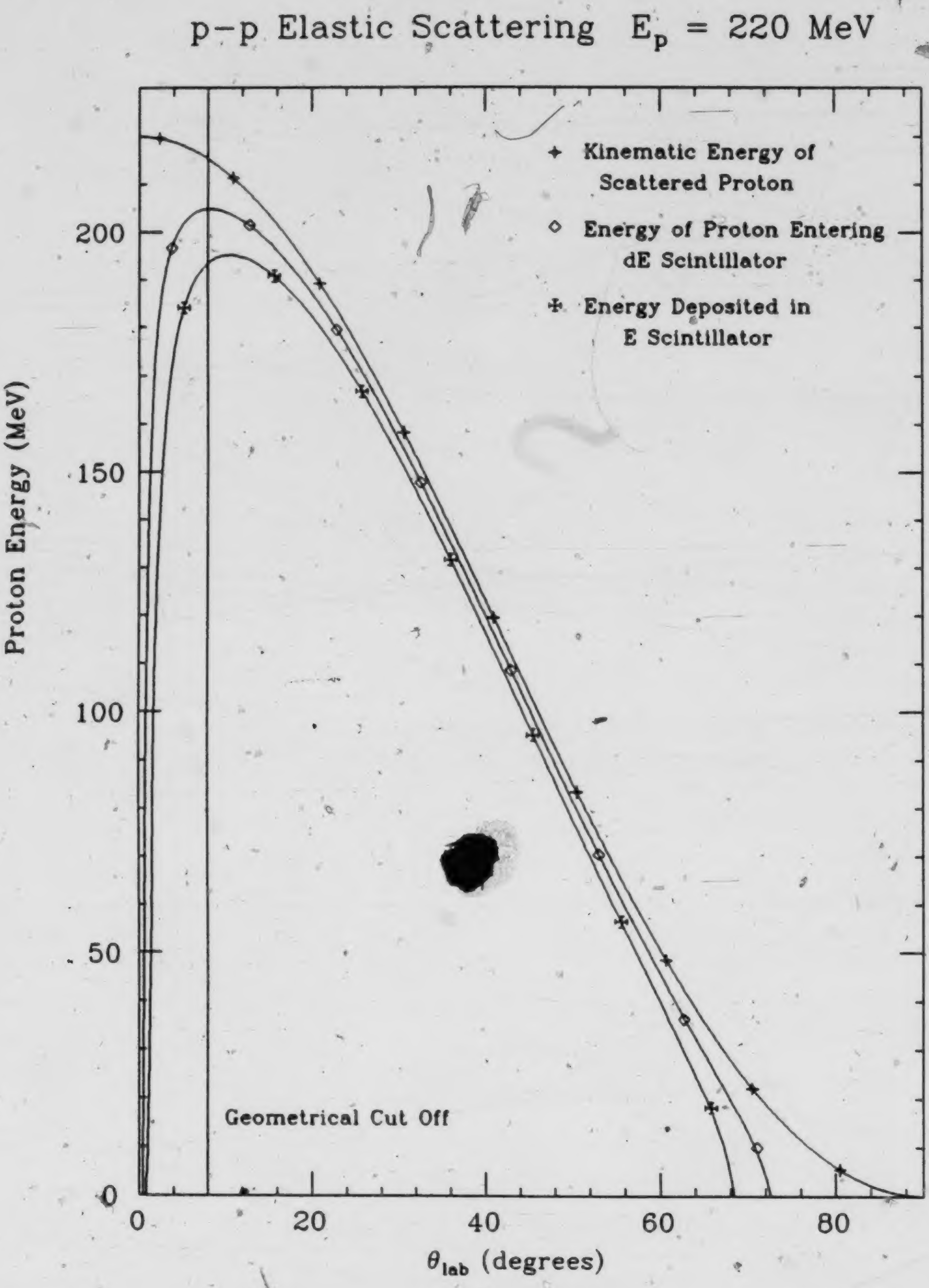

Figure 4-23 Energy Loss of Scattered Protons in SALAD as a Function of θ_{Lab}.

H) Efficiency Calculation From Monte Carlo Studies

A Monte Carlo simulation of the p-p elastic scattering process studied with SALAD was performed. The Monte Carlo code generates a data set which is analyzed by the same analysis package that is used to study the real p-p data set. For a single event, the azimuthal angle ϕ and the cosine of the polar angle θ is chosen at random in the center of momentum frame. These angles are converted to the lab frame and the energy of the scattered protons is calculated for a beam energy of 220 MeV.

As stated in part B, one p-p data run employed the strict SALAD trigger ($2E_{up} \cdot 2E_{dn} \cdot 2dE_{up} \cdot 2dE_{dn}$) while all other runs employed the trigger ($1dE_{up} \cdot 1dE_{dn}$). It is not completely clear how to model this mixed trigger in the Monte Carlo code. For this reason only data triggered on ($1dE_{up} \cdot 1dE_{dn}$) was utilized in producing the final $N(\theta)$ distribution. The Monte Carlo mimics this trigger by verifying that a scattered proton deposits at least 2 MeV in a dE scintillator (which is approximately the actual dE scintillator threshold).

The z vertex position of the event is chosen at random within the target cell, and the x and y coordinates of the vertex are chosen at random consistent with a prescribed beam divergence. With the introduction of geometric and energy loss constraints it is determined whether an event will satisfy an event trigger. For those events which satisfy a trigger, the elements within SALAD which give non-zero ADC information are determined along with an appropriate ADC value.

A wire chamber efficiency parameter is placed in the Monte Carlo code. [illegible] parameter is adjusted until the relative number of hits in each wire chamber, as determined by an analysis of the Monte Carlo generated data, is approximately the same as for the real p-p data. A parameter which reflects the position resolution of the wires is also placed in the code. The wire chamber calibration of section C showed that the position resolution of the wires is ~ twice at the ends what it is at the center. The Monte Carlo mimics this by assuming a linear change in resolution with position from the center of the wire. This parameter is adjusted until the width of the opening angle spectrum of the Monte Carlo data, shown in figure 4-24, is the same as the real p-p data. The energy resolution of the E and dE scintillators is modeled after the results of chapter 3, so that the resolution of the E scintillators is given by $0.336/\sqrt{E}$ and the resolution of the dE scintillators is given by $0.296 / \sqrt{E}$ where E is in MeV. The divergence of the beam is also parametrized and adjusted until the shape of the radial vertex position spectrum is approximately the same as for the real p-p data with the target wall subtracted. The beam divergence varied slightly from run to run when the p-p data was collected, so it is not possible to exactly match the radial vertex position of the Monte Carlo and p-p data. A beam divergence of 3.8 mRad in the Monte Carlo code gives the result shown in figure 4-25.

An estimate as to the total amount of inactive material between the target gas and the dE scintillators can be made from the information in table 2-1 (equivalent to ~ 3.2 mm of CH_2 of density 1.032 g / cm^3). The exact amount of inactive material cannot be calculated as the large number of graphite coated kapton strips used to separate the wire chamber cells contributes in a complicated way to the total. For this reason an inactive material parameter based on mm of CH_2 is put into the Monte Carlo code so that the additional energy loss due to the presence of the ribbons can be modeled.

All of the spectra generated by the data analysis software for the real p-p data can be generated for the Monte Carlo generated data. A summary of the Monte Carlo results as they compare to the p-p data is given in appendix C. The confidence in the Monte Carlo code is justified based on the very good agreement of the analysis results of the p-p and Monte Carlo data sets.

In many cases a comparison of the Monte Carlo and real p-p results have led to some important insights in the interpretation of the p-p data. For example, preliminary analysis showed a discrepancy between the minimum distance and RMS tracking error spectra of the Monte Carlo and p-p data sets. Careful examination of the individually reconstructed tracks relative to the wire chamber cells displaying hits (using diagrams like figure 4-4) indicated a small construction error. Making a + 10° rotation of wire chamber 1 (in software) with respect to the intended orientation caused the minimum distance and RMS spectra of the p-p data to agree with the Monte Carlo simulation. This rotation is shown implicitly in figure 2-6.

Another discrepancy was in the centroid of the opening angle distributions. The Monte Carlo predicted a centroid of 87° while the p-p data peaked at 90°. It was postulated that the two remote controlled ^{55}Fe sources do not line up when in their z = 0 positions. This would make the midpoint of the inner wire chambers (as defined by one source) skewed with respect to the midpoint of the outer wire chambers (as

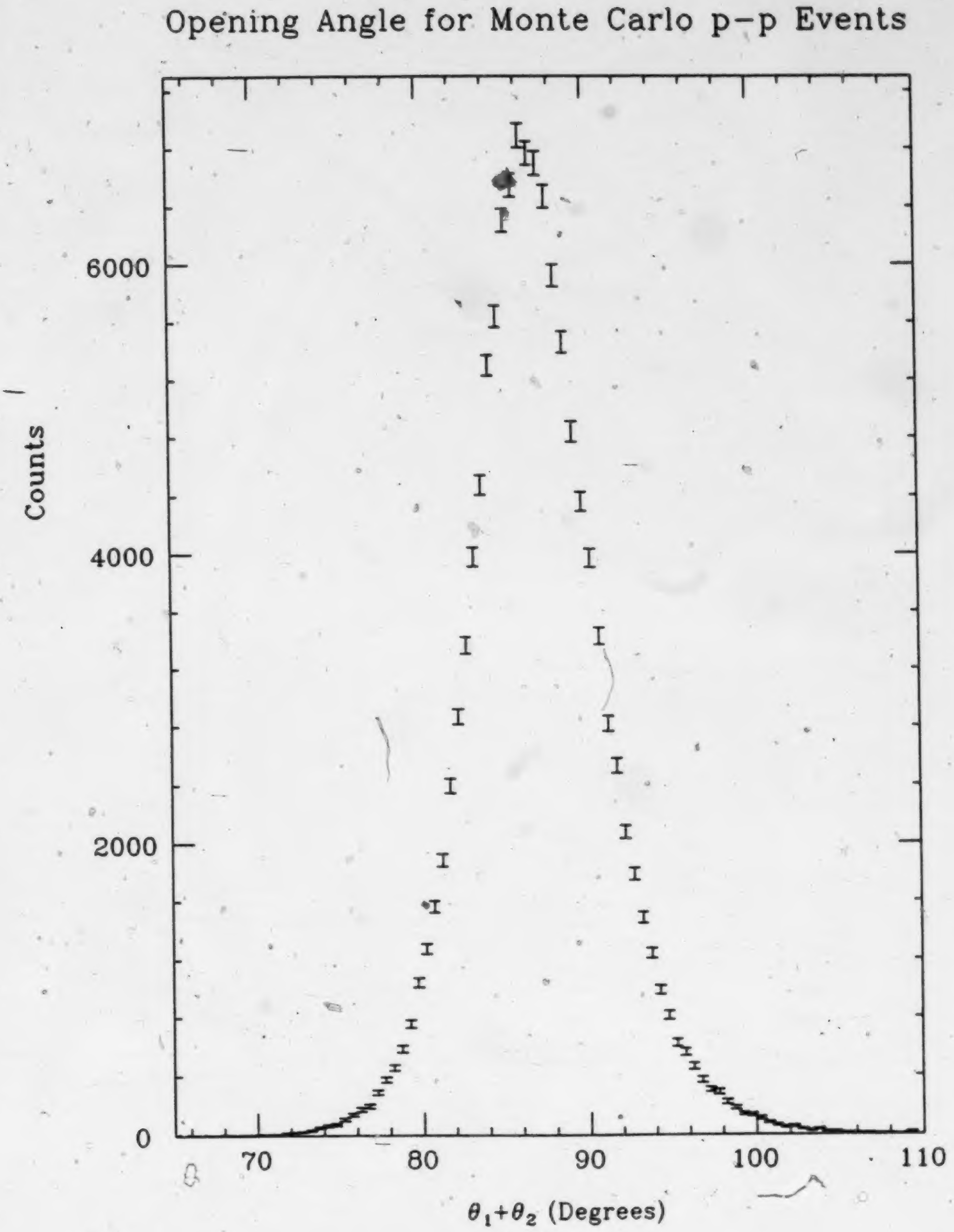

Figure 4-24 Opening Angle of the Monte Carlo Data Set.

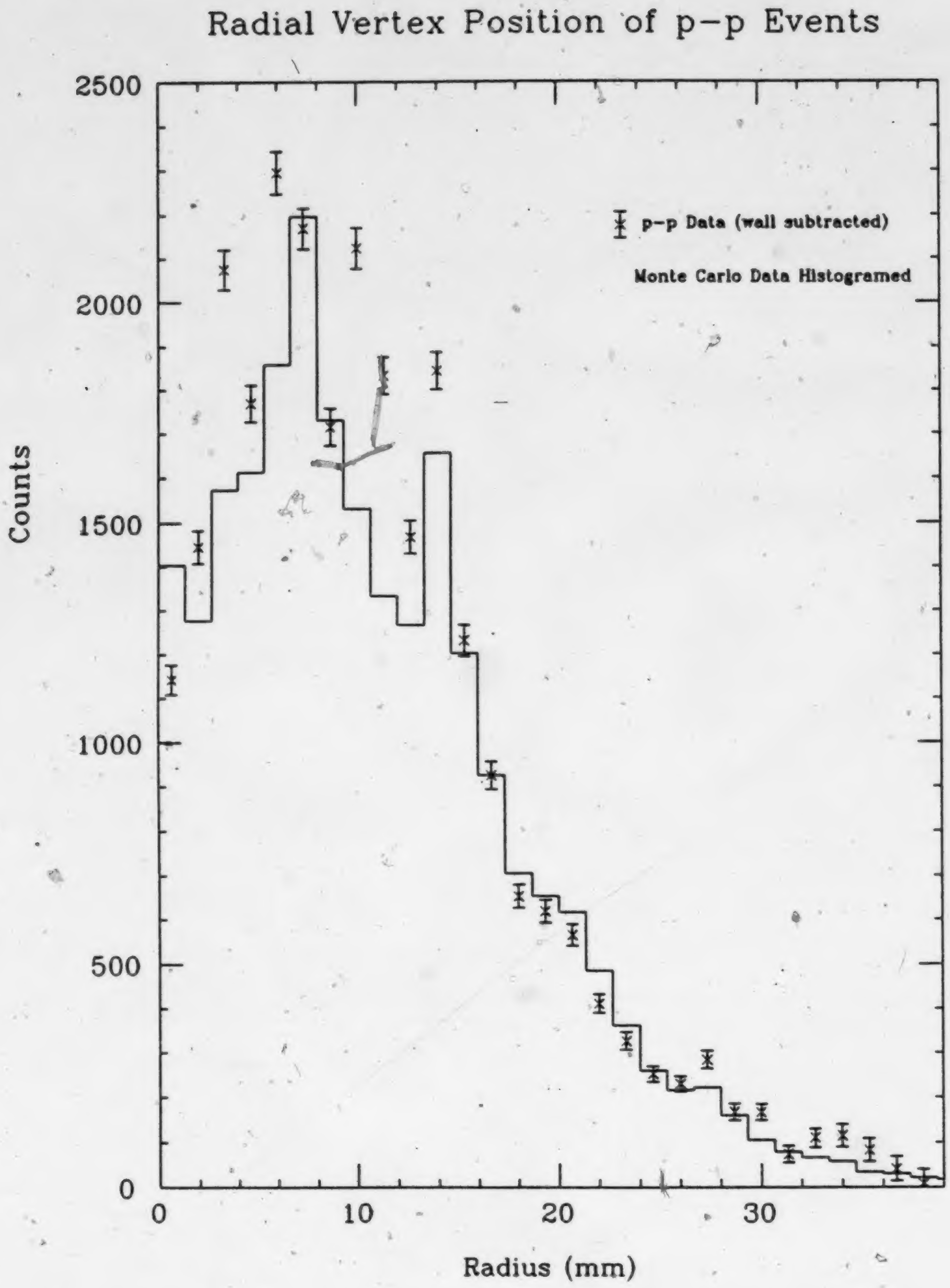

Figure 4-25 Comparison of the Radial Position of the p-p Interaction Vertex for the Monte Carlo and p-p Data Sets (Target wall subtracted from the p-p data).

defined by the other source). Shifting the outer wire chamber pair (in software) 6.5 mm with respect to the inner wire chamber pair removed the opening angle discrepancy.

Shifting the wire chamber pairs with respect to one another changes slightly the polar angle of the reconstructed tracks. The energy resolution of the scintillators, as indicated by the width of the missing energy spectra, was observed to improve by the resulting changes in polar angle. Unfortunately the missing energy spectra of the p-p data is still wider than that of the Monte Carlo data. This discrepancy remains to be understood, although a distribution of incident energies with $\sigma = 10$ MeV would remove the disagreement. Since scintillator information was not used to identify particles in the analysis of both the real p-p data set and Monte Carlo generated p-p data set, this discrepancy does not affect the results of the efficiency calculation.

The efficiency of SALAD is found from the Monte Carlo data in the following manner. The Monte Carlo code generates a uniform distribution of center of momentum polar angles θ_{CM}, (the distribution per unit solid angle is constant). This distribution is transformed to the lab frame by converting the CM angles to lab angles. The result is the θ_{Lab} distribution that a perfect 4π detector would find for the real p-p data set. This distribution is shown in figure 4-26. Each event is then tracked through the detector. Geometric and energy loss restrictions are imposed and if the event is found to satisfy the event trigger (the same event trigger employed by SALAD) it is included in the the Monte Carlo generated p-p data set. This data set is then analyzed in the same manner as the real p-p data set (the cuts applyed to the real p-p data set are applied to the Monte Carlo generated p-p data set) and the distribution of p-p coincidence events as a function of θ_{Lab} is determined. The resulting Monte Carlo $N(\theta)$ p-p coincidence distribution is shown in figure 4-27. The ratio of the number of counts in figure 4-27 to the number counts in figure 4-26 at a given angle gives the calculated efficiency of SALAD for detecting coincidence events at that angle. Thus the p-p coincidence efficiency as a function of angle can be mapped for SALAD. The efficiency of SALAD for detecting p-p events in coincidence is shown in figure 4-28.

The efficiency of SALAD for detecting p-p one track events is determined by analyzing the same Monte Carlo data set rejecting all coincidence events. The singles efficiency is given by the number of single tracks observed at a given angle divided by

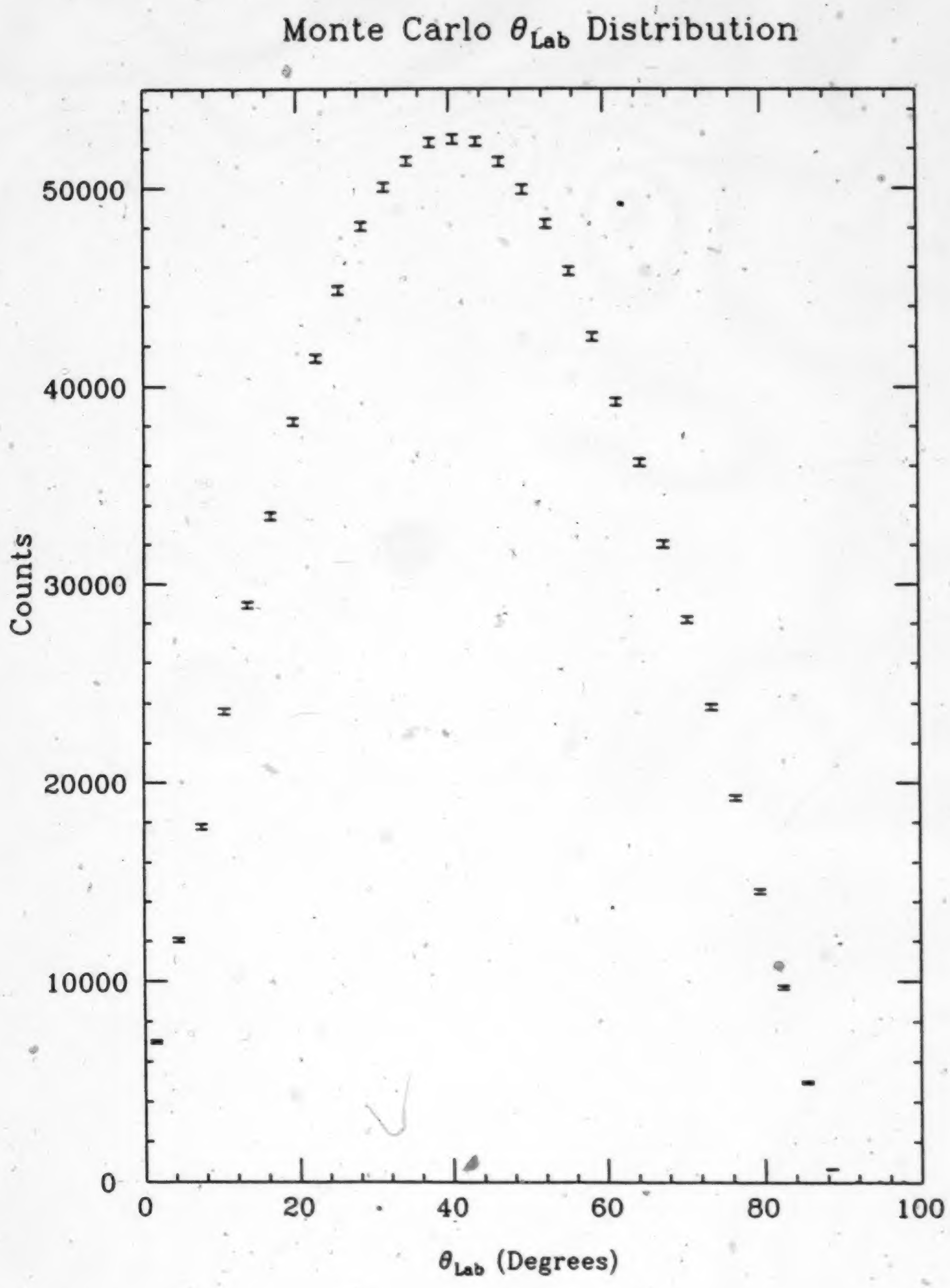

Figure 4-26 θ_{Lab} Distribution Used to Generate the Monte Carlo Data Set.

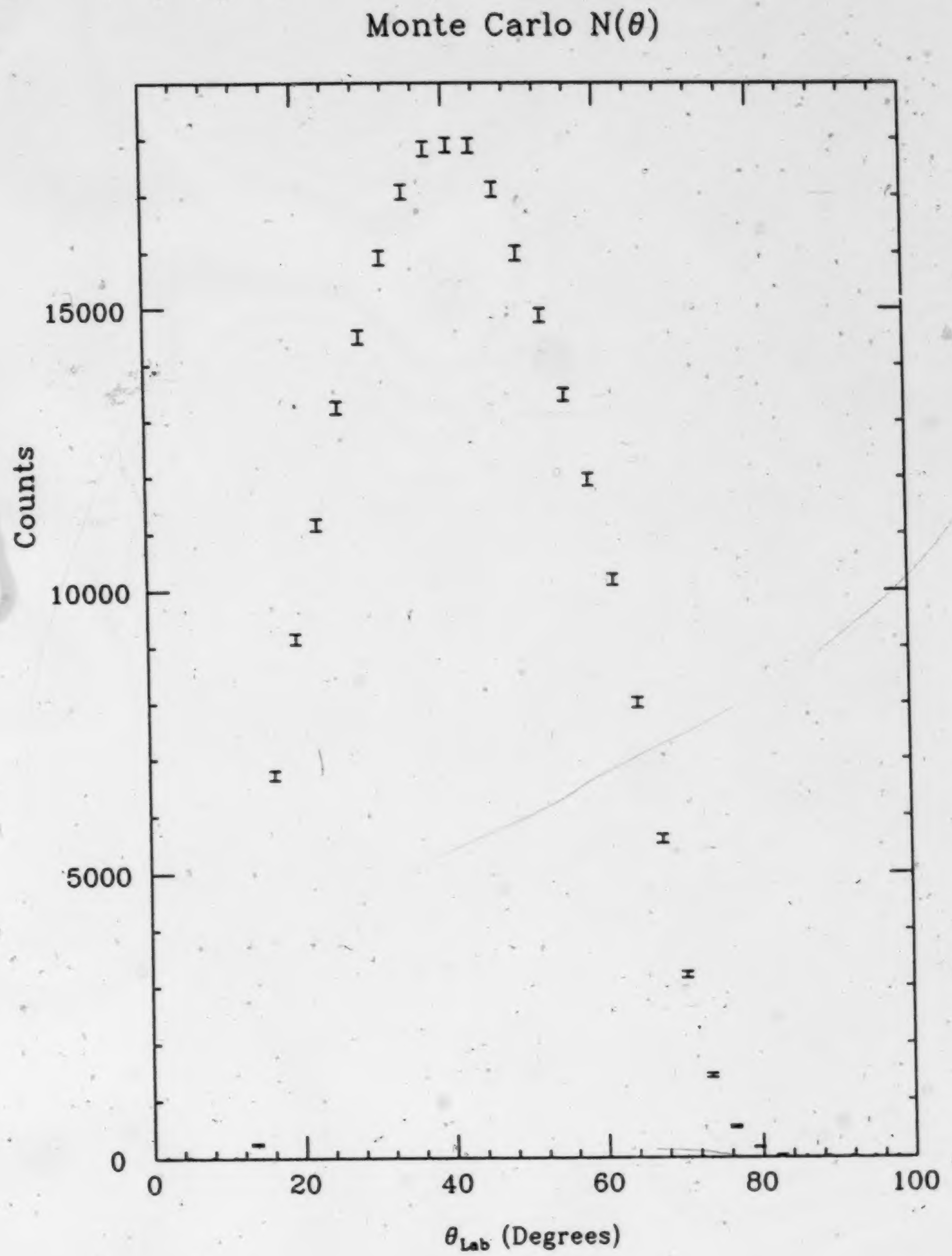

Figure 4-27 N(θ) Distribution of the Analyzed Monte Carlo Data Set.

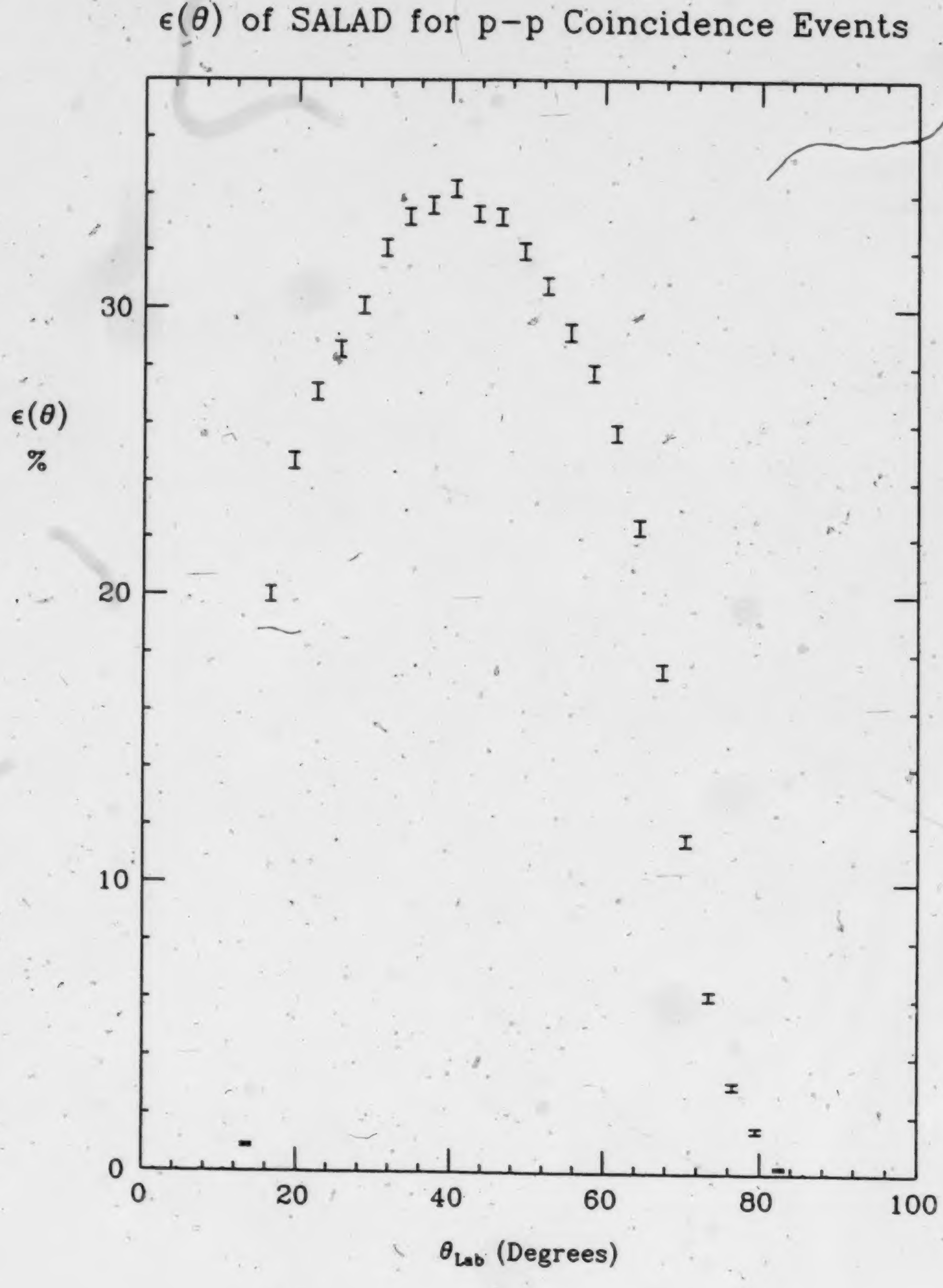

Figure 4-28 Efficiency of SALAD for Detecting p-p Coincidence Events.

(a) SALAD Single p−p Efficiency

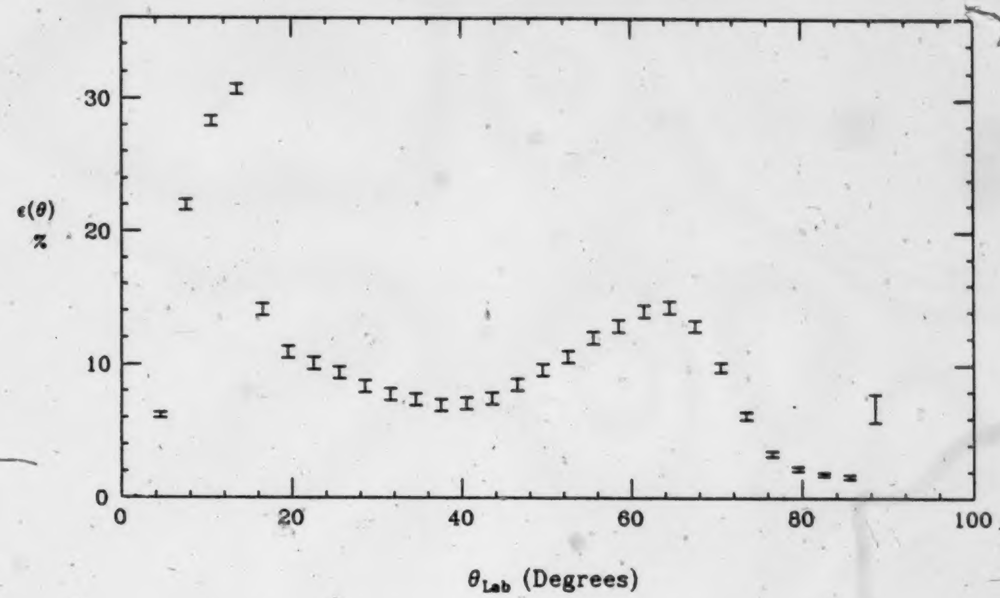

(b) Total SALAD p−p Efficiency

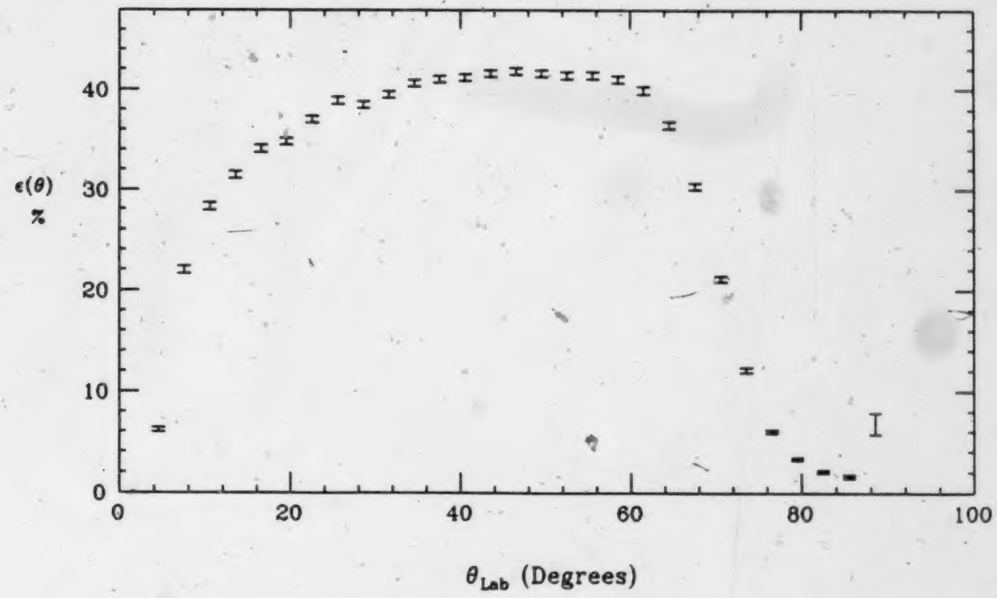

Figure 4-29 The (a) Single and (b) Total Efficiency of SALAD for Detecting p-p Events.

the number of events generated at that angle. The efficiency for p-p one track events is shown in figure 4-29(a). The net efficiency, defined as the sum of the one and two track efficiencies, is shown in figure 4-29 (b).

I) The p(p,p)p Elastic Scattering Differential Cross Section

The p-p coincidence $N(\theta)$ distribution for the SALAD trigger ($1dE_{up} \cdot 1dE_{dn}$), and the SALAD efficiency $\varepsilon(\theta)$ for detecting p-p coincidence events for the same trigger have been determined. The elastic scattering differential cross section can thus be found from equation 4.4,

$$\frac{d\sigma}{d\Omega}(\theta) = \frac{N(\theta)}{\int \varepsilon(\theta)\, N_T\, 2\pi \sin\theta\, d\theta\, F_B(t)\, dt} \quad . \tag{4.4}$$

A measurement of the relative cross section is sufficient to evaluate the reliability of the efficiency calculation. For this reason no attempt is made to obtain the absolute normalization of the cross section. With the beam flux integral $\int F_B(t)\, dt$ and the H_2 target thickness N_T, normalized to unity, equation 4.4 becomes,

$$\frac{d\sigma}{d\Omega}(\theta) \propto \frac{N(\theta)}{\varepsilon(\theta)\sin\theta} \quad . \tag{4.17}$$

The p-p elastic scattering cross section as determined from equation 4.8 is shown in figure 4-30.

Also shown in figure 4-30 is a theoretical calculation of the p-p elastic scattering cross section at $E_P = 220$ MeV using the Scattering Analysis in the Interactive Dial-In program (or SAID[(20)]). SAID provides a partial - wave analysis of the NN interaction below a laboratory kinetic energy of 1300 MeV. The partial waves used to calculate various NN observables, including the cross section, are extracted from a data base of 9778 p-p and 5729 n-p elastic scattering observations below 1300 MeV (as of July

1987)(21). Some relevant p-p data used in fitting the phase shifts is shown in figure 4-30 is given in table 4-1(22,23) and shown in the figure.

Table 4-1 p(p,p)p Elastic Scattering Cross Section Data Used by SAID.

Energy (MeV)	θ_{cm} (degrees)	θ_{lab} (degrees)	$\frac{d\sigma}{d\Omega_{cm}}$ (mb/sr)	$\frac{d\Omega_{cm}}{d\Omega_{lab}}$	$\frac{d\sigma}{d\Omega_{lab}}$ (mb/sr)
213	8.9	4.2	4.86 ± 0.12	4.45	21.63 ± 0.53
	9.8	4.6	4.12 ± 0.10	4.45	18.32 ± 0.44
	10.4	4.9	3.67 ± 0.09	4.44	16.31 ± 0.40
	12.2	5.8	3.49 ± 0.06	4.44	15.48 ± 0.27
	13.2	6.3	3.47 ± 0.07	4.43	15.37 ± 0.31
	14.8	7.0	3.50 ± 0.04	4.42	15.47 ± 0.18
	17.2	8.1	3.55 ± 0.06	4.40	15.63 ± 0.26
	18.5	8.8	3.59 ± 0.04	4.39	15.77 ± 0.18
	19.4	9.2	3.55 ± 0.04	4.38	15.57 ± 0.18
	21.7	10.3	3.77 ± 0.06	4.36	16.45 ± 0.26
	24.2	11.5	3.72 ± 0.03	4.34	16.14 ± 0.13
	29.0	13.8	3.76 ± 0.03	4.28	16.11 ± 0.13
	38.7	18.4	3.67 ± 0.05	4.14	15.21 ± 0.21
210	30.0	14.2	3.70 ± 0.04	4.27	15.80 ± 0.17
	40.0	19.0	3.73 ± 0.04	4.12	15.38 ± 0.16
	50.0	23.8	3.62 ± 0.04	3.94	14.25 ± 0.16
	60.0	28.6	3.55 ± 0.04	3.72	13.20 ± 0.15
	70.0	33.5	3.57 ± 0.04	3.47	12.40 ± 0.14
	80.0	38.4	3.57 ± 0.04	3.20	11.44 ± 0.13
	90.0	43.4	3.52 ± 0.04	2.91	10.26 ± 0.17

The SALAD cross section results are normalized to the theoretical curve by multiplying by a constant scaling factor (ξ). The scaling factor is chosen such that the χ^2 per degree of freedom value calculated from

$$\chi^2 = \frac{1}{23 - 1} \sum_{\theta = 16^\circ}^{84^\circ} \frac{\left[\xi\left(\frac{d\sigma}{d\Omega}(\theta)\right)_{SALAD} - \left(\frac{d\sigma}{d\Omega}(\theta)\right)_{SAID}\right]^2}{\delta\left(\frac{d\sigma}{d\Omega}(\theta)\right)^2_{SALAD}} \qquad (4.9)$$

is minimized.

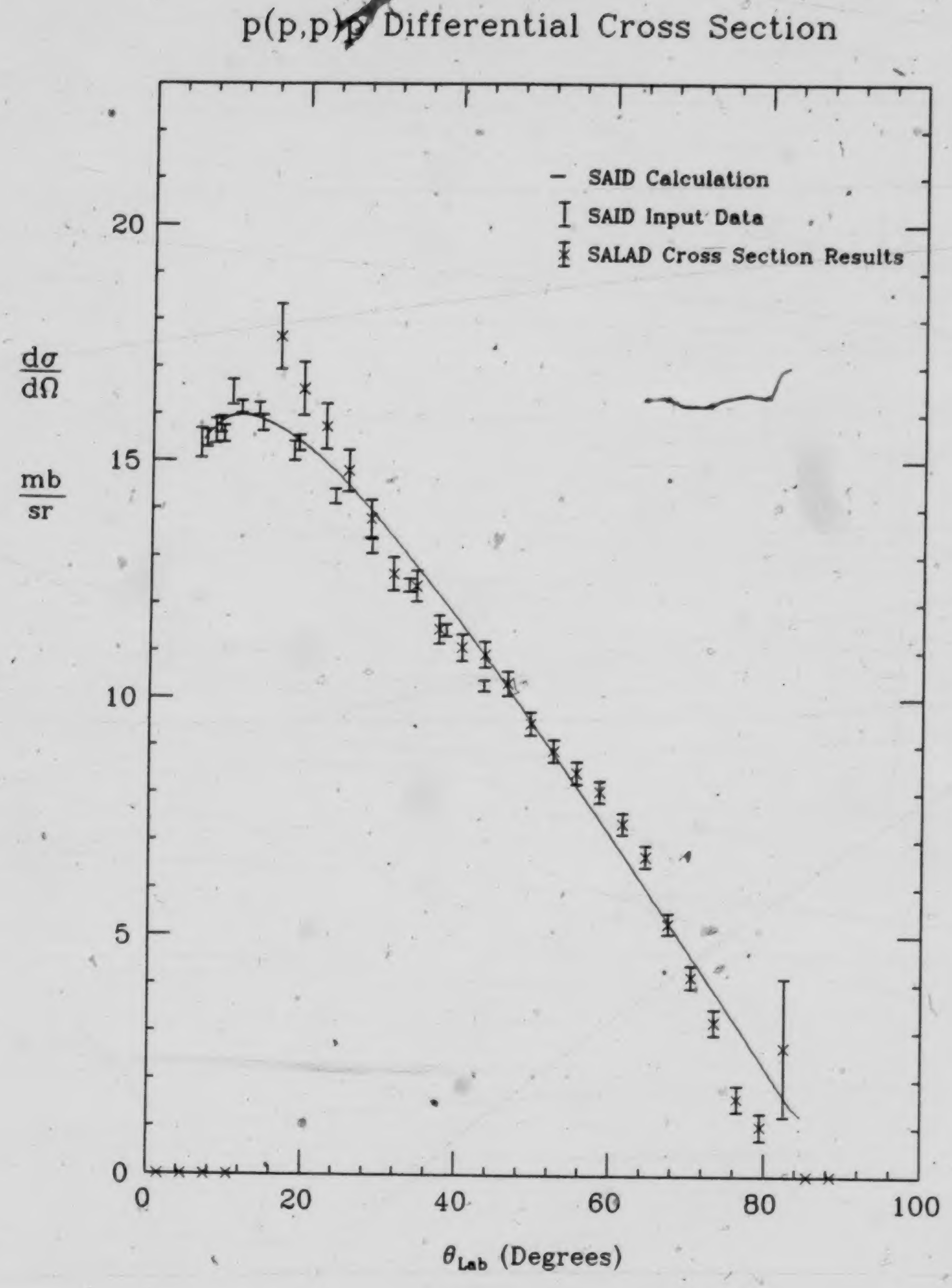

Figure 4-30. The p-p Elastic Scattering Cross Section.

In comparison to the SAID curve, the SALAD p-p cross section has a discernable 'S' shape. The discrepancy could lie in either the p-p N(θ) distribution shown in figure 4-20 or the Monte Carlo efficiency calculation shown in figure 4-28.

The shape of the p-p coincidence efficiency curve is characterized by its height in percent and in its angular width. Monte Carlo studies have shown that the height of the efficiency curve depends primarily on the lengths of the gas target cell, wire chambers and calorimeter within SALAD and upon their relative positions. These lengths and positions are known precisely and can be put into the Monte Carlo code in an unambiguous way. Monte Carlo studies have also shown that the width of the efficiency curve depends primarily on the amount of inactive material between the gas target cell and the dE scintillators. An adjustment of the amount of inactive material is effectively an adjustment of the energy loss properties of the detector. This has important effects particularily at large θ_{lab} where the energy of the scattered protons is low.

Another parameter which affects the width of the efficiency curve to second order is the divergence of the beam. At the angular extremes the geometric acceptance of the detector is quite sensitive to the distance between the axis of the detector and the interaction vertex.

The final values of the inactive material and beam divergence parameters were selected so as to give the smallest χ^2 fit of the measured p-p cross section to the theoretical curve. The possible range of beam divergence values was determined by the radial vertex position studies discussed in section H. The search for a final value was restricted to the range 3.5 mRad to 4.0 mRad. With all the materials outlined in table 2–1 included in the Monte Carlo code, the inactive material parameter (based on mm of CH_2) should not be large. The search for its final value naturally starts at zero. The best values of the beam divergence and inactive material parameters based on the χ^2 analysis were found to be 3.8 mRad and 0.7 mm CH_2 respectively. These values were used in figure 4-30 which has a reduced χ^2 value of 5.3. It was observed that the fluctuation of the p-p elastic scattering cross section about the theoretical curve persisted for all values of beam divergence and inactive material studied.

CHAPTER 5

CONCLUSION

As discussed in the introduction, an accurate data set is essential for the understanding of the photonuclear interaction. The Saskatoon Alberta Large Acceptance Detector (SALAD) has been built for use with the tagged photon facility at the Saskatoon Accelerator Laboratory (SAL) in the hope of contributing to this accurate data set.

A detailed description of SALAD has been given in chapter 2. Its notable features are a large angular acceptance, a high pressure gas target cell and a low amount of inactive material between the target gas and the calorimeter. Various aspects of the detector have been studied and are described in chapters 3 and 4. What has been learned?

The scintillator tests of chapter 3 showed that the attenuation lengths of the E and dE scintillators are $\lambda_E = 323 \pm 31$ cm and $\lambda_{dE} = 133 \pm 41$ cm respectively. The energy resolution of the E and dE scintillators have been found and can be expressed as,

$$E_{Res} \approx \frac{33.6\%}{\sqrt{E}} , \qquad dE_{Res} \approx \frac{29.6\%}{\sqrt{E}}$$

where E is the kinetic energy of the particle entering the scintillator. Also the light collection and energy resolution of the E scintillators were found to be very nearly position independent. The data available did not allow a similar study for the dE scintillators.

The efficiency test of chapter 4 is important for assessing the performance of both SALAD and the Monte Carlo software. As far as SALAD is concerned, the wire chamber z-position determinations are very good ($\sigma_z \sim 1.3$ mm at $z = 0$, and $\sigma_z \sim 2.6$ mm at $z = \pm 44$ mm). This small error in z coupled with good x - y position determinations allows accurate track reconstructions. Histograms of opening angle, coplanarity, minimum distance and radial position of the interaction vertex can be made based on the track reconstructions. These histograms were made for the p(p,p)p elastic scattering data collected by SALAD at TRIUMF on BL1B. After applying relatively loose cuts to the histograms the angular distribution of the p-p coincidence events, N(θ), was determined. The number of good p-p events rejected by the cuts was estimated to be ~3 ± 1 %, and the number of background events satisfying the cuts was estimated to be ~1.6 ± 0.3 %. Thus SALAD performed very well in determining the p–p coincidence N(θ) distribution.

The confidence in the Monte Carlo code is high for two reasons. First, in preliminary Monte Carlo studies a few important discrepancies were found between the analyzed real p-p and Monte Carlo generated p-p data sets. These discrepancies prompted fundamental questions which have led to an in-depth understanding of the p–p data set, the Monte Carlo generated p-p data set and the code used to analyze both data sets (see section 4-H). The second reason follows from the first in that the analyzed real p-p and Monte Carlo generated p-p data sets give very similar results. Thus the Monte Carlo code is well understood and appears to perform very well in determining the efficiency of SALAD for detecting p-p coincidence events.

On an individual basis both SALAD and the Monte Carlo code appear to perform very nicely. The true test however, comes when both are combined to determine the shape of the p-p elastic scattering differential cross section. In comparison to the theoretical cross section the SALAD results are generally quite good. The SALAD data points follow closely the downward trend of the theoretical prediction. The data does however tend to fluctuate about the theoretical curve. The generally good agreement between the measured and theoretical cross section is promising. However, the small discrepancy indicates that either a slight modification in the p-p data analysis must be made, or the Monte Carlo must be 'fine-tuned', or both.

An example of a slight modification to the p-p data analysis is the following. The outer wire chamber pair was shifted by 6.5 mm in software with respect to the inner wire chamber pair in order to remove a discrepancy between the centroids of the p-p and Monte Carlo opening angle distributions (see section 4-H). This shift obviously alters the N(θ) distribution of the p-p coincidence events. How this shift affects the resulting p-p elastic scattering cross section measurement was tested. The p–p cross section was recalculated using analysis runs where the shift was set to 5.0 and 8.0 mm. The fluctuation persisted and the resulting χ^2 values were 5.5 and 10.4

respectively. The shift parameter of 6.5 mm not only removes the opening angle discrepancy but appears to give the best χ^2 result which in this case was 2.7.

An attempt to fine tune the Monte Carlo was performed in section 4-I where the beam divergence and inactive material parameters were adjusted. There it was found that no combination of these two parameters could remove the fluctuation in the calculated p-p cross section. The values of these parameters have been chosen to minimize the χ^2. Clearly further attempts to remove the fluctuation are necessary.

One aspect of the Monte Carlo that needs to be explored further is the sensitivity to the event trigger. Because of the complexity in understanding the strict SALAD trigger ($2E_{up} \cdot 2E_{dn} \cdot 2dE_{up} \cdot 2dE_{dn}$), only the data triggered on ($1dE_{up} \cdot 1dE_{dn}$) was used for the comparison of the p-p cross section results to the theoretical prediction. However, even this simple trigger has probably not been modeled adequately. The suspected problem is as follows. SALAD was triggered if both the dE-up *and* dE-dn values were above their individual discriminator thresholds. It was observed that the resulting p-p dE threshold as calculated from

$$\frac{\sqrt{ADC^{p\text{-}p}_{dE\text{-}up} \times ADC^{p\text{-}p}_{dE\text{-}dn}}}{gain}$$

is 2 MeV on average. The Monte Carlo calculates the value of

$$\frac{\sqrt{ADC^{MC}_{dE\text{-}up} \times ADC^{MC}_{dE\text{-}dn}}}{gain}.$$

If this value is ≥ 2 MeV an event is said to have been triggered. However, the Monte Carlo does not check if the $ADC^{MC}_{dE\text{-}up}$ and $ADC^{MC}_{dE\text{-}dn}$ values satisfy their individual discriminator thresholds. The 2 MeV condition could be passed even though one of the ADC^{MC} values may fail its individual threshold test.

It would be straight forward to do this ADC^{MC} test in the Monte Carlo code but unfortunately it is very difficult at this stage to determine the individual discriminator thresholds of the 48 dE PMT's. This is because there are electronic (fastbus) ADC thresholds that are folded in with the discriminator thresholds. If a test can be devised so that the discriminator thresholds alone determine the result then the discriminator thresholds can be determined. In the future, care must be taken to determine the discriminator thresholds on line.

It should also be mentioned that no scintillator energy information was used in determining the N(θ) distribution of both the real p-p and Monte Carlo p-p data sets. In both cases particle identification was accomplished by applying opening angle, coplanarity and radial vertex position restrictions. Since scintillator information did not enter into the ε(θ) calculation, the discrepancy between the widths of the missing energy spectra of the real p–p and Monte Carlo p-p data sets could be neglected. When scintillator information is needed for particle identification this discrepancy must be resolved.

To conclude, the p-p elastic scattering data has greatly increased the understanding of the Saskatoon Alberta Large Acceptance Detector. It appears, however, that some minor adjustments must be made to either the Monte Carlo or the data analysis. It is expected that SALAD will be an excellent tool for use in the tagged photon beam at SAL, creating an opportunity to produce high quality data in a number of photonuclear reactions.

REFERENCES

1. J. Chadwick and M Goldhaber. *Nature*, **134** (1934) 237.
2. E. Fermi. *Physical Review*, **48** (1935) 570.
3. A. J. F. Seigert. *Physical Review*, **52** (1937) 787.
4. J. M. Laget. *Physics Reports* **69** (1981) 1.
5. H. O. Meyer. *Canadian Journal of Physics* **62** (1984) 1109.
6. J. M. Cameron. *Canadian Journal of Physics* **62** (1984) 1019.
7. N. E Davison and D. A. Hutcheon. *Canadian Journal of Physics* **62** (1984) 1019 - 1128.
8. R. Pywell. *Notes on High Energy Photon Tagging*, SAL Internal Report, Linac Spect #132x8521. January 27, 1987.
9. J. M. Laget, *Nuclear Physics* **A312** (1978) 265.
10. M. W. K. Rosenow, *COMPOSITES*. **15** (1984) 144.
11. G. C. Eckold, *COMPOSITES*. **16** (1985) 8.
12. H. Pasternack, *Upstream Window Failure Tests*, SALAD Progress Report, June 5, 1988, unpublished.
13. L.G. Greeniaus, computer code *LOSSPROG* (University of Alberta, Edmonton Alberta. , 1987).
14. Data published by the Bicron Corporation. 12345 Kinsman Road Newbury, Ohio. 44065. European Office, P.O. Box 271 2410 AG Bodegraven The Netherlands.
15. C. Oram et al. *Nuclear Instruments and Methods* **179** (1981) 95.
16. L.G. Greeniaus, computer code *PERSEUS* (University of Alberta, Edmonton Alberta. , 1987).
17. L. Lyons, *Statistics for Nuclear and Particle Physists,* Cambridge University Press, New York, 1986.
18. C.R. Hurlbut, *Plastic Scintillators - A Survey,* Paper Presented at the American Nuclear Society Winter Meeting. November, 1985.
19. G. F. Knoll, *Radiation Detection and Measurement,* John Wiley & Sons Inc., Toronto, 1979.

20. R. A. Arndt et al. *Physical Review* D **35** (1987) 128.

21. K. Negm : Thesis, University of Alberta (1988), unpublished.

22. 210 MeV data from - A. Konradi : Thesis, University of Rochester (1961).

23. 213 MeV data from - J. F. Marshall et al., *Physical Review* **150** (1966) 1119.

24. Price, W. J. *Nuclear Radiation Detection*, 2nd ed. McGraw-Hill Series in Nuclear Engineering. McGraw-Hill Book Co., Toronto, 1964.

25. Wilkinson, D.H., *Ionization Chambers and Counters*, Cambridge University Press, 1950.

26. Rossi, B.B. and Staub, H.H., *Ionization Chambers and Counters*, McGraw Hill Book Co. Toronto, 1949.

27. Sauli, F., *Principles and Operation of Multiwire Proportional and Drift Chambers*, CERN Report 77-09. Geneva. May 3, 1977.

28. Knoll, G.F., *Radiation Detection and Measurement*, John Wiley & Sons Inc., Toronto, 1979.

29. Bouclier, R. et al. *Nuclear Instruments and Methods* **88** (1970) 149.

30. Brehin, S. et al. *Nuclear Instruments and Methods* **123** (1975) 225.

31. Matoba, M. *Radiation Detectors and Their Uses*, KEK Report 88-5 Japan. July (1988) 9.

32. Alekseev, N.A. et al. *Nuclear Instruments and Methods* **177** (1980) 385.

33. Barash-Schmidt, N. *Rev. Mod. Phys* **45** (1973) S15.

34. Bevington, P. R., *Data Reduction and Error Analysis for the Physical Sciences*, McGraw-Hill, New York (1969).

35. H. A. Bethe, *Ann. Physik* [7] **5** (1930) 325.

36. Greeniaus, L. G. *TRIUMF Kinematics Handbook* 2nd Ed. (1987).

37. E. Fermi, *Nuclear Physics*, University of Chicago Press, Chicago, 1950.

38. Jackson, J. D., *Classical Electrodynamics*, 2nd Ed. John Wiley & Sons Inc., Toronto, 1975.

39. J. E. Moyal, *Phil. Mag*. **46** (1955) 263.

40. Segre, E. *Nuclei and Particles*, 2nd ed. Benjamin / Cummings Publishing Company, Don Mills, Ontario, 1977.

41. Yuan, L. and Wu, C. Ed. *Methods of Experimental Physics*, Vol. 5A Academic Press, New York, 1961.

APPENDIX A.

CHARACTERISTICS OF WIRE CHAMBER DETECTORS

The various types of wire chamber detectors can be classified on the basis of *gain*. The gain is the ratio of the number of electrons collected by the anode wire (n), to the number of ion pairs produced by the incident radiation (N_0). Two major factors affect the gain. They are the *applied voltage* V between the anode wire and the cathode wall and the *gas mixture* used. First, the effects of the applied voltage on the gain will be discussed for a wire chamber of a fixed gas mixture. This will introduce the ionization chamber, proportional counter and the Geiger Müller counter modes of wire chamber operation. Then the effects of gas mixture on the gain will be discussed. This will introduce the self quenching streamer mode of wire chamber operation.

A. Effects of Applied Voltage

All classes of gas filled wire chamber detectors share features of the simple mechanical and electrical design shown schematically in figure A-1 below[(24)]. Figure A-2[(25)] shows log(n) as a function of V for the gas filled detector of figure A-1.

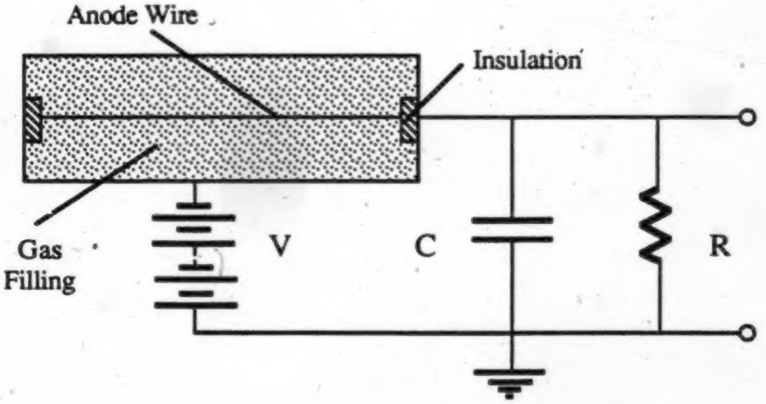

Figure A-1 Schematic Design of a Typical Gas Filled Wire Chamber Detector. (Modified from W. J. Price, Nuclear Radiation Detection, 1964)

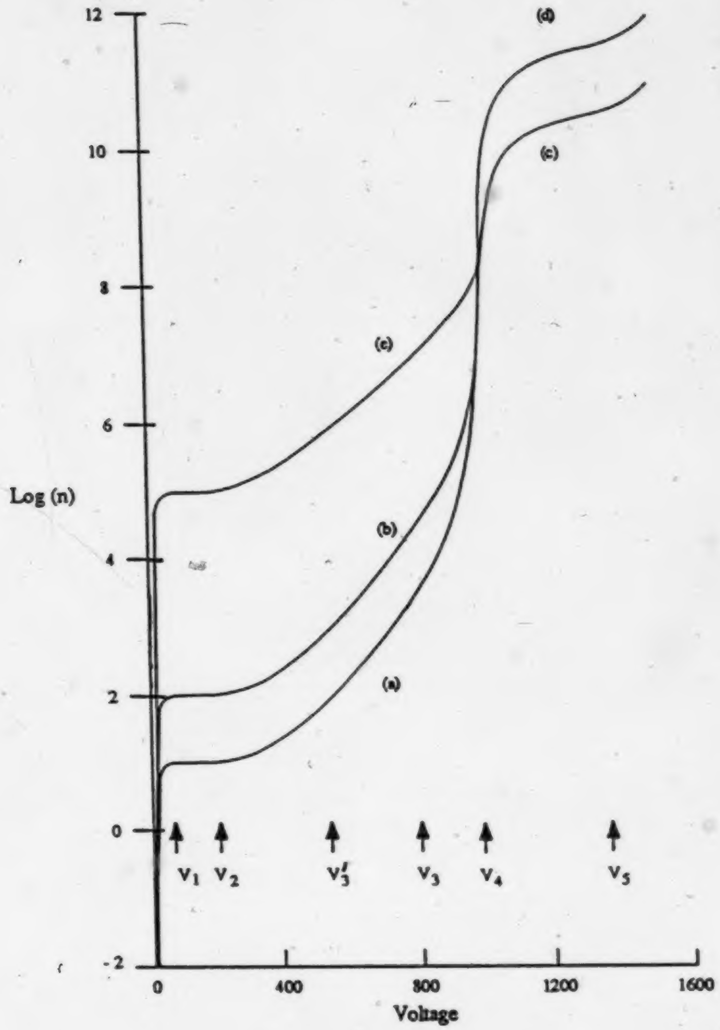

Figure A-2 Log(n) as a Function of Applied Voltage for the Gas Filled Detector of Figure A-1. (Modified from D. H. Wilkinson, Ionization Chambers and Counters, 1950)

Curve (a) corresponds to 10 electrons initially liberated and curve (b) corresponds to 100. Below a certain small voltage V_1 all the electrons initially liberated do not reach the anode wire. The three major processes which prevent the free electrons from being collected are:

a. Diffusion - electrons thermally diffuse out of the *active volume* (the volume from which ionization is collected as defined by the shape of the electric field).

b. Attachment - electrons becoming attached to a neutral gas molecule.

c. Recombination - electrons recombining with a positive ion.

The details of these mechanisms can be found in many books on gas filled detectors(24,25,26). As the voltage is increased to V_1 these processes become negligible and essentially all N_0 electrons reach the central anode. At this point *saturation* is said to occur. The number of electrons collected remains equal to the number produced by primary ionization until V is increased to V_2. This range of operating voltage between V_1 and V_2 defines the ionization chamber.

As the highly mobile free electrons accelerate towards the anode (typically moving 5 mm in ~ 1 ns(27)) they undergo many collisions with neutral gas molecules. At V_2 the electrons gain enough energy in a mean free path, typically a few µm, to cause ionization (one mean free path being the average distance traveled between collisions). The newly liberated secondary electrons are also accelerated by the electric field and can cause more ionization. This gas multiplication or avalanche begins a few radii from the anode wire and terminates when all the free electrons reach the anode. The collected charge is proportional to N_0 as shown in figure A-2 between V_2 and V_3 since the 100 initial electrons always give 10 times more final electrons than do the 10 initial electrons and so curves (a) and (b) are 1 unit apart on the log(n) scale. This range of operating voltage between V_2 and V_3 defines the proportional counter.

For voltages above V_3 non-linear effects come into play due to the large number of positive ions created in the avalanche process. The drift velocity of the free electrons is typically 10^3 times greater than that of the massive positive ions. By the time the electrons are collected at the anode the positive ions have moved negligibly. The cloud of positive ions (half of which are created in the last electron mean free path) is large enough to distort the electric field near the anode wire and gas multiplication is inhibited. The electron gain begins to drop off so that the proportionality of the electron yield to the initial ionization is broken. The higher the initial ionization the sooner the positive space charge becomes important. If 10^5 ion pairs are initially formed as indicated in figure A-2 by curve (e), then curves (b) and (e) are three units apart but only between V_2 and V_3'. Hence V_3 is a function of the initial ionization. As V approaches V_4 the number of electrons collected is no longer proportional to N_0 but it is still true that the greater number of initial electrons gives the greater number of collected electrons. When the applied voltage reaches V_4 the positive space charge is large enough to stop further gas multiplication. Regardless of the initial number of ion pairs, the number of electrons collected is the maximum number of electrons that can be produced in a single avalanche. This range of operating voltage between V_3 and V_4 defines the region of limited proportionality.

In the avalanche process, collisions between electrons and neutral gas molecules result in both ionization and excitation. The excited molecules return quickly to their ground state with the release of photons(28). The energy of the photons depends on how highly excited the gas molecules are. This in turn depends on how energetic the colliding electrons are which depends on the applied voltage. Above V4 the photons released by the excited gas molecules have energies corresponding to the ultraviolet region (5 - 50 eV). When these UV photons interact with gas molecules or with the cathode wall, photoelectrons can be released. These free electrons can go on to trigger other avalanches which in turn generate more UV photons. Rapidly the entire anode wire is enveloped by the UV photon propagated discharge. As can be seen in figure A–2 the number of electrons collected above V_4 is restricted only by the size of the chamber. Curve (d) is produced under conditions identical to curves (a) and (b) except that the chamber in figure A-1 is 10 times longer. Curves (a) and (b) again join but this time giving curve (d) which is one unit higher than cuive (c). When the applied voltage reaches V_5 the chamber will discharge even if no radiation is incident (this is referred to as *breakdown*). This range of operating voltage between V_4 and V_5 defines the Geiger–Müller mode.

The gain which can be obtained in the Geiger - Müller mode is limited by the large positive ion space charge that develops around the anode. The electric field strength in the whole counter is quickly reduced below that needed for gas multiplication. The electric field recovers slowly as the space charge diffuses away from the anode toward the cathode. During this *dead time* (typically several hundred μsec) no further radiation detection is possible.

B. Effects of Gas Mixture

Both monoatomic and polyatomic gases are used in gas filled detectors. Monoatomic, or noble, gases include He, Ne, Ar, and Kr. Polyatomic gases are of the organic type - hydrocarbons and alcohols, and the inorganic type - freons, CO_2, BF_3

for example. Experimental requirements such as gain, rate capabilities, dead time, energy and position resolution determine the type of gas or mixture of gases to be used. The influence of the gas mixture on these parameters is outlined below.

Gas multiplication begins at much lower voltages for noble gases than for polyatomic gases which have many rotational and vibrational (i.e. non-ionizing) energy dissipation modes. When low operating voltage is desirable, noble gases are often used. High specific ionization and relatively low cost favor the use of argon (29.4 primary ion pairs per cm for minimum ionizing particles at atmospheric pressure(24,27)). It is generally necessary to use a noble gas in a mixture with other gases for the following reasons. In a pure noble gas, the positive monoatomic ions are neutralized only when they reach the cathode wall. If their ionization potential is greater than but not twice the work function of the cathode, a single cathode electron will be liberated. The now neutral monoatomic molecule is often excited and can radiate a UV photon which may go on to initiate a new or secondary avalanche. If the ionization potential is greater than twice the work function of the cathode it is possible for two cathode electrons to be liberated. One electron neutralizes the positive ion and the other electron is free to initiate a secondary avalanche.

In proportional counters the processes described above can limit the operating voltage range and hence the gain. Geiger counters operated with pure noble gases become unstable due to the large number of positive ions reaching the cathode. To limit the formation of secondary avalanches, it is necessary to *quench* the processes leading to secondary avalanche formation.

Quenching can be done *externally*(24) by reducing the high voltage for a period of time after the initial pulse determined by the positive ion drift time between their point of formation and the cathode. Typically this is on the order of 100μs limiting the usefulness of this method to low count rate situations. More commonly the quenching is done *internally*(27,28) by adding a small proportion (5% - 10%) of a polyatomic gas. The quenching action of the polyatomic gas is twofold:

i. The positive ions formed by the incident radiation are primarily of the monoatomic component. As they drift to the cathode wall there is a high probability that they will collide with a neutral polyatomic gas molecule. Since the latter has a lower ionization potential than the former an electron will be transferred from one to the other. The monoatomic molecule is neutralized and the now positive polyatomic molecule drifts toward the cathode. Unlike the noble gas molecule there is a very low probability of secondary electron emission when the polyatomic ion reaches the cathode because any energy excess between the liberated cathode electron and the energy needed to fill the ionized state goes into a non-ionizing rotational or vibrational energy mode. It is also unlikely that a UV photon will be released as the energy modes of the polyatomic molecules are highly non-radiative. The build-up of vibrational and rotational energy eventually causes the polyatomic molecule to dissociate into smaller radicals. By preventing the monoatomic ion from reaching the cathode the probability of a secondary avalanche is significantly reduced.

ii. Polyatomic gas molecules have a high cross section for photon absorption. Should a monoatomic ion reach the cathode with the emission of a UV photon a polyatomic molecule can absorb the photon energy and again prevent a secondary avalanche. The photon-quenching efficiency increases with the number of atoms in the molecule. Isobutane (C_4H_{10}) is often used as a quenching agent for stable operation at high gain.

Many polyatomic gases are electronegative (freons such as CF_3Br or ethyl-bromide C_2H_5Br for example). Should a free electron be liberated from the cathode the electronegative molecule can capture it before a secondary avalanche results. In proportional chamber mode gains as high as 10^7 are possible with the use of electro-negative gases.

Experimentation with various gas mixtures has led to the discovery of the *self quenching streamer* (SQS) mode of wire chamber operation.(29) Using a 'magic' gas mixture of argon, isobutane and freon in the volume proportion 70.0 - 29.6 - 0.4 gains as high as 10^8 were observed with 100% efficiency without entering the Geiger counter mode. Further investigation showed similar results with a typical argon - isobutane gas mixture but with large diameter anode wires (>40μm)(30). The SQS mode was originally believed to be a transitional mode between the proportional and Geiger modes of operation. However, the large width of the counting rate plateau (>1000V) and the constant values of pulse duration (~40ns at half maximum) and *dead zone* (~300 μs x cm) over this plateau show the SQS mode is separate and distinct from all other modes. The term 'dead time' is not applicable to the SQS mode as unlike the Geiger - Müller

(GM) discharge the SQS discharge does not envelope the entire anode wire. Thus it is more useful to define a 'dead zone' which is the product of the length of anode wire involved in the discharge (~ 10 mm) and the dead time of that length (~300 μs).

The exact mechanism of the SQS discharge is not well understood(31). Photographs reveal that the discharge is initiated by the initial electron avalanche near the anode wire. Then an intense streamer develops propagating toward the cathode in a direction defined by the original electron drift. Unlike the GM discharge, there is only a small region of photon propagation along the anode wire. The high concentration of polyatomic gas somehow prevents the photoionization process from propagating beyond a confined region.

There are many interesting and useful aspects of the SQS mode of wire chamber operation(32). Here are some that pertain specifically to the SALAD detector:

- The gain from gas multiplication is very high (~10^8). This reduces the need for high amplifier gain, gives a very good signal to noise ratio, and allows stable operating thresholds.
- The SQS discharge is easily obtained using a thick anode wire (50 - 100μm diameter) making the construction of large SQS chambers feasible.
- The SQS streamer is localized to a small region along the anode wire. Using a charge division readout, position information can be obtained with a resolution on the order of a few millimeters.
- Although a small part of the anode wire in the region of the SQS discharge has a large dead time, the rest of the anode remains fully sensitive to passing radiation.
- The amplitude of SQS signals are very nearly independent of the primary ionization. Thus the SALAD wire chambers are equally sensitive to all types of charged γN reaction products.

The major limitation of the SQS mode is the large local dead time. A uniformly irradiated 1 m x 1 m wire chamber with 1 wire / cm would have ~ 1% loss at 10^5 counts / sec(30).

A summary of the modes of wire chamber operation as they relate to one another is shown in figure A-3(31). Although the diameter of the anode wire and the pressure of the gas have some influence, the mode of operation beyond the proportional mode is defined primarily by the gas mixture composition.

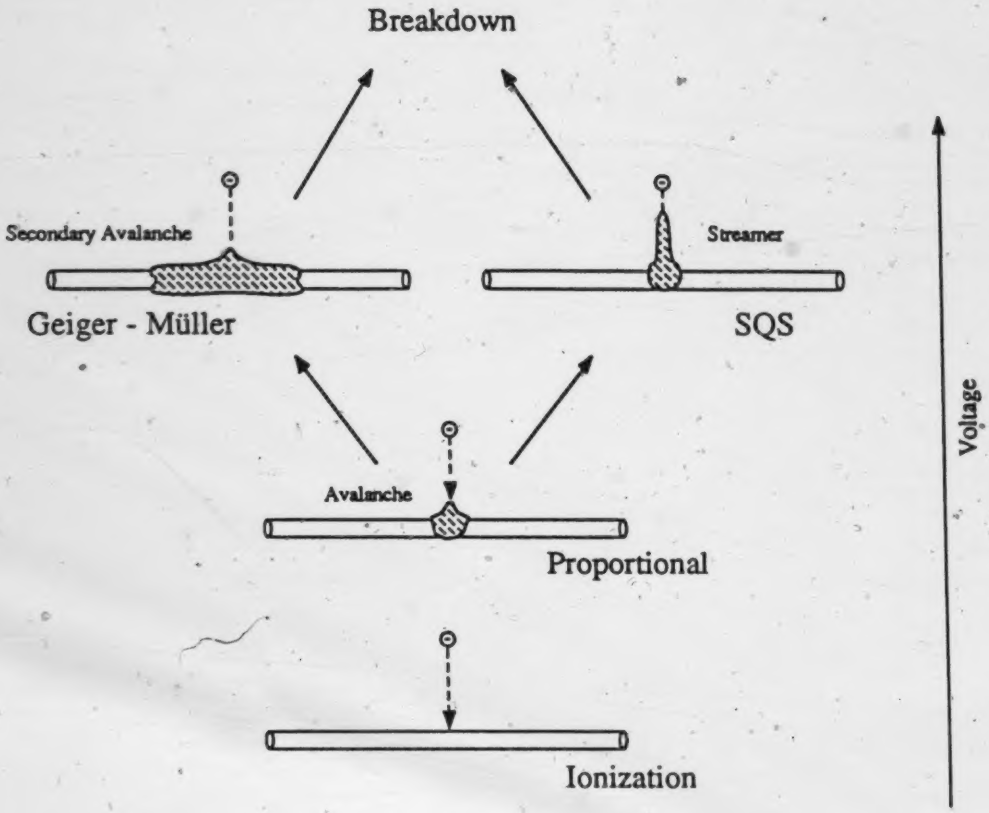

Figure A-3 A Summary of the Wire Chamber Modes of Operation.

(Modified from M. Matoba, Radiation Detectors and Their Uses, 1988)

APPENDIX B

MATHEMATICAL SUPPLEMENT

I. z Position Determination From Charge Division Readout

When an amount of charge Q is collected by an anode wire at some position (z) along its length, it splits into two parts, Q_{up} and Q_{dn}, which are collected at the upstream and downstream ends of the wire respectively. The calculated z position where Q is collected is proportional to $\mathbb{R}$, the difference in charge collected by the downstream and upstream ends of the anode wire normalized with respect to the total charge collected

$$z \propto \mathbb{R} = \frac{Q_{difference}}{Q_{sum}} = \frac{Q_{dn} - Q_{up}}{Q_{dn} + Q_{up}} \quad . \qquad \text{(B.1)}$$

The relative sizes of Q_{up} and Q_{dn} depend on (a) the impedance Z of the electronics at the ends of the wire, and (b) the resistances, R_{up} and R_{dn}, of the wire between the point where Q is collected and the upstream and downstream ends. The resistance per unit length of the 50 μm stainless steel anode wires is 5.3 Ω / cm. Thus R_{up} and R_{dn} are proportional to the length of wire between the point where Q is collected and the upstream and downstream ends of the wire.

For example, if Z is 10 kΩ at each end (as it is on the collector side of the NPN transistor), and if Q is deposited at a point along the wire such that R_{up} and R_{dn} are 118 Ω and 518 Ω respectively, then Q is divided into two portions in the ratio

$$\frac{Q_{up}}{Q_{dn}} = \frac{R_{up} + Z}{R_{dn} + Z} = \frac{10118\,\Omega}{10518\,\Omega} \quad .$$

If the values of Q_{up} and Q_{dn} have an error of 1%, the values of $\mathbb{R}$ are

$$-0.03 \pm 32\% \leq \mathbb{R} \leq 0.03 \pm 32\% \quad .$$

If Z is 82 Ω at each end, (as it is on the emitter side of the NPN transistor) and Q is deposited at the same position then

$$\frac{Q_{up}}{Q_{dn}} = \frac{200\,\Omega}{600\,\Omega} \quad .$$

With a 1% error in the values of Q_{up} and Q_{dn}, the values of $\mathbb{R}$ are

$$-0.80 \pm 0.46\% \leq \mathbb{R} \leq 0.80 \pm 0.46\% \quad .$$

The accuracy with which z can be determined depends on the error in $\mathbb{R}$. The above calculations show that the smaller the value of Z the smaller the error in $\mathbb{R}$ and hence the smaller the error in z.

Written in terms of ADC values $\mathbb{R}$ is given by

$$\mathbb{R} = \left[\frac{ADC_{dn} - ADC_{up}}{ADC_{dn} + ADC_{up}}\right] . \qquad \text{(B.2)}$$

Ideally, if an event takes place at the very upstream end of the wire then no charge is collected at the downstream end and $ADC_{dn} = 0$ (after pedestal subtraction). If an event takes place at the very downstream end of the wire then no charge is collected at the upstream end and $ADC_{up} = 0$ (after pedestal subtraction). Thus, ideally $\mathbb{R}$ obeys

$$-1.0 \leq \mathbb{R} \leq 1.0$$

Multiplying $\mathbb{R}$ by half of the length of the wire would yield the position along the wire where Q was collected such that z = 0 corresponds to the center of the wire.

The pedestals and gains of the upstream and downstream electronics are nearly but not exactly identical. Thus $\mathbb{R}$ does not lie exactly between -1.0 and 1.0, and a result of $ADC_{up} = ADC_{dn}$ does not necessarily correspond to z = 0. However, because of the linearity of the system we can write

$$z = \mathbb{R} * L + L_o \quad , \qquad \text{(B.3)}$$

where L is the effective half length of the wire, and L_o is the offset which ensures that z = 0 when the event occurs at the center of the wire even if $ADC_{up} \neq ADC_{dn}$.

II. Flight Time Through the M13 π Channel and π Decay Kinematics

The velocity (v) and momentum (p) of a pion are related by

$$p_\pi = \gamma_\pi m_\pi v_\pi \ ,$$

where m_π is the rest mass of the pion (m_π = 139.57 Mev / c^2)(33) and γ_π is the relativistic factor given by

$$\gamma_\pi = \frac{1}{\sqrt{1 - \left(\frac{v_\pi}{c}\right)^2}} \ .$$

The above equations can be rearranged to give

$$\frac{v_\pi}{c} = \sqrt{\frac{p_\pi^2}{p_\pi^2 + m_\pi^2}} \ .$$

The velocity and momentum of the pions through the M13 channel are given in table 3-1.

Since the momenta of the pions and muons are the same in a given TRF spectrum (figure 3-5), the velocity of the muons can be calculated as above. Muons of momenta 77.8 MeV/c, 104.7 MeV/c, 127.1 MeV/c, and 145.8 MeV/c have velocities of 0.59c, 0.70c, 0.77c and 0.81c respectively. Assuming the pions and muons originate at the 1AT1 pion production target, the time of flight of the pions (t_π) and muons (t_μ) through the M13 channel is given simply by

$$t_\pi = \frac{d}{v_\pi} \quad \text{and} \quad t_\mu = \frac{d}{v_\mu} \ ,$$

where d is the length of the M13 channel in the lab frame (9.2 m). The difference in time of flight (T) is given by

$$T = t_\pi - t_\mu = d\left(\frac{1}{v_\pi} - \frac{1}{v_\mu}\right) = d\left(\frac{v_\mu - v_\pi}{v_\pi v_\mu}\right) \ .$$

Using the muon velocities above and the pion velocities given in table 3-1, the difference in time of flight of the muons and pions of momenta 77.8 MeV/c, 104.7 MeV/c, 127.1 MeV/c, and 145.8 MeV/c are 10.6 ns, 7.31 ns, 5.9 ns and 4.7 ns respectively. These values are observed in the TRF spectra of figure 3-5.

Positively charged pions decay predominantly via the process $\pi^+ \rightarrow \mu^+ + \nu_\mu$. With the pion decaying at rest, what are the kinetic energies of the muon and neutrino? In the lab frame, conservation of energy gives the relation

$$E_\pi = E_\mu + E_\nu$$

where the total energy of a particle is given relativistically by

$$E = T + E_o \qquad (B.4)$$

where T is the kinetic energy and $E_o = m_o c^2$ is the rest mass energy of the particle. Since $T_\pi = 0$ and the rest mass of the neutrino is $m_\nu = 0$

$$m_\pi c^2 = T_\mu + m_\mu c^2 + T_\nu$$

or rearranging

$$T_\nu = m_\pi c^2 - m_\nu c^2 + T_\mu \,. \qquad (B.5)$$

Conservation of momentum gives the relation

$$p_\pi = p_\mu + p_\nu \,.$$

With the pion at rest in the lab, $p_\pi = 0$ so

$$p_\mu c = -p_\nu c \,. \qquad (B.6)$$

The total energy E of a particle is related to its momentum by

$$E^2 = p^2c^2 + m_o^2c^4 \,. \qquad (B.7)$$

Using (B.4), the massless neutrino obeys the simple relation

$$E_\nu = p_\nu c = T_\nu \,.$$

From (B.6), this gives

$$T_\nu = - p_\mu c\,. \tag{B.8}$$

Squaring (B.4) and equating the result to (B.7) gives the relation between a particles momentum and kinetic energy

$$p^2c^2 = T^2 + 2Tm_oc^2\,. \tag{B.9}$$

To find an expression for the kinetic energy of the muon we square (B.5)

$$T_\nu^2 = m_\pi^2c^4 + m_\mu^2c^4 - 2m_\pi m_\mu c^4 - 2T_\mu m_\pi c^2 + T_\mu^2 + 2T_\mu m_\mu c^2\,.$$

From (B.9) the last two terms in this equation sum to give $p_\mu{}^2c^2$ which from (B.8) is equal to $T_\nu{}^2$. So the above equation becomes

$$m_\pi^2c^4 + m_\mu^2c^4 - 2m_\pi m_\mu c^4 - 2T_\mu m_\pi c^2 = 0\,.$$

Solving for T_μ gives

$$T_\mu = \frac{m_\pi^2c^4 + m_\mu^2c^4 - 2m_\pi m_\mu c^4}{2m_\pi c^2}\,.$$

Placing this into (B.5) gives a relation for the kinetic energy of the neutrino

$$T_\nu = \frac{m_\pi^2c^4 - m_\mu^2c^4}{2m_\pi c^2}\,.$$

The mass of the pion is $m_\pi = 139.57$ MeV/c^2 and the mass of the muon is $m_\mu = 105.66$ MeV / c^2(33). Using these values we find that a positive pion decaying at rest via $\pi^+ \rightarrow \mu^+ + \nu_\mu$ gives a muon of kinetic energy $T_\mu = 4.1$ MeV and a neutrino of energy $T_\nu = 29.8$ MeV.

III. Linear Regression Formulas

Many linear fits are performed throughout this thesis. When fitting the data points (x_1, y_1), (x_2, y_2), . . . ,(x_N, y_N) to a straight line of the form $y = Ax + B$, the following linear regression equations are used(34)

$$A = \frac{N\sum_{i=1}^{N} x_i\, y_i \;-\; \sum_{i=1}^{N} x_i \sum_{i=1}^{N} y_i}{N\sum_{i=1}^{N} x_i^2 \;-\; \left(\sum_{i=1}^{N} x_i\right)^2} \;, \qquad \text{(B.10)}$$

and

$$B = \frac{\sum_{i=1}^{N} y_i \sum_{i=1}^{N} x_i^2 \;-\; \sum_{i=1}^{N} x_i \sum_{i=1}^{N} x_i\, y_i}{N\sum_{I=1}^{N} x_i^2 \;-\; \left(\sum_{i=1}^{N} x_i\right)^2} \;. \qquad \text{(B.11)}$$

The correlation coefficient of the data (r) is calculated using

$$r = \frac{N\sum_{i=1}^{N} x_i\, y_i \;-\; \sum_{i=1}^{N} x_i \sum_{i=1}^{N} y_i}{\left[N\sum_{i=1}^{N} x_i^2 \;-\; \left(\sum_{i=1}^{N} x_i\right)^2\right]^{1/2} \left[N\sum_{i=1}^{N} y_i^2 \;-\; \left(\sum_{i=1}^{N} y_i\right)^2\right]^{1/2}} \;. \qquad \text{(B.12)}$$

IV. Order of Peaks in 20.2 MeV Beam Scintillator Spectrum

The energy lost by a particle of charge z and velocity v in an absorber of atomic density N, proton number Z and mean ionization energy $\hbar\langle\omega\rangle$ as derived by Bethe(35) is

$$\frac{dE}{dx} = 4\pi NZ\,\frac{z^2e^4}{m_e v^2}\left[\ln\frac{2\gamma^2 m_e v^2}{\hbar\langle\omega\rangle} - \frac{v^2}{c^2}\right] \qquad \text{(B.13)}$$

where m_e is the mass of the electron. Here the effects of close collisions are included but no density effect correction δ and no shell correction term U is included. To find whether pions or muons of the same momentum lose more energy in the beam scintillator we take the ratio

$$\frac{\left|\frac{\Delta E}{\Delta x}\right|_{\pi}}{\left|\frac{\Delta E}{\Delta x}\right|_{\mu}} = \frac{4\pi NZ \frac{z^2e^4}{m_e v_\pi^2}\left[\ln \frac{2\gamma_\pi^2 m_e v_\pi^2}{\hbar\langle\omega\rangle} - \frac{v_\pi^2}{c^2}\right]}{4\pi NZ \frac{z^2e^4}{m_e v_\mu^2}\left[\ln \frac{2\gamma_\mu^2 m_e v_\mu^2}{\hbar\langle\omega\rangle} - \frac{v_\mu^2}{c^2}\right]} \,.$$

The value of Δx is the same in each case so we can write

$$\frac{\Delta E_\pi}{\Delta E_\mu} = \frac{v_\mu^2}{v_\pi^2}\,\frac{\ln \alpha_\pi - \beta_\pi^2}{\ln \alpha_\mu - \beta_\mu^2} \tag{B.14}$$

where

$$\alpha = \frac{2\gamma^2 m_e v^2}{\hbar\langle\omega\rangle}$$

and $\beta = v / c$. The mean ionization energy $\hbar\langle\omega\rangle$ of CH_2 is given in the TRIUMF Kinematics Handbook(36) as 73.8 eV. The values of γ and β for pions of energy 20.2 MeV are given in table 3-1. The value of α_π for this energy is then $\alpha_\pi = 4299.8$. Muons of the same momentum have a velocity $v_\mu = 0.593$ c and so $\gamma_\mu = 1.242$. Together these give $\alpha_\mu = 7502.6$. These values of α and v in (B.14) give,

$$\frac{\Delta E_\pi}{\Delta E_\mu} = 1.41 > 1 \ .$$

An actual LOSSPROG(13) calculation of the energy lost by the pions and muons in the beam scintillator gives a ratio of 1.44. Therefore, for pions and muons of the same momentum we expect the pions to lose more energy in the thin beam scintillator.

V.Energy Loss Distribution in the Beam Scintillator Spectra

The average energy lost by a charged particle per unit distance in some material can be calculated from energy loss theory(35,37). This average energy lost is due to a large number of collisions primarily between the particle and the bound electrons in the material. The amount of energy lost in a single collision can vary widely. From simple arguments it can be shown that the energy transfered to an electron in a collision is given by (38)

$$E_t(b) = \frac{2\,z^2 e^4}{m_e v^2}\,\frac{1}{b^2}$$

where b is the impact parameter. The mean square energy loss per unit distance is given by

$$\frac{dE^2}{dx} = 2\pi NZ \int_{b_{min}}^{b_{max}} \left[E_t(b)\right]^2 b\,db\ .$$

Provided the minimum impact paramater b_{min} is much less than the maximum impact parameter b_{max} this becomes

$$\frac{dE^2}{dx} = 4\pi NZ \frac{z^2 e^4}{m_e v^2}\left[\gamma^2 m_e v^2 \left(1 - \tfrac{1}{2}\beta^2\right)\right]\ . \qquad \text{(B.15)}$$

The term $-{}^{1}/_{2}\beta^2$ is added by hand to make the expression correct relativistically. The energy loss is a statistical process resulting in a distribution of energy lost about the average. For most circumstances this distribution is Poisson. However, the energy loss distribution becomes Gaussian for the case $\sigma \ll E_{av}$ where σ^2 is the mean square deviation in energy loss which is given by

$$\sigma^2 = x\,\frac{dE^2}{dx}$$

and E_{av} is the average energy of the particle as it exits the material of thickness x. The energy loss distribution also becomes Gaussian if $\sigma \gg \Delta E_{max}$ where $\Delta E_{max} \cong 2\gamma^2 m v^2$ is the maximum energy that can be lost by the passing particle in a single collision. To test the latter condition we form the ratio

$$\frac{\sigma^2}{\Delta E_{max}^2} = \frac{4\pi NZx \frac{z^2e^4}{m_e v^2} \gamma^2 m_e v^2 \left(1 - \frac{1}{2}\beta^2\right)}{\left(2\gamma^2 m_e v^2\right)^2} ,$$

or

$$\frac{\sigma}{\Delta E_{max}} = \left[\pi NZx \frac{z^2 e^4}{m_e^2 c^4} \frac{\left(1 - \frac{1}{2}\beta^2\right)}{\beta^4 \gamma^2} \right]^{1/2} . \qquad \text{(B.16)}$$

For CH_2 of density $\rho = 1.032$ g/cm^3 and $Z = 8$, then $N = 4.43 \times 10^{22}$/cm^3. With $e^2 = 1.44 \times 10^{-7}$ eV·cm, $m_ec^2 = 0.511 \times 10^6$ eV and x measured in cm this expression reduces to

$$\frac{\sigma}{\Delta E_{max}} \cong (0.1x)^{1/2} \frac{\left(1 - \frac{1}{2}\beta^2\right)^{1/2}}{\beta^2 \gamma} \qquad \text{(B.17)}$$

for particles with $z = 1$. If the passing particles are pions of kinetic energy 20.2 MeV, then $v_\pi = 0.487$ c and $\gamma_\pi = 1.145$. The thickness of the beam scintillator is 0.3175 cm. Hence for this case

$$\frac{\sigma}{\Delta E_{max}} \cong 0.6 < 1.$$

In order for the energy distribution to be Gaussian this ratio must be » 1. Equation (B.17) indicates that the pions would need a lower velocity (a lower kinetic energy) or the beam scintillator would need to be thicker in order to expect a Gaussian distribution.

The energy distribution typically observed in a thin scintillator is a Landau distribution which is described by(39)

$$f(\lambda) = \frac{1}{\sqrt{2\pi}} e^{-\frac{1}{2}(\lambda + e^{-\lambda})} .$$

The parameter

$$\lambda = \frac{(\Delta E - E_{mp})}{\Delta E_{ave}} ,$$

is the normalized deviation from the most probable energy loss E_{mp}, ΔE is the actual energy lost and ΔE_{ave} is the average energy loss given by

$$\Delta E_{ave} = 4\pi NZ \frac{z^2 e^4}{m_e v^2} x$$

The distinguishing features of the Landau distribution are its large width as compared to the predicted Gaussian width and its extended tail towards high energies.

VI. Position Independent ADC Values

When a particle stops in a scintillator an initial number N_o of photons are emitted in proportion to the kinetic energy of the particle. The number of photons collected depends on N_o and on the attenuation and light collection properties of the scintillator (as outlined in many text books(40)). For example, if a particle stops in a SALAD E scintillator a distance A from the left end and a distance B from the right end as shown in figure B-1, then the ADC values recorded for the left and right ends are given by

$$ADC_{Left} = \gamma N_o e^{-\mu A} \qquad \text{and} \qquad ADC_{Right} = \beta N_o e^{-\mu B}$$

where μ is the light attenuation coefficient, and γ and β are factors that depend on the light collection efficiency of the ends of the scintillator and on the external electronics which includes the photomultiplier tubes and analog to digital converters. Note that the ADC values are position dependent. When $A = B$ and $\gamma = \beta$, as they are in the pion tests, then $ADC_L = ADC_R$.

The quantity most directly related to the particle energy is N_o. To best calibrate the kinetic energy of the stopped particle with the measured ADC values, a position independent quantity that depends directly on N_o must be derived. Such a quantity can be found by taking the square root of the product of the left and right ADC values,

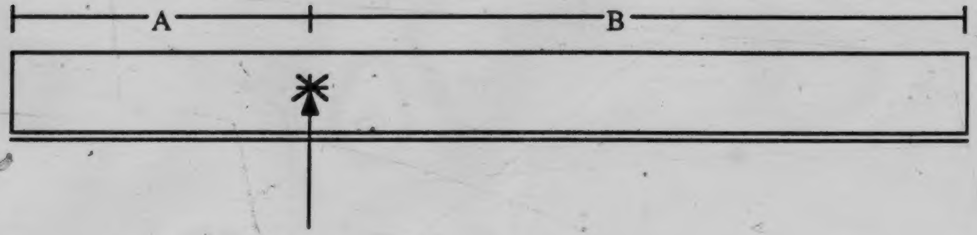

Figure B-1
A Particle Stopping in the SALAD E Scintillator at Some Arbitrary Position

$$\sqrt{ADC_{Left} * ADC_{Right}} = \sqrt{\gamma \beta N_o^2 e^{-\mu A} * e^{-\mu B}} = N_o \sqrt{\gamma \beta e^{-\mu(A+B)}} \ ,$$

or since A + B = L the length of the scintillator,

$$\sqrt{ADC_{Left} * ADC_{Right}} = N_o \sqrt{\gamma \beta} \ e^{-\mu L/2} \ . \qquad (B.18)$$

This quantity depends directly on N_o as the exponential factor is just a constant. It is also position independent assuming that γ and β are position independent.

VII. $1/\sqrt{E}$ Dependence of the Scintillator Energy Resolution.

When a particle of kinetic energy E comes to rest in a scintillator a number N_1 of scintillation photons are produced. When a second particle of energy E comes to rest a number N_2 of photons is produced. After n particles have come to rest an average number of photons $\overline{N} \pm \sigma_{\overline{N}}$ have been produced in each scintillation process where

$$\overline{N} = \frac{1}{n} \sum_{i=1}^{n} N_i$$

and $\sigma_{\overline{N}}$ is the standard error of the mean. $\sigma_{\overline{N}}$ is given by

$$\sigma_{\overline{N}} = \frac{\sigma}{\sqrt{n}}$$

where σ is the standard deviation of N where

$$N = N_1 + N_2 + \cdots + N_n = n\,\overline{N}\,.$$

Because the scintillation process in a thick scintillator follows a Poisson distribution, the standard deviation of N is $\sqrt{N}$. Thus,

$$\sigma_{\overline{N}} = \frac{\sigma}{\sqrt{n}} = \frac{\sqrt{N}}{\sqrt{n}} = \frac{\sqrt{n\overline{N}}}{\sqrt{n}} = \sqrt{\overline{N}}\,.$$

Therefore the average number of photons produced when a particle of energy E stops in a scintillator is $\overline{N} \pm \sqrt{\overline{N}}$.

Since the average number of photons produced is proportional to E, we can say that the energy measured by an apparatus which utilizes a thick scintillator is $E \pm \sqrt{E}$. The energy resolution of the apparatus is conventionally defined as the Full Width at Half Maximum (FWHM) of the energy distribution divided by the centroid of the distribution. If the energy is normally distributed then the FWHM is related to the standard deviation by FWHM ≈ 2.35 σ(24). That is, the energy resolution is proportional to

$$\text{Energy Resolution} \propto \frac{\sqrt{E}}{E} = \frac{1}{\sqrt{E}}\,.$$

The energy distribution is expected to be normal or very nearly normal because the energy distribution is proportional to the distribution of $\overline{N}$. From basic statistical theory we know that even though the parent population of N_i is Poisson distributed, the distribution of mean values $\overline{N}$ tends to be more nearly normal(41).

APPENDIX C

MONTE CARLO RESULTS

The following is a collection of Monte Carlo results. Where possible, the corresponding results for the p–p data set are also shown. The information shown in each plot is explaned the title.

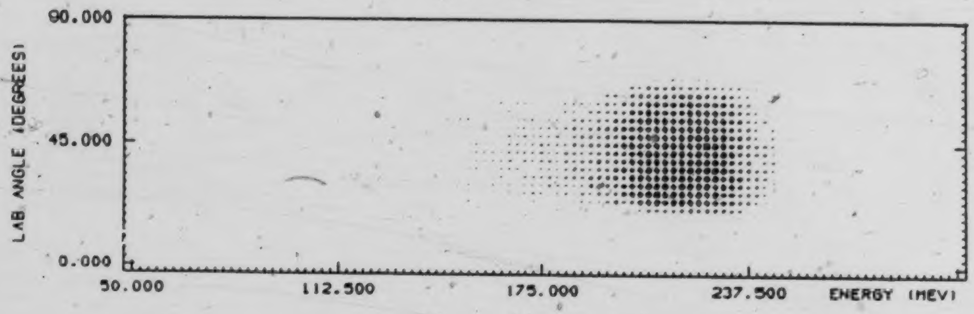
(a) p-p Data Set

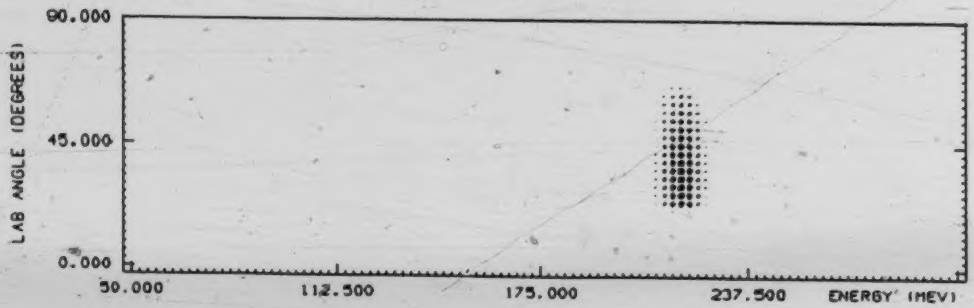
(b) Monte Carlo Data Set

Figure C-1 Scattering Angle θ_{Lab} Versus Reconstructed Beam Energy for the (a) p-p and (b) Monte Carlo Data Sets.

(a) p-p Data Set

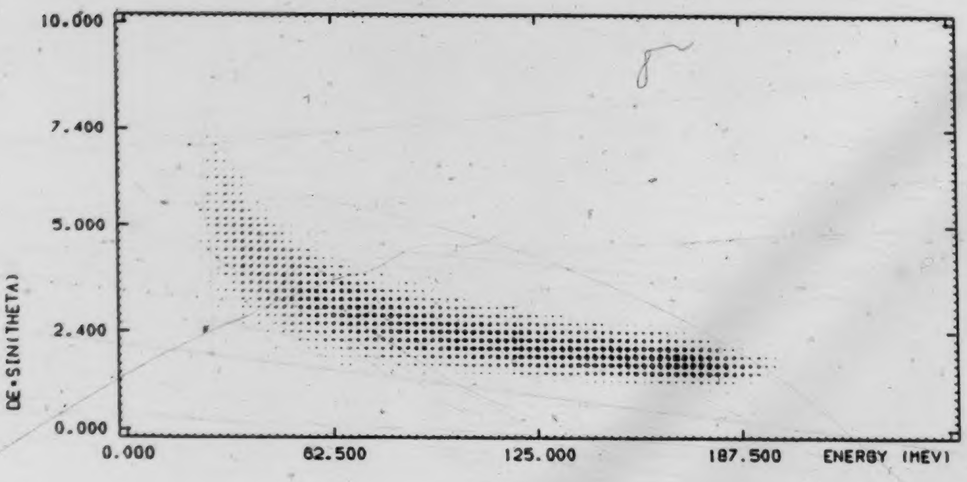

(b) Monte Carlo Data Set

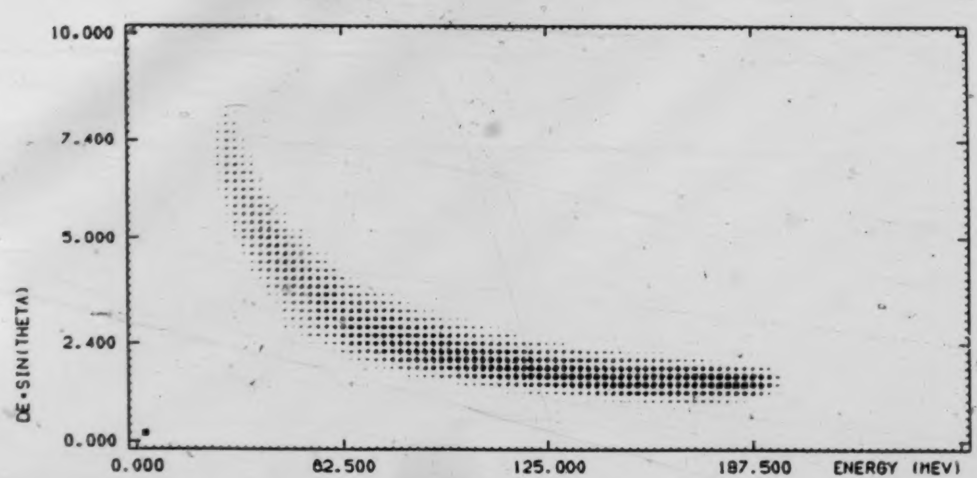

Figure C-2 Stopping Power Versus Energy Deposited in E Scintillator for the (a) p-p and (b) Monte Carlo Data Sets.

(a) Error in Theta (Monte Carlo)

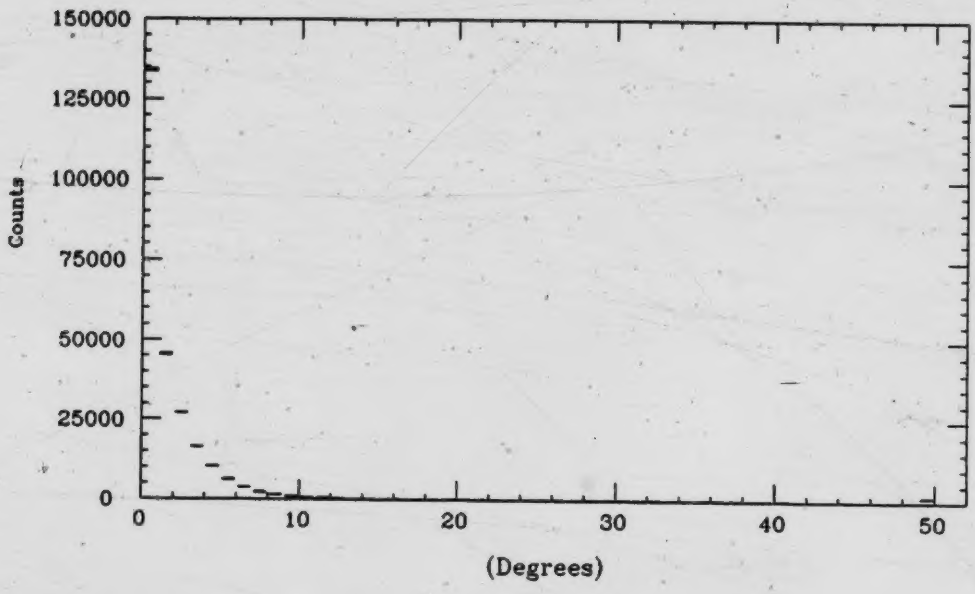

(b) Error in Phi (Monte Carlo)

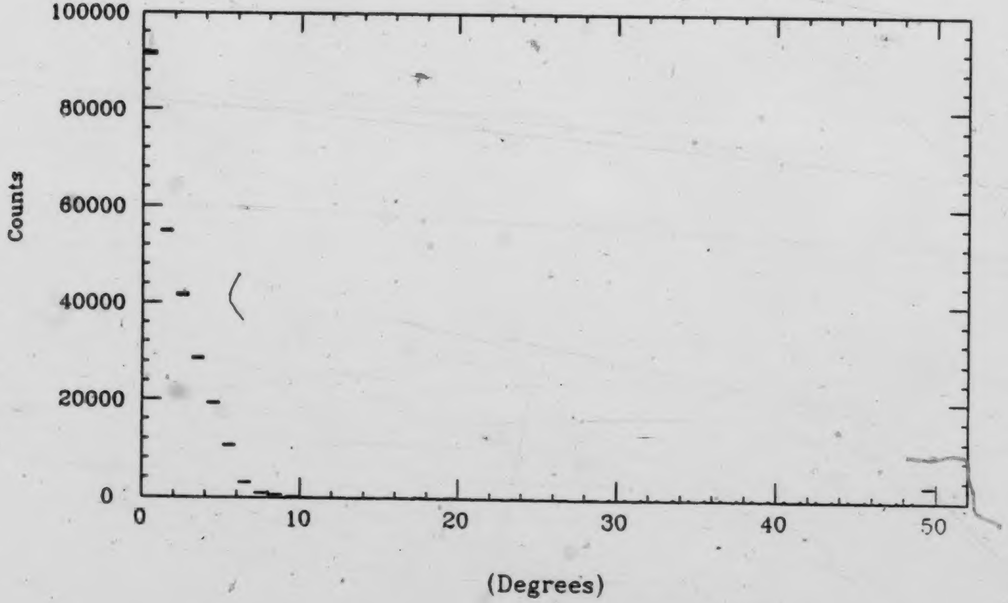

Figure C-3 Difference Between the (a) Theta and (b) Phi Angles as Generated by the Monte Carlo and Calculated by the Track Reconstruction Software.

(a) Error in Vertex (Monte Carlo)

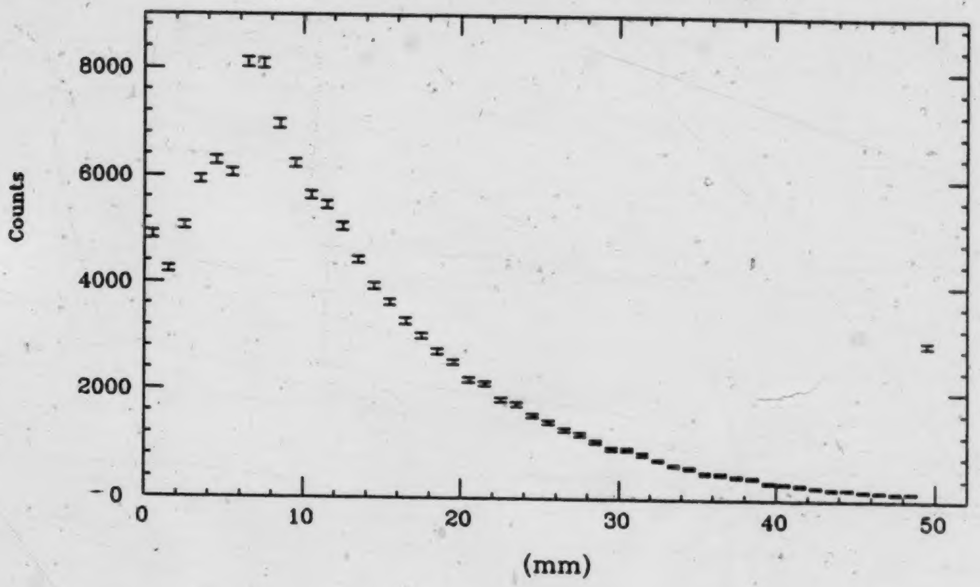

(b) Error in X-Coord of Vertex (Monte Carlo)

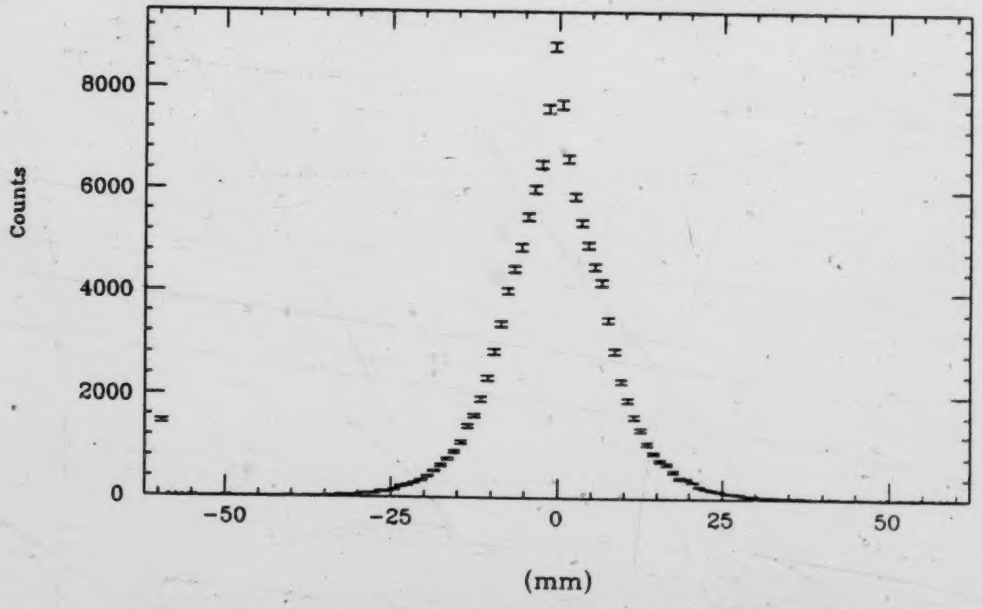

Figure C-4 Difference Between the (a) Radial Vertex Position and (b) X-Coordinate of the Radial Vertex Position as Generated by the Monte Carlo and Calculated by the Track Reconstruction Code.

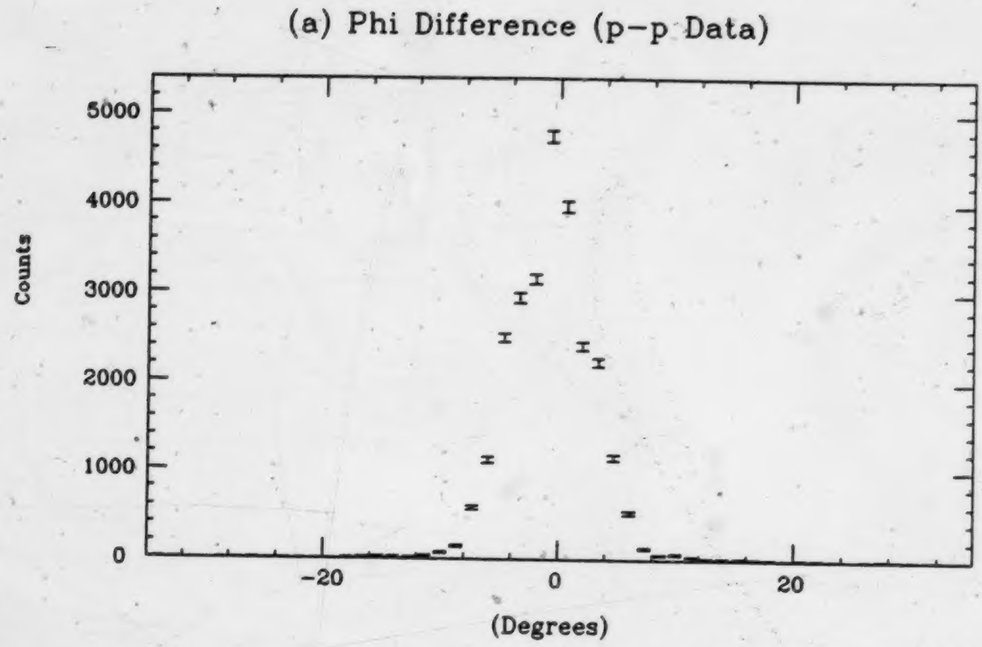

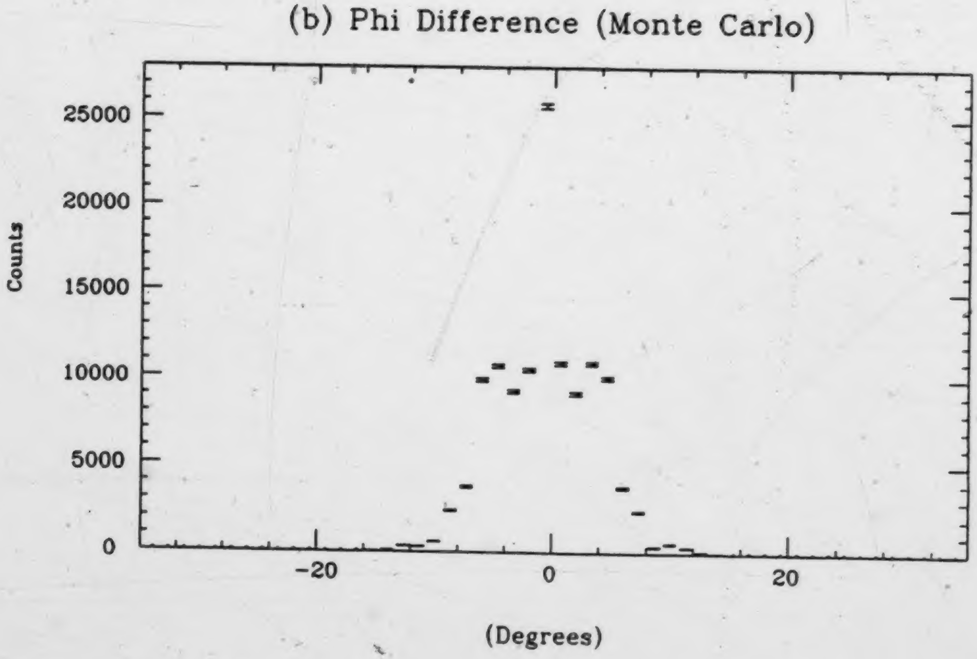

Figure C-5 $|\phi_1 - \phi_2| - 180^{\circ}$ for the (a) p-p and (b) Monte Carlo Data Sets.

(a) Opening Angle Error (p−p Data)

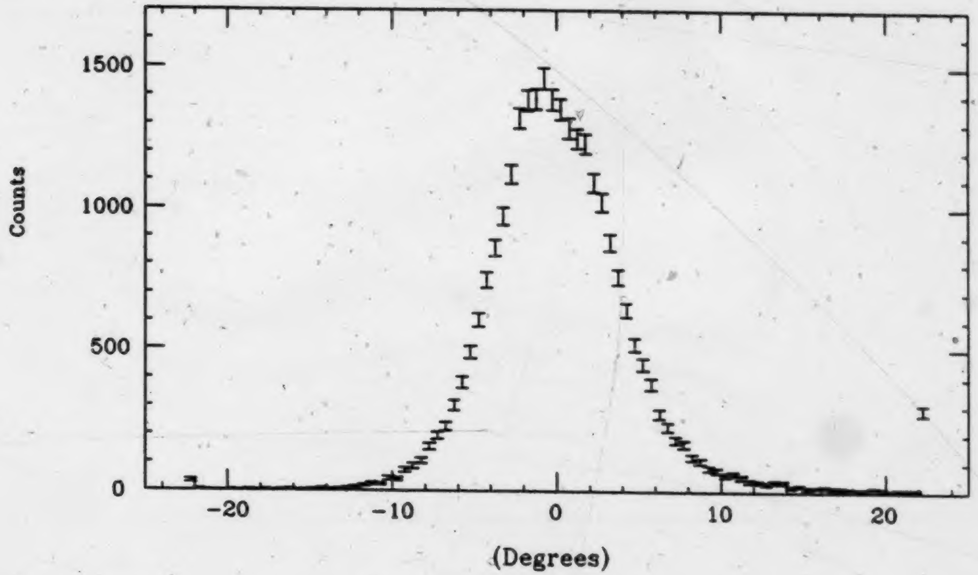

(b) Opening Angle Error (Monte Carlo)

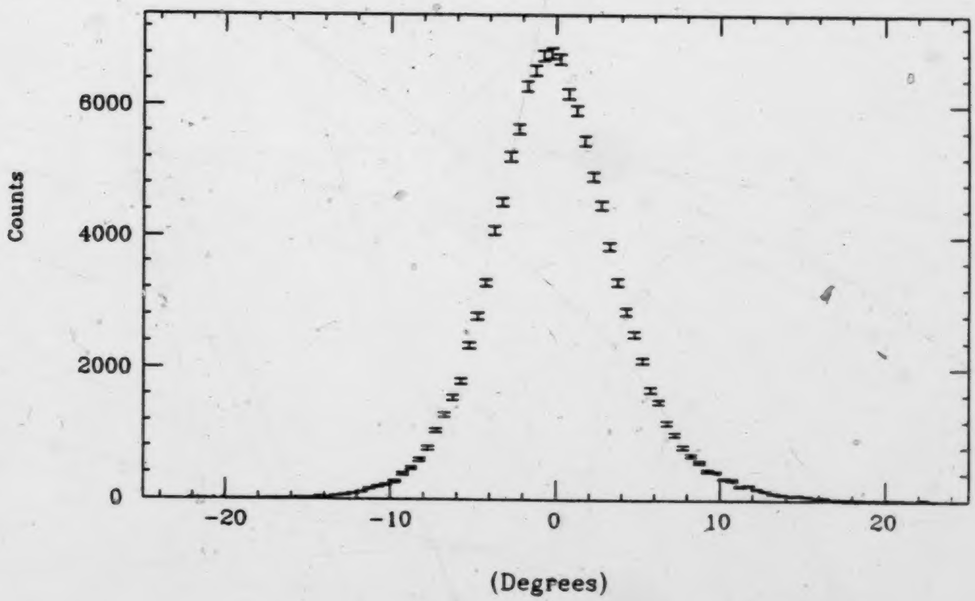

Figure C-6 $|\theta_1 + \theta_2| - 87^\circ$ for the (a) p-p and (b) Monte Carlo Data Sets.

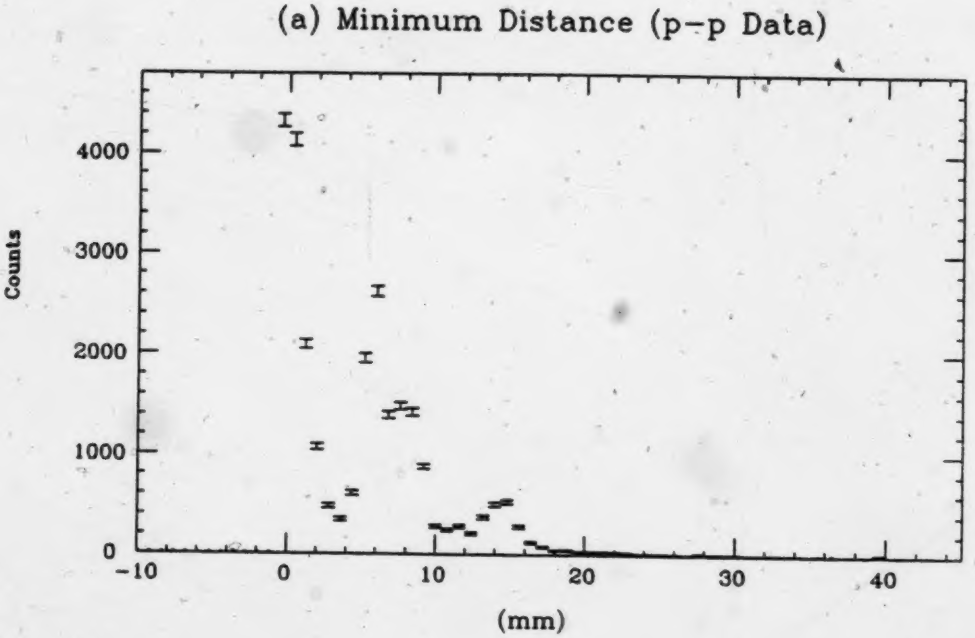
(a) Minimum Distance (p-p Data)

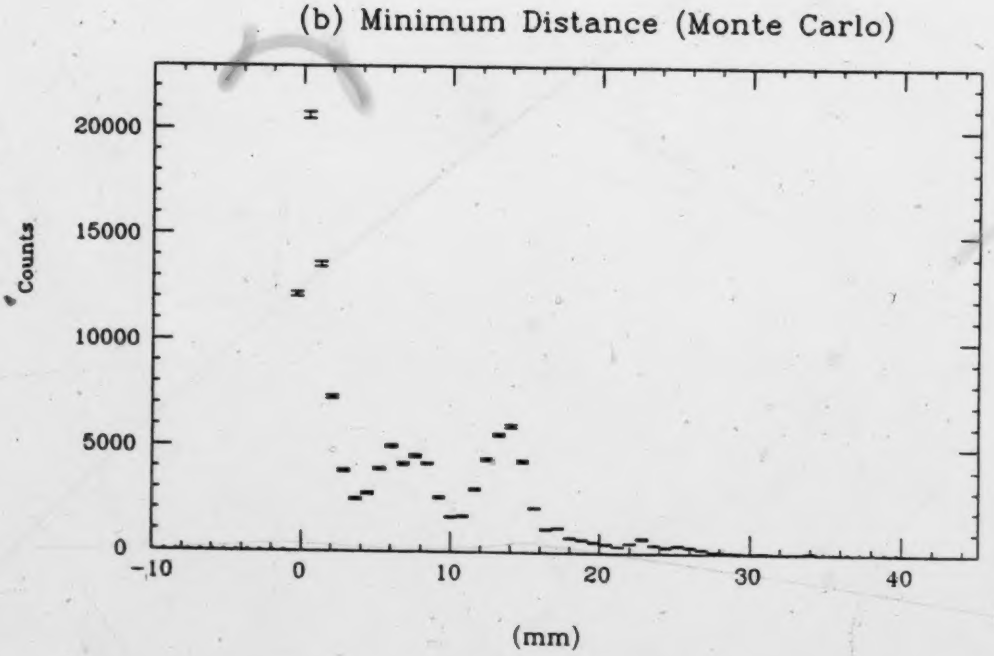
(b) Minimum Distance (Monte Carlo)

Figure C-7 Minimum Distance Between Outgoing Tracks for the (a) p-p and (b) Monte Carlo Data Sets.

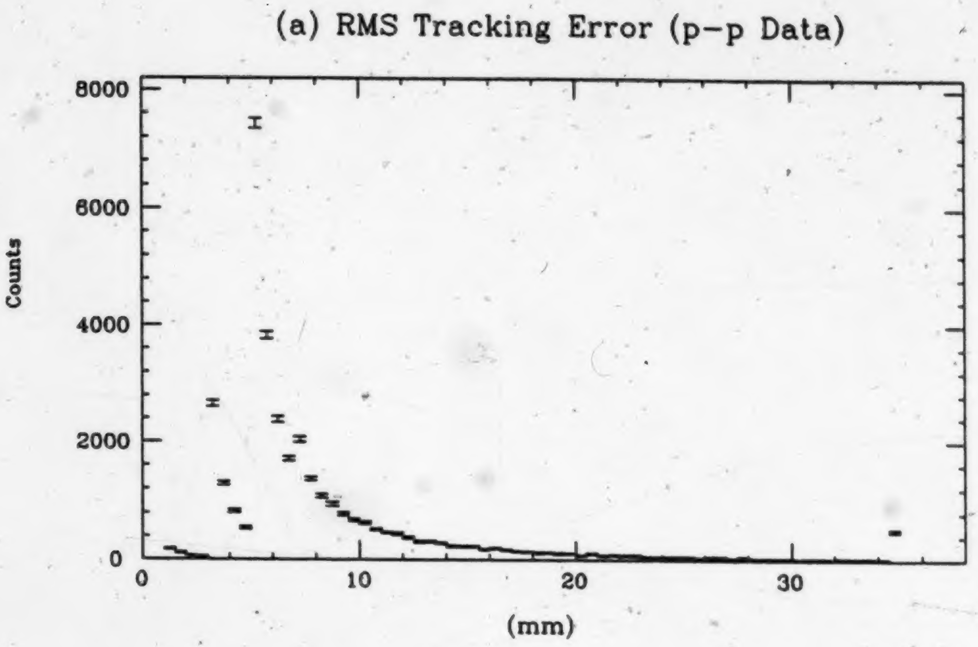

(a) RMS Tracking Error (p-p Data)

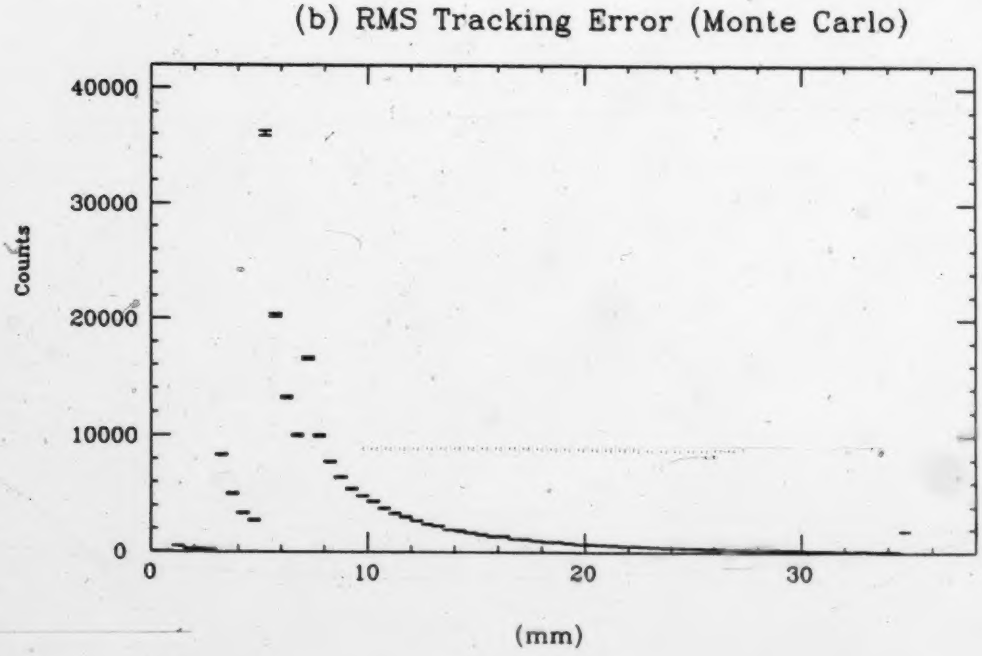

(b) RMS Tracking Error (Monte Carlo)

Figure C-8 RMS Tracking Error for the (a) p-p and (b) Monte Carlo Data Sets.

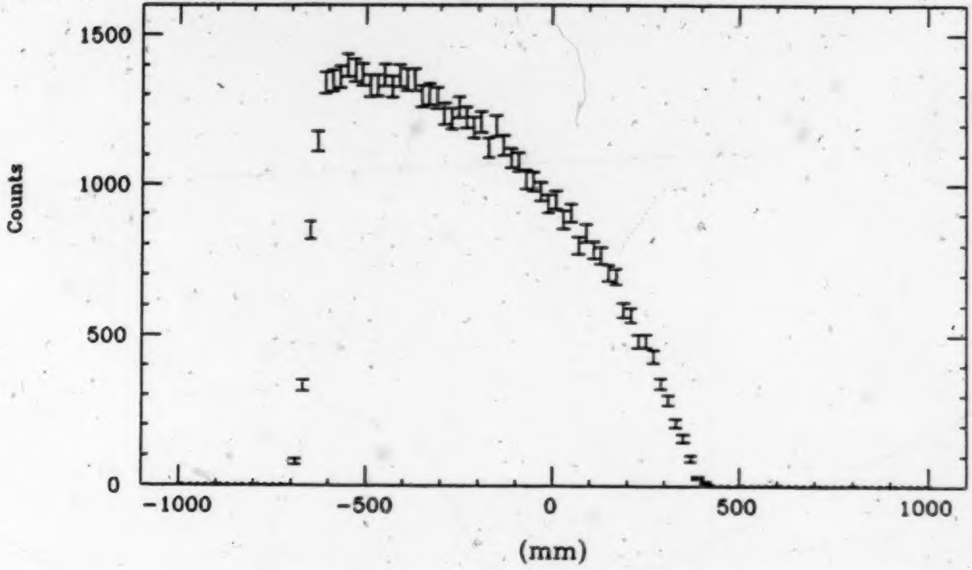

(a) Z-Vertex Position (p-p Data)

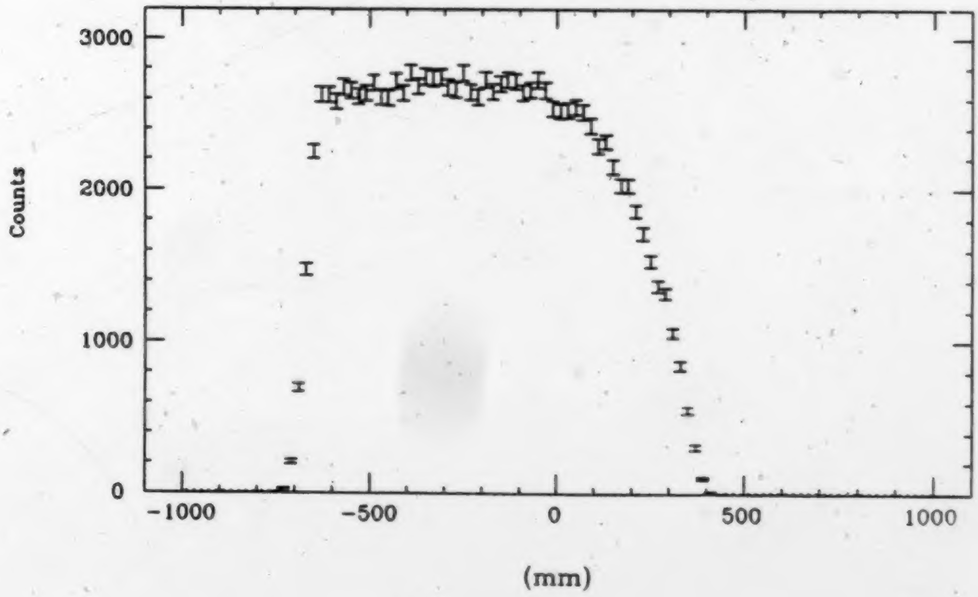

(b) Z-Vertex Position (Monte Carlo)

Figure C-9 Z - Position of the Interaction Vertex for the (a) p-p and (b) Monte Carlo Data Sets.

(a) QSUM - WC1 (p-p Data)

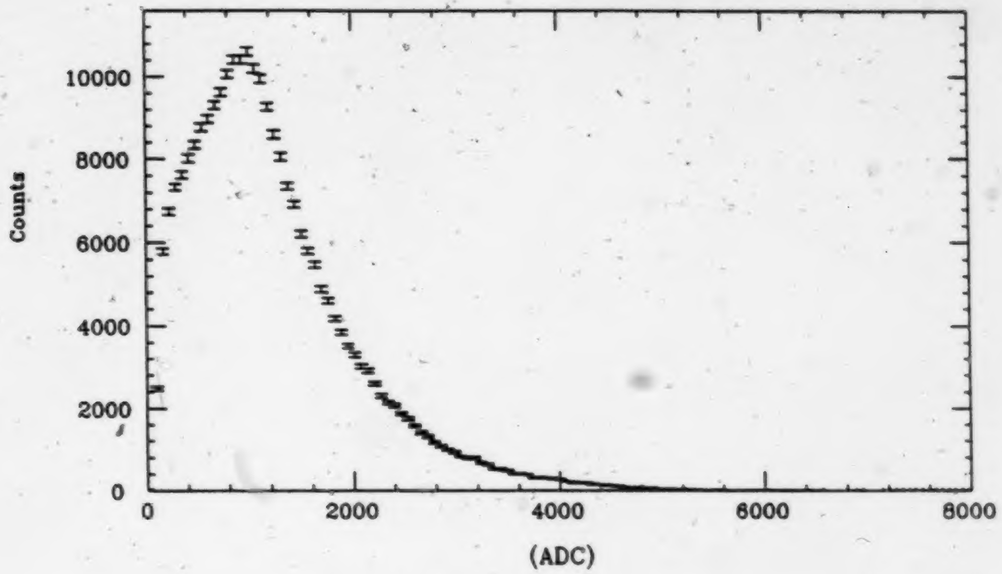

(b) QSUM - WC1 (Monte Carlo)

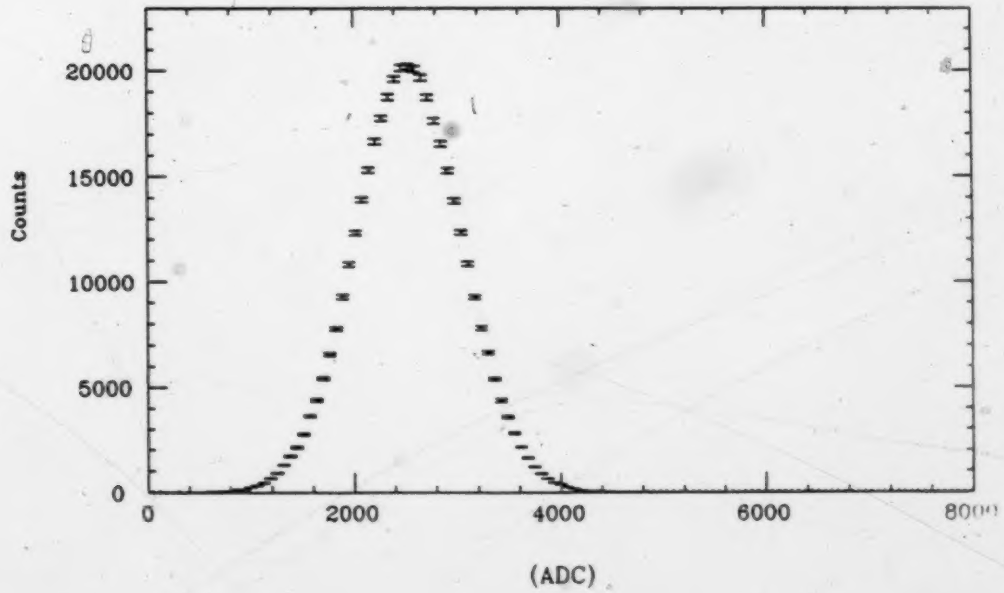

Figure C-10 Total Charge Collected by Wire Chamber 1 (Sum Over All Wires) for the (a) p-p and (b) Monte Carlo Data Sets.

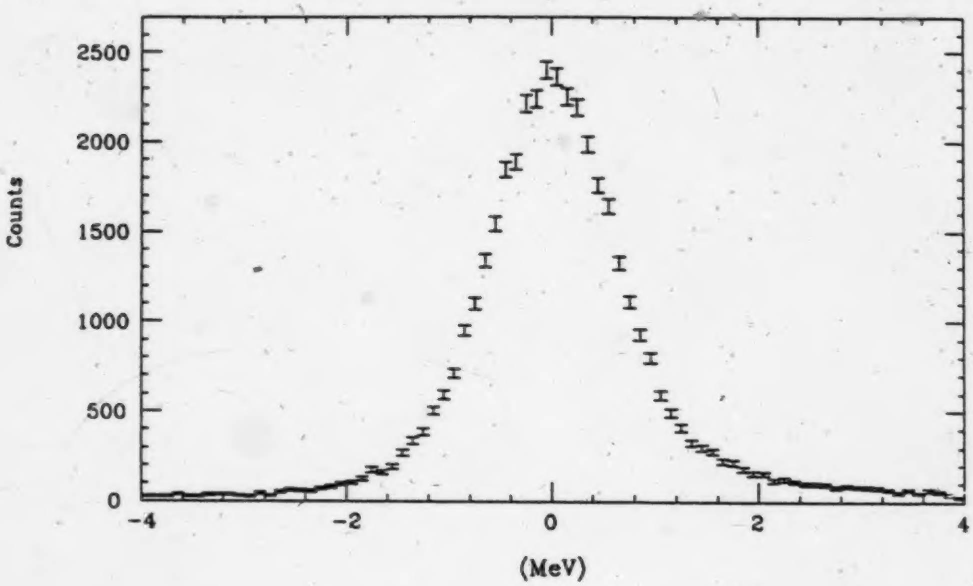

(a) Missing dE−Scintillator Energy (p−p Data)

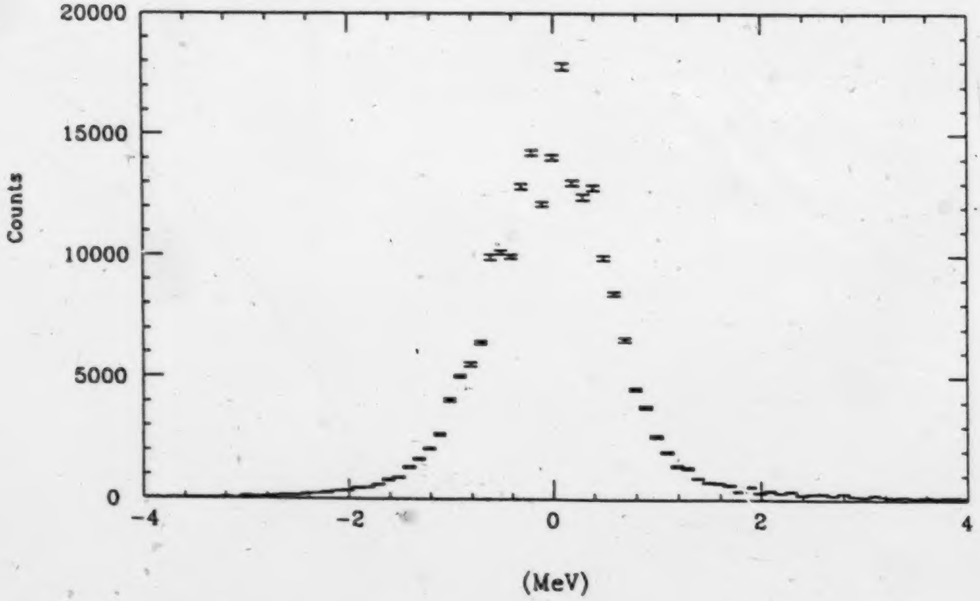

(b) Missing dE−Scintillator Energy (Monte Carlo)

Figure C-11 $E_{Calculated}$ - $E_{Measured}$ for the dE scintillators (Sum Over All dE Scintillators) for the (a) p-p and (b) Monte Carlo Data Sets.

(a) Missing E−Scintillator Energy (p−p Data)

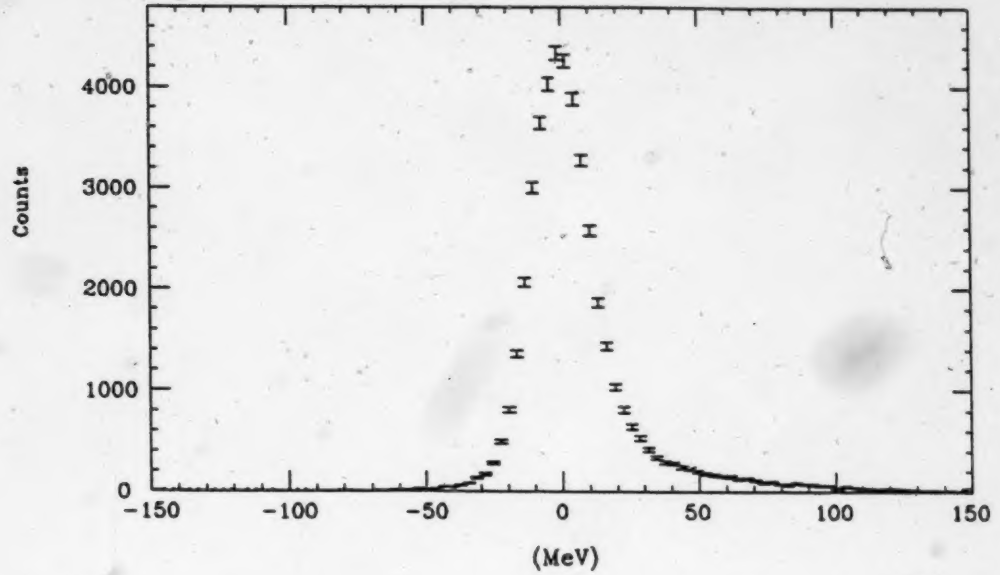

(b) Missing E−Scintillator Energy (Monte Carlo)

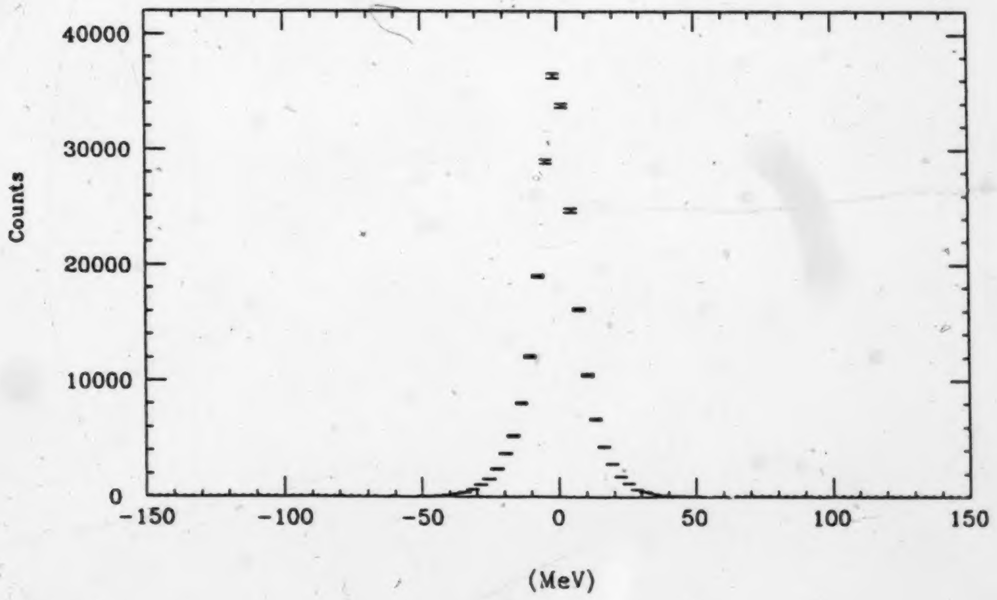

Figure C-12 $E_{Calculated} - E_{Measured}$ for the E scintillators (Sum Over All E Scintillators) for the (a) p-p and (b) Monte Carlo Data Sets.

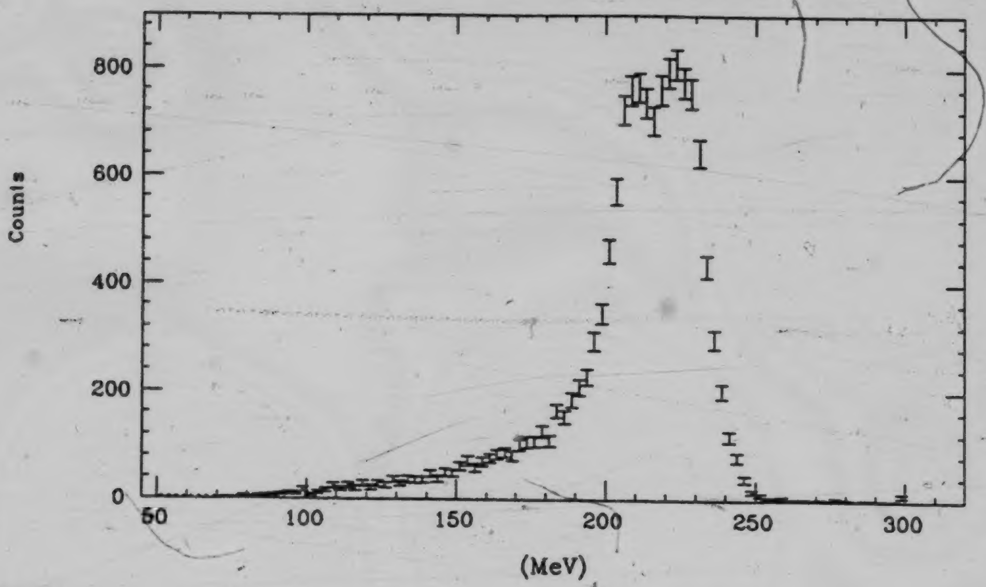
(a) Reconstructed Beam Energy (p−p Data)

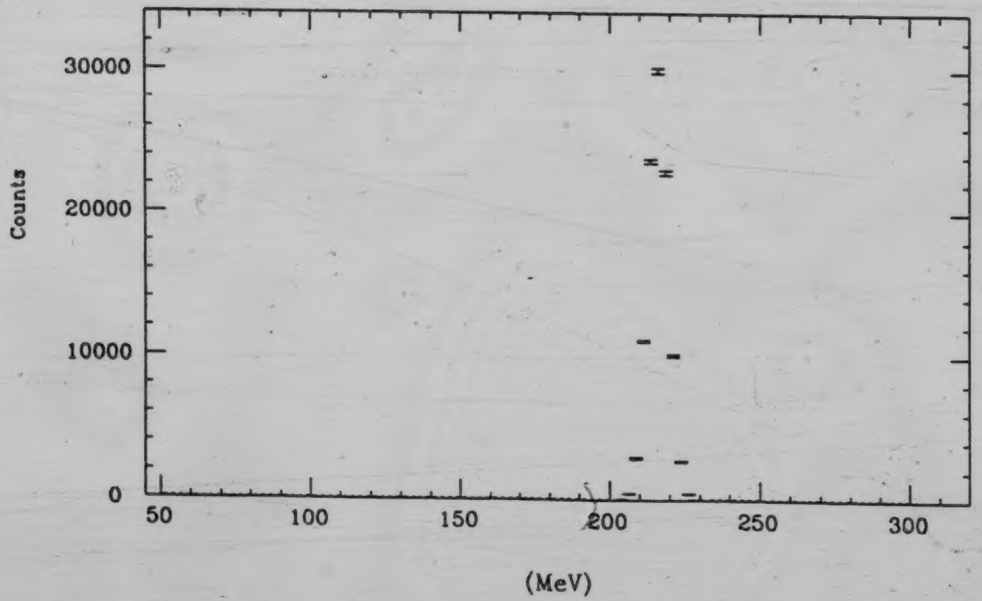
(b) Reconstructed Beam Energy (Monte Carlo)

Figure C-13 Beam Energy as Reconstructed from Energy Deposited in Scintillators for Two Track Events. (a) p-p and (b) Monte Carlo Data Sets